Universidade do Minho
Escola de Ciências

Rui Miguel Dinis Silva

Associated Production of Dark Matter with Heavy Fermions at the RUN3 of the LHC

Associated Production of Dark Matter with Heavy Fermions at the RUN3 of the LHC
Rui Miguel Silva
UMinho | 2023

november 2023

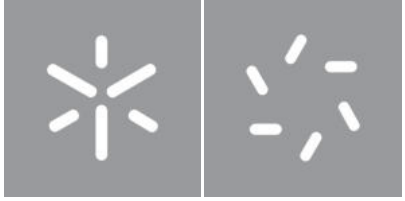

University of Minho
School of Sciences

Rui Miguel Dinis Silva

Associated Production of Dark Matter with Heavy Fermions at the RUN3 of the LHC

Master's Dissertation
Master in Physics

Dissertation supervised by
Prof. Dr. António J. Onofre A. R. Gonçalves

november 2023

Copyright and Terms of Use for Third Party Work

License granted to users of this work:

Acknowledgements

First, I would like to express my heartfelt gratitude to my supervisor Professor António Onofre. His constant dedication, enthusiasm and commitment throughout this work helped and motivated me even more to pursue my own path in this research and, overall, in Physics. The main tools to conduct this work were provided, and I was guided all along, but the freedom to pursuit my analysis and my intuitions in certain aspects of this dissertation helped me gain valuable skills that I truly cherish. Next, a big word of appreciation to my PhD Colleague, Esteban Chalbaud for his friendship and instrumental aid across all stages of this thesis. His constructive feedback helped me improve a lot as a physicist. I would also like to extend my thanks to Laboratório de Instrumentação e Física Experimental de Partículas (LIP) for all the support granted to me, without which this thesis would not have been made possible.

To my good friends and Minho physics family, Florival Cunha and Rui Dias, who have been with me since the beginning of this journey in my undergraduate years, I extend a massive word of gratitude. Also to Ricardo Barbosa, whom I met during this Master's degree.

To my very dear old friends Alberto Cunha and Carlos Santos, whom I have known forever a massive thank you as well, notably Alberto for those late-night coffee sessions where we talked about anything and everything. To Ana Sofia, my best and dearest friend, no words can describe or explain how much you have helped me all these countless years. And to Maria João as well, whose support was beyond fundamental.

To my Beatriz, forever this work will bear a mark of you. Your help and love were utterly fundamental on this journey. Thank you, thank you.

Lastly, to my loving family, specially my parents, Helena and Rui: I will be forever thankful for everything you have given me. The efforts you made, the love you gave me, the values you have raised me on. They made me the person I am today, and I will carry them throughout my life.

The cosmos is within us. We are made of star-stuff. We are a way for the universe to know itself.

Carl Sagan

Statement of Integrity

I hereby declare having conducted this academic work with integrity.

I confirm that I have not used plagiarism or any form of undue use of information or falsification of results along the process leading to its elaboration.

I further declare that I have fully acknowledged the Code of Ethical Conduct of the University of Minho.

University of Minho, Braga, november 2023

Rui Miguel Dinis Silva

Abstract

Dark matter (DM) stands as one of the most prominent mysteries that the Standard Model of Particle Physics (SM) has yet to unravel. Several compelling observations indicate the existence of non-baryonic matter in the Universe, which interacts solely through gravitational forces with ordinary matter. Assuming the presence of a new interaction mechanism, three distinct search approaches have arisen, with collider-based searches demonstrating notable potential for uncovering and characterizing the nature of DM.

In this thesis, a search is undertaken to explore possible DM particles concealed within the final states of the $t\bar{t}$ topology. Within the framework of the simplified DM models, this phenomenological analysis involves the reconstruction of a $t\bar{t}$ system considering the presence of a spin-0 mediator denoted as Y_0 that couples to both SM and DM particles. Signal samples of $pp \to t\bar{t}Y_0$ are generated at Next-to-Leading-Order (NLO), considering both Charge-Parity (CP)-even and CP-odd couplings of Y_0 to the top quarks. The `MadGraph5_aMC@NLO` framework is employed for this purpose. Various mass scales for the mediator Y_0 are explored, ranging from an ultra-low mass region (approximately 0 GeV) to the mass of the Higgs boson (125 GeV). The analysis concentrates on the dileptonic final states of the $t\bar{t}$ system, while accounting for all relevant SM background processes associated with the dileptonic $t\bar{t}$ search at the LHC. An event reconstruction algorithm is applied to both signal and background SM samples to reconstruct solely the $t\bar{t}$ system. Additionally, new CP angular observables are utilized to probe the CP-nature of the coupling between the mediator and top quarks. This leads to the establishment of confidence level (CL) limits for the Yukawa couplings as functions of the mediator mass.

Keywords CP Violation, Dark Matter, Top Quark, LHC, Phenomenology

Resumo

A Matéria Escura destaca-se como um dos mistérios mais proeminentes que o Modelo Padrão da Física de Partículas tem ainda por desvendar. Várias observações convincentes apontam para a existência de matéria não-bariónica no Universo, que interage com a demais matéria bariónica, apenas através de forças gravitacionais. Assumindo a existência de um novo mecanismo de interação, existem estratégias de pesquisas distintas, destacando-se as baseadas em colisionadores, que demonstram um potencial notável para desvendar e caracterizar a natureza da Matéria Escura.

Nesta dissertação, é realizada uma pesquisa por partículas passíveis de serem candidatas a Matéria Escura, em estados finais com a topologia $t\bar{t}$. Enquadrada em modelos simplificados de produção de Matéria Escura, a análise fenomenológica aqui apresentada envolve a reconstrução de um sistema $t\bar{t}$, considerando a presença de um mediador de spin-0, denominado por Y_0 que acopla tanto à Matéria Escura como às partículas do Modelo Padrão. Amostras de sinal de $pp \rightarrow t\bar{t}Y_0$ são geradas a Next-to-Leading-Order (NLO), considerando acoplamentos de Carga-Paridade (CP)-par e CP-ímpar do Y_0 aos quarks top. Para este propósito, é utilizado o gerador Monte-Carlo `MadGraph5_aMC@NLO`. São exploradas várias escalas de massa para o mediador Y_0, variando de uma região de massa ultra baixa (aproximadamente 0 GeV) até à região da massa do Bosão de Higgs (125 GeV). Esta análise é focada em estados finais dileptónicos do sistema $t\bar{t}$, e paralelamente considera todos os fundos de sinal do Modelo Padrão associados à pesquisa dileptónica de $t\bar{t}$ no LHC. É aplicado um algoritmo de reconstrução de eventos às amostras de sinal e de fundos para reconstruir somente o sistema $t\bar{t}$. Adicionalmente, novos observáveis angulares de CP, são utilizados para testar a natureza-CP do acoplamento entre o mediador e os quarks top, levando assim ao estabelecimento de limites nos acoplamentos entre o mediador e os quarks top em função da massa do mediador (Confidence Level limits).

Palavras-chave Violação de CP, Matéria Escura, Quark Top, LHC, Fenomenologia

Contents

Part I

Introduction

The Standard Model of Particle Physics (SM) [1, 2, 3] is a fundamental framework that describes nearly all the fundamental interactions. To explore the intricacies of these interactions, experiments are conducted at several different energy scales including those at the CERN Large Hadron Collider (LHC), which operates at the highest achievable energies in a laboratory.

One of the most significant milestones in recent particle physics history was the discovery of the Higgs boson in 2012 by the ATLAS and CMS experiments [4, 5]. This particle was predicted by the SM, and its discovery marked a crucial confirmation of the theory. However, despite this achievement, numerous unresolved questions linger in the field. One of these unresolved questions relates to the composition of the Universe itself. At cosmological scales, the evolution of the Universe, from the hot big bang to its present-day observed structure, can be described with a fairly good accuracy by the ΛCDM model. Nonetheless, astrophysical and cosmological observations reveal a universe in which over 80% of its matter content comprises non-baryonic particles, which are constituents not accounted for in the SM [6, 7]. This form of matter, which seems to interact solely through gravitational forces with ordinary matter, is termed Dark Matter (DM). Building upon these observations, it is hypothesized that DM is indeed composed of particles, which interact only very weakly with the SM. This line of reasoning suggests the possible existence of a *Dark Sector* comprised of particles beyond the SM (BSM). Among the prominent candidates proposed for describing the nature of DM is the Weakly Interacting Massive Particle (WIMP) framework, which will be explored in greater detail in this work.

This thesis examines the potential connection between the SM and Weakly Interacting Massive Particles (WIMPs) through simplified Dark Matter models. These models propose a new mediator particle that interacts with both DM and SM particles and can be generated in accelerator experiments, such as the LHC. The ATLAS collaboration has demonstrated that searches for such interactions with DM, with the $t\bar{t}$ topology emerging as both less explored and notably compelling [8], are possible. For this reason, this study assesses the impact of a spin-0 DM mediator $(J^{CP} = 0^{\pm})$ in the associated production process of $t\bar{t}Y_0$ through experimental analysis of $pp \to t\bar{t}$ in the dileptonic channel.

Three distinctive characteristics set this analysis apart from previous studies. Firstly, it introduces a novel approach by reconstructing the kinematics of the $t\bar{t}$ system without the need to reconstruct the DM particles produced in association with the $t\bar{t}$ system. Secondly, it explores scenarios involving DM particles with nearly zero mass, covering a broad spectrum of DM masses from ultra-light particles of a few GeV, extending up to the Higgs mass. Thirdly, it introduces two new angular observables based on the b_2 observable [9]. These observables are designed as discriminants for examining the CP-nature of these mediators, offering an alternative approach to ongoing searches that predominantly rely on missing

energy as a discriminator.

Significantly driven by these unique characteristics, this analysis aims to discern whether the presence of a DM particle alongside the $t\bar{t}$ pair results in observable differences in kinematic distributions. In the absence of such differences, the previously conducted analysis can be leveraged to constrain the couplings of DM particles. The following outlines the structure of the thesis.

In Chapter 1, the theoretical framework essential to this thesis is introduced. It includes a concise overview of the Standard Model of Particle Physics, an examination of the top quark, encompassing its properties and its relevance in High Energy Physics (HEP) experiments. Additionally, the chapter engages in a discussion of Dark Matter, shedding light on its context and the motivating factors behind its postulation, while also outlining the model employed in this thesis for elucidation.

In Chapter 2, the discussion centers on the current experimental setup enabling the observation of $t\bar{t}Y_0$ production at the LHC. This chapter provides an overview of the LHC and introduces the ATLAS detector [10]. The ATLAS experiment is presented with a focus on its fundamental characteristics as a modern, general-purpose particle physics experiment. As the present study was based on fast simulated events, the description of the tool used for detector simulation, `DELPHES` [11, 12], is also included in this chapter.

Chapter 3 provides an overview of the event analysis. It commences with the generation of simulated event samples and the specification of parameters employed for the fast simulation of a generic LHC detector. Subsequently, it delineates the anticipated final state of signal events and enumerates the primary background processes expected at the LHC. The chapter then delves into the description of the reconstruction of the $t\bar{t}$ events, with a primary focus on the kinematic fit conducted to reconstruct neutrinos and intermediate heavy particles of the $t\bar{t}$ decay chain. Additionally, it encompasses information on the selection criteria applied and the procedure employed for truth-match, i.e., the matching of the reconstructed objects to their corresponding leptons and quarks counterparts at parton-level. Moreover, a multivariate analysis is described as an alternative method for achieving this matching in the absence of parton-level information. The incorporation of two new observables related to the b_2 angular observable [9] is introduced towards the end of this chapter. These observables are subsequently compared to the original b_2 observable, serving the dual purpose of investigating the CP nature of the mediator and providing a comparative analysis. The motivation for including these observables and the specific methods used for their computation are outlined.

The analysis results previously described in the preceding chapter are displayed and discussed in Chapter 4. The distributions of the angular observables in the production of $t\bar{t}Y_0$ are shown and subse-

quently analyzed, with a comparison made between all of them. In the context of restricting the couplings of the DM mediator particle to the top quarks, the calculation of Confidence Levels for the rejection of various signal hypotheses is also presented and discussed upon.

The conclusions of this study are presented in the final chapter, Chapter 5. A case is made for the potential advantages of reconstructing the $t\bar{t}$ system in the quest for $t\bar{t}Y_0$ production, introducing an entirely novel approach to DM studies. Furthermore, the introduced angular observables exhibit a respectable discriminant power across the range of tested mediator masses. They are also instrumental in establishing exclusion limits to the couplings of the DM mediator to the top quarks for the distinct signal hypothesis. The use of these angular observables necessitates the reconstruction of the $t\bar{t}$ system. The chapter concludes with suggestions for enhancing the current work and considerations for its future progress.

Part II

Phenomenology and Experimental Setup

Chapter 1

Theory Framework

Chapter 1 introduces the foundational theory framework that underlies the key physics concepts explored in this thesis. Encompassing a comprehensive spectrum, spanning from the well-established Standard Model of Particle Physics to the intricate notion of Dark Matter. In Section 1.1, the Standard Model of Particle Physics is discussed, including its particle content, underlying group structure, and the Lagrangian density governing particle interactions and kinematics. The theoretical foundation for this Quantum Field Theory was laid in the 1960s through the works of Glashow [1], Weinberg [2], and Salam [3], and it has since been successful in describing the available particle physics experimental data, albeit with some limitations. In the subsequent section, Section 1.2, the top quark is explored, emphasizing its properties, decay modes, and the mechanisms of production at the LHC. In the concluding section 1.3, the focus is on addressing the issue of Dark Matter, including its origin and its connection with the current cosmological model (i.e. ΛCDM) in terms of its nature. The methods employed to detect Dark Matter are also discussed. Moreover, the search addressed in this thesis is explored using a Dark Matter Simplified Model [13], which is subsequently elucidated.

1.1 Standard Model of Particle Physics

Within the realm of particle physics, the Standard Model (SM) serves as the prevailing framework that describes three of the four fundamental forces in nature: the strong, electromagnetic, and weak forces. Notwithstanding, the gravitational force manifests at a considerably different energy scale and remains unaccounted for within the current scope of the Standard Model.

The Standard Model describes a Universe comprised of elementary particles, which can be categorized into fermions and gauge bosons. Fermions form the fundamental constituents of the Universe, while the gauge bosons serve as mediators that account for the interactions between these fundamental constituents.

Fermions The visible matter in the Universe is composed of 12 spin-$1/2$ fundamental particles which obey Fermi-Dirac statistics. These fermions are divided into leptons and quarks, and they are arranged in three generations, with each generation consisting of a pair of particles.

Every lepton generation encompasses one electrically charged lepton (e^-, μ^-, τ^-) and one neutral lepton, commonly referred to as neutrino (ν_e, ν_μ, ν_τ). On a similar note, a quark generation consists of an up-type quark (u, c, t) with a fractional electric charge of $+2/3$, and a down-type quark (d, s, b), which has a fractional electric charge of $-1/3$. In addition, the quarks possess a color charge (red, blue, green) as dictated by the theory of strong interactions, known as quantum chromodynamics (QCD). This color charge is a fundamental property that governs the behavior of quarks under the strong nuclear force [14].

The masses of fermions, directly connected to their Yukawa couplings, are regarded as free parameters within the SM. These parameters are not predicted by the SM itself but are determined through experimental measurements. The fermion masses, with the sole exception of the neutrinos still to be confirmed, exhibit an increasing pattern across generations, ranging over several orders of magnitude from the electron mass of approximately 0.5 MeV to the top-quark mass of around 173 GeV [15, 14].

Neutrinos are assumed to be massless within the framework of the SM. Nonetheless, this supposition has been proven wrong. Experimental observations of neutrino oscillations [16], for which Takaaki Kajita and Arthur B. McDonald were awarded the 2015 Nobel Prize in Physics, have provided a strong evidence that neutrinos must have non-zero masses, albeit small. The discovery of neutrino oscillations was made in the Super-Kamiokande and SNO collaborations, led by Kajita and McDonald, respectively [17].

An inclusive overview of the fermions within the SM, categorized into three generations, is shown in Table 1.

Each fermion type in the SM is associated with an antiparticle counterpart, with the same mass but with opposite quantum numbers.

Gauge Bosons The gauge bosons complement the matter particles within the framework of the SM. These gauge bosons, all characterized by their spin-1 nature, fulfill the role of mediators for the fundamental interactions between the matter particles. Table 2 displays the four gauge bosons associated with the fundamental forces of nature described by the SM.

The mediator responsible for the electromagnetic force is the photon (γ), which is massless and electrically neutral. The electromagnetic force affects all fermions, except for neutrinos, as photons couple to charged particles only.

On the other hand, the strong interaction is mediated by the massless gluon (g). This particle carries color charge and couples with quarks according to QCD. Consequently, the strong interaction has no effect

Quarks

Generation	Flavor	Charge	Mass
I	up (u)	$+2/3$	2.16 MeV
	down (d)	$-1/3$	4.67 MeV
II	charm (c)	$+2/3$	1.27 GeV
	strange (s)	$-1/3$	93.4 MeV
III	top (t)	$+2/3$	172.69 GeV
	bottom (b)	$-1/3$	4.18 GeV

Leptons

Generation	Name	Charge	Mass
I	electron (e^-)	-1	0.511 MeV
	electron neutrino (ν_e)	0	0
II	muon (μ^-)	-1	105.66 MeV
	muon neutrino (ν_μ)	0	0
III	tau (τ^-)	-1	1.78 GeV
	tau neutrino (ν_τ)	0	0

Table 1: Properties of Quarks and Leptons. Each fermion is accompanied by its corresponding mass and electric charge, [15].

on all leptons.

The weak interaction involves the neutral Z boson and the charged $W^\pm$ bosons, which interact with the weak isospin quantum property. Charged leptons and down-type quarks possess a weak isospin with a third component, T_3, of $-1/2$, while neutrinos and up-type quarks have a weak isospin with a third component of $1/2$. Therefore, the weak interaction is the only fundamental force that affects all fermions, including neutrinos. This force has a short range due to the massive nature of the weak bosons, which decay rapidly.

The $W^\pm$ boson can decay into either two quarks or a charged lepton and a neutrino, whereas the Z boson can decay into two quarks, two oppositely charged leptons, or two neutrinos.

Completing the particle content of the Standard Model is the Higgs boson (H), a spin-0 elementary particle. The Higgs boson, which possesses no electric charge, imparts mass to all fundamental particles, and itself has a mass of 125.25 ± 0.17 GeV [15, 14].

Gauge Bosons

Name	Charge	Mass	Interaction
Photon (γ)	0	0	Electromagnetic
Gluon (g)	0	0	Strong
Z^0	0	91.19 GeV	Weak
$W^{\pm}$	± 1	80.38 GeV	

Table 2: Properties of the Gauge Bosons. Each boson is accompanied by its corresponding mass and electric charge, [15].

1.1.1 A Simplified Quantum Field Theory Approach

Mathematically, the SM is formulated as a quantum field theory (QFT) that relies on the concept of local gauge symmetry within a set of gauge groups,

$$SU(3)_C \otimes SU(2)_L \otimes U(1)_Y, \tag{1.1}$$

where, $SU(2) \otimes U(1)$ is the gauge group associated with the electroweak interaction, which combines the electromagnetic and weak forces, and $SU(3)$ is the gauge group of the strong interaction.

The SM is able to combine quantum mechanics with special relativity, treating particles as excitations of their respective fields. The dynamics and interactions of particles within the model are mathematically described by a density term called the SM Lagrangian density, denoted as $\mathcal{L}_{SM}$.

The complete SM Lagrangian density, more commonly denoted as simply the SM Lagrangian, is written as:

$$\mathcal{L}_{SM} = \mathcal{L}_{EW} + \mathcal{L}_{QCD} + \mathcal{L}_{Higgs} + \mathcal{L}_{Yukawa}. \tag{1.2}$$

In the following subsections, each term of the Lagrangian is explained in more detail.

Dynamics of Free Fermions

Firstly, it is important to highlight several aspects of the underlying QFT that constitutes the Standard Model before delving into each term of the $\mathcal{L}_{SM}$.

The Lagrangian that describes the motion of free fermions is the Dirac Lagrangian,

$$\mathcal{L} = \bar{\psi}(i\gamma^{\mu}\partial_{\mu} - m)\psi. \tag{1.3}$$

Here, ψ represents the fermionic field, γ^μ denotes the Dirac matrices, and m represents the fermion mass. This Lagrangian exhibits invariance under global gauge transformations. However, to satisfy local gauge invariance, the ordinary partial derivative in the Lagrangian must be replaced by the covariant derivative,

$$D_\mu = \partial_\mu - igA^a_\mu T^a. \tag{1.4}$$

The A^a_μ vector field, also known as the gauge field, is introduced into the covariant derivative to ensure a local gauge invariance. It interacts with the scalar field through a coupling strength parameter denoted as g.

The number of vector fields required for maintaining local gauge invariance is determined by the number of generators T^a associated with the underlying symmetry group. These generators satisfy the commutation relation:

$$[T^a, T^b] = if^{abc}T^c. \tag{1.5}$$

f^{abc} represents the structure constants of the symmetry group, which describe the algebraic relationship between the generators. The non-zero structure constants indicate the non-Abelian nature of the gauge theory, where the generators do not commute with each other. The Lagrangian of free vector fields is written as:

$$\mathcal{L} = -\frac{1}{4}F^a_{\mu\nu}F^{\mu\nu}_a, \tag{1.6}$$

where, $F_{\mu\nu}$ represents the electromagnetic tensor

$$F^a_{\mu\nu} = \partial_\mu A^a_\nu - \partial_\nu A^a_\mu + gf^{abc}A^b_\mu A^c_\nu. \tag{1.7}$$

The omission of mass terms in this Lagrangian is motivated by the need to maintain gauge invariance in the electroweak theory. The inclusion of mass terms would violate gauge symmetry, and hence they will be introduced via the the Brout-Englert-Higgs mechanism.

Electroweak Interaction

The electroweak theory unifies the electromagnetic interaction and the weak interaction. It encompasses flavor-conserving neutral currents mediated by the photon and the Z boson, as well as flavor-changing charged currents mediated by the $W^\pm$ bosons [14]. While the electromagnetic and neutral weak interactions do not exhibit a preference for either left-handed or right-handed fermions and couple to both chiralities equally, the charged weak interaction, characterized by the $SU(2)$ symmetry group, manifests

complete parity violation by exclusively coupling with left-handed fermions. As a result, a clear distinction arises between the left-handed components (ψ_L) and the right-handed components (ψ_R) of the fermionic field [1]:

$$\psi_{L/R} = \frac{1}{2}(1 \mp \gamma^5)\psi, \tag{1.8}$$

where, γ^5 is defined as the product of the Dirac matrices $\gamma^0\gamma^1\gamma^2\gamma^3$, transforming a vector into an axial vector, giving rise to the $V - A$ coupling structure in weak interactions.

Under $SU(2)$ transformations, the left-handed and right-handed components of the fermionic field undergo distinct transformations. Left-handed fermions are arranged in $SU(2)$ doublets as:

$$L_L^i = \begin{pmatrix} \nu_L^i \\ l_L^i \end{pmatrix} \quad Q_L^i = \begin{pmatrix} u_L^i \\ d_L^i \end{pmatrix}. \tag{1.9}$$

L_L^i and Q_L^i correspond to the left-handed leptons and quarks doublets of generation i, respectively. The right-handed fermions are instead $U(1)$ singlets,

$$(l_R^i) \quad (u_R^i) \quad (d_R^i) \ , \tag{1.10}$$

with l_R^i, u_R^i and d_R^i being the lepton, up-type and down-type singlets, respectively. The lack of right-handed neutrinos in the SM results in the nonexistence of neutrino singlets.

The generator of $SU(2)$ is the weak isospin operator,

$$T_i = \frac{\sigma_i}{2}, \tag{1.11}$$

where, σ_i corresponds to the Pauli matrices. There are a total of three $SU(2)$ generators. Regarding the $U(1)$ symmetry group, its generator is the hypercharge operator Y, and is related to the electric charge Q and the third component of the weak isospin, T_3, via the Gell-Mann–Nishijima relation:

$$Q = \frac{Y}{2} + T_3. \tag{1.12}$$

Then, building upon the previous definition in 1.4 , the covariant derivative D_μ, which satisfies local gauge invariance, is expressed as:

$$D_\mu = \partial_\mu - igW_\mu^i \frac{\sigma^i}{2} - ig'B_\mu \frac{Y}{2}, \tag{1.13}$$

where, W_μ^i represents the three gauge fields associated with $SU(2)$ symmetry, and B_μ represents the gauge field associated with $U(1)$. The g and g' parameters denote the coupling constants of the $SU(2)$ and $U(1)$ symmetry groups, respectively.

[1] The fermionic field ψ is partitioned into its chiral projection operators

From these definitions, it is possible to write the electroweak Lagrangian as:

$$\mathcal{L}_{EW} = -\frac{1}{4}W^i_{\mu\nu}W^{i\mu\nu} - \frac{1}{4}B_{\mu\nu}B^{\mu\nu} + \bar{\psi}_L i\gamma^\mu D_\mu \psi_L + \bar{\psi}_R i\gamma^\mu D_\mu \psi_R, \tag{1.14}$$

$$\mathcal{L}_{EW} = -\frac{1}{4}W^i_{\mu\nu}W^{i\mu\nu} - \frac{1}{4}B_{\mu\nu}B^{\mu\nu} + \bar{\psi}_L i\gamma^\mu \left(\partial_\mu - igW^i_\mu \frac{\sigma^i}{2} - ig'B_\mu \frac{Y}{2}\right)\psi_L$$

$$+\bar{\psi}_R i\gamma^\mu \left(\partial_\mu - ig'B_\mu \frac{Y}{2}\right)\psi_R, \tag{1.15}$$

in which, $B_{\mu\nu} = \partial_\mu B_\nu - \partial_\nu B_\mu$ and $W^i_{\mu\nu} = \partial_\mu W^i_\nu - \partial_\nu W^i_\mu + g\epsilon^{ijk}W^j_\mu W^k_\nu$ correspond to the kinematic terms of the EW gauge bosons, with the antisymmetric Levi-Civita tensor ϵ^{ijk} .

Strong Interaction

The strong interaction, which describes the interactions between quarks and gluons, is best analyzed within the theory of Quantum Chromodynamics (QCD). This theory is characterized by a gauge symmetry group $SU(3)$, consisting of eight generators representing the eight mediating gluon fields [18]. In QCD, gluon-gluon interactions induce an anti-screening effect on the quark charge, causing it to become stronger at shorter distances. The QCD Lagrangian is expressed as:

$$\mathcal{L}_{QCD} = \bar{q}(i\gamma_\mu D_\mu - m)q - \frac{1}{4}G^a_{\mu\nu}G^{\mu\nu}_a, \tag{1.16}$$

after imposing local gauge invariance. Here, the covariant derivative D_μ is defined as:

$$D_\mu = \partial_\mu + ig_s G^a_\mu T_a, \tag{1.17}$$

where, g_s is the coupling constant for the strong interactions, and T_a are the $SU(3)$ generators. G^a_μ represents the spin-1 chargeless gluons, from where the gluon field tensor $G^a_{\mu\nu}$ is provided by:

$$G^a_{\mu\nu} = \partial_\mu A^a_\nu - \partial_\nu A_\mu g_s f^{abc} A^b_\mu A^c_\nu \tag{1.18}$$

For low momentum transfer Q interactions, QCD exhibits a strong coupling regime ($\alpha_s \approx 1$[2]). This strong coupling prevents the applicability of perturbative methods and results in confinement [3]. Quarks are either confined as mesons (one quark with a certain colour and one antiquark with its anticolour) or baryons, three (anti-)quarks with the three different colour charges, color neutral bound states.

[2] α_s is commonly denoted as the coupling strength, and it represents the strength of the strong nuclear force

[3] Momentum transfer Q is defined as the difference in the four-momentum vectors of the incoming and outgoing particles.

The Brout-Englert-Higgs Mechanism

At this stage, the SM faces certain limitations that require the introduction of an additional mechanism. One such limitation arises from the fact that the theory does not account for the masses of gauge bosons or fermions, as they would explicity break the local gauge invariance. To address this issue, the Brout-Englert-Higgs mechanism emerges as a necessary component within the SM framework [14].

Incorporating the Brout-Englert-Higgs mechanism into the SM involves the addition of an isospin doublet of complex scalar fields, denoted as ϕ, along with a specific potential.

The Higgs potential $V(\phi)$ is gauge-invariant under the $SU(2)$ symmetry group and is expressed as:

$$V(\phi) = \frac{1}{2}\mu^2\phi^\dagger\phi - \frac{1}{4}\lambda(\phi^\dagger\phi)^2. \tag{1.19}$$

This establishes the Higgs sector,

$$\mathcal{L}_{Higgs} = (D_\mu\phi)^\dagger(D^\mu\phi) - \underbrace{\frac{1}{2}\mu^2\phi^\dagger\phi + \frac{1}{4}\lambda(\phi^\dagger\phi)^2}_{V(\phi)}. \tag{1.20}$$

The Higgs potencial depends on two parameters, namely λ and μ^2. In the case where $\lambda < 0$, it is considered to be unphysical because it leads to a potential without any stable minima. However, when both λ and μ^2 are positive, there exists a unique stable global minimum at $\phi = 0$. On the other hand, if $\lambda > 0$ but $\mu^2 < 0$, the minimum becomes degenerate and continuous in three dimensions, satisfying:

$$|\phi|^2 = \phi^\dagger\phi = \frac{\mu^2}{2\lambda} = \frac{v^2}{2}, \tag{1.21}$$

where v is referred to as the vacuum expectation value (VEV). The behaviour of $V(\phi)$ is depicted in Figure 1.

Choosing a minimum yields $\phi_0 = {}^1/\sqrt{2}\binom{0}{v}$, consequently the Higgs field can be expressed as an excitation around its minimum:

$$\phi = \frac{1}{\sqrt{2}}\begin{pmatrix} 0 \\ v + h(x) \end{pmatrix}. \tag{1.22}$$

Chiral fermions do not possess mass terms of the form $m\bar{\psi}\psi$ due to the chiral symmetry[4]. Instead, they acquire mass through their interactions with the Higgs field, facilitated by the Yukawa coupling.

The Yukawa Lagrangian $\mathcal{L}_{Yukawa}$ is expressed as follows:

$$\mathcal{L}_{Yukawa} = g_f\bar{\psi}_L\psi_R\phi. \tag{1.23}$$

[4] $m\psi\bar{\psi}$ describes the interaction of a fermionic field with a mass parameter

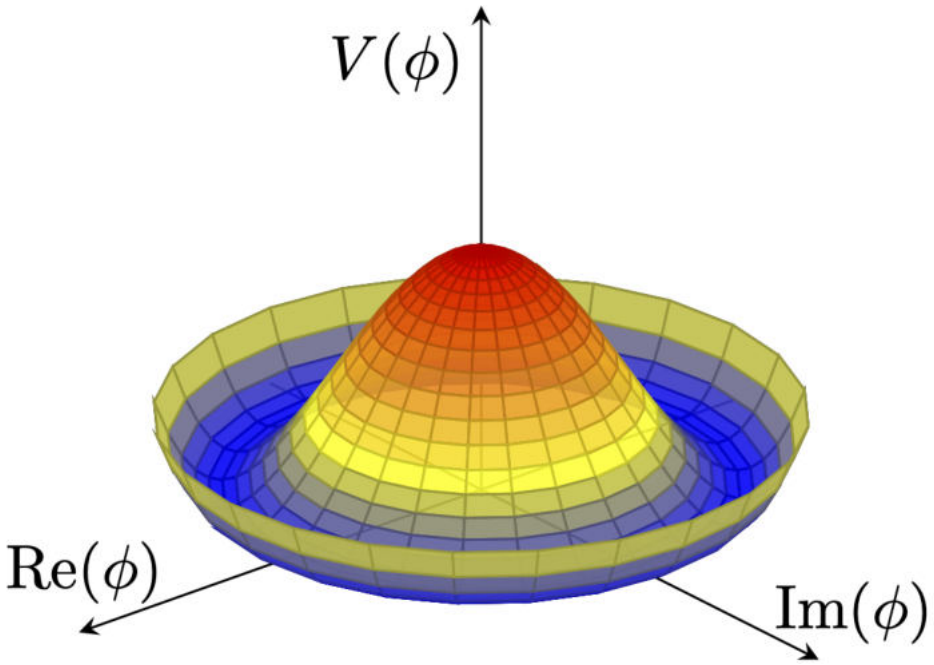

Figure 1: Schematic of the Higgs potential $V(\phi)$ in three dimensions, with $\lambda > 0$ and $\mu^2 < 0$. [19]

It encompasses a contribution for each fermion term, which, after spontaneous symmetry breaking, results in a chiral mass term m_f and a coupling to the Higgs field:

$$m_f = g_f \frac{v}{\sqrt{2}}. \tag{1.24}$$

The process of spontaneous symmetry breaking (SSB) in the Higgs doublet also results in the generation of mass terms for the electroweak gauge bosons. The requirement of $SU(2) \otimes U(1)$ invariance in the Higgs sector leads to the following conditions:

$$\mathcal{L}_{Higgs} = |(\partial_\mu + igW_\mu^a + ig'YB_\mu)\phi|^2 - V(\phi), \tag{1.25}$$

After undergoing spontaneous symmetry breaking, the electroweak W^a and B fields combine and interact to give rise to the physical states: $W^\pm$, Z^0 and γ. These bosons acquire their masses through their coupling to the vacuum expectation value v:

$$m_Z = \frac{v}{2}\sqrt{g^2 + g'^2}, \qquad m_W = \frac{g}{2}v, \qquad m_\gamma = 0. \tag{1.26}$$

The CKM Matrix

As a final note, it is worth noting that the mass eigenstates obtained through the Yukawa couplings may not align precisely with the electroweak eigenstates. This discrepancy introduces a mixing phenomenon between generations, where left-handed up-type and down-type quarks are transformed between the eigenstates using different matrices. This mixing is quantified by the unitary Cabibbo-Kobayashi-Maskawa (CKM)

matrix, which is commonly represented as:

$$V_{CKM} = \begin{pmatrix} V_{ud} & V_{us} & V_{ub} \\ V_{cd} & V_{cs} & V_{cb} \\ V_{td} & V_{ts} & V_{tb} \end{pmatrix}$$

$$= \begin{pmatrix} c_{12}c_{13} & s_{12}c_{13} & s_{13}e^{-i\delta} \\ -s_{12}c_{23} - c_{12}s_{23}s_{13}e^{i\delta} & c_{12}c_{23} - s_{12}s_{23}s_{13}e^{i\delta} & s_{23}c_{13} \\ s_{12}s_{23} - c_{12}c_{23}s_{13}e^{i\delta} & -c_{12}s_{23} - s_{12}c_{23}s_{13}e^{i\delta} & c_{23}c_{13} \end{pmatrix}. \quad (1.27)$$

Here, $c_{ij} = \cos\theta_{ij}$, and $s_{ij} = \sin\theta_{ij}$. It uses three mixing angles (θ_{12},θ_{13},θ_{23}) and a phase δ, responsible for all CP-violating phenomena in flavour changing processes in the SM [20].

Assuming the three generations of quarks and the unitarity of the CKM matrix, the magnitudes of all nine CKM elements are constrained to specific allowed ranges [16].

$$V_{CKM} = \begin{pmatrix} 0.97373 \pm 0.00031 & 0.2243 \pm 0.0008 & (3.82 \pm 0.20) \times 10^{-3} \\ 0.221 \pm 0.004 & 0.975 \pm 0.006 & (40.8 \pm 1.4) \times 10^{-3} \\ (8.6 \pm 0.2) \times 10^{-3} & (41.5 \pm 0.9) \times 10^{-3} & 1.014 \pm 0.029 \end{pmatrix}. \quad (1.28)$$

The CKM matrix elements represent the probabilities of quark transitions in the process of $q \to q'W^{\pm}$. For the top quark, the probability of the $t \to bW^{\pm}$ vertex transition is proportional, in first approximation, to $|V_{tb}|^2$. Comparatively, the values of V_{td} and V_{ts} are much smaller than V_{tb}. As a result, the primary decay mode of the top quark involves the emission of a W boson and a bottom quark (for the CKM matrix, refer to [20, 16]).

1.2 Top Quark

The top quark (t) is an elementary fermion and belongs to the third family of quarks. It has an electric charge of $Q = +2/3$ and a weak isospin of $T_3 = +1/2$. The top quark is the heaviest elementary particle in the SM, with a reported mass of 173.4 ± 0.36 (stat) ± 0.67 (syst) GeV/c^2 [21], obtained from the first combination of Tevatron and LHC measurements. This mass value is approximately 35 times larger than that of the b quark, its weak isospin partner. The large mass of the top quark implies a Yukawa coupling to the Higgs boson with a value near unity, making it distinct from all other known particles.

The primary decay channel for a top quark is through the charged current interaction, specifically $t \to W^+b$ ($\bar{t} \to W^-\bar{b}$), as governed by the CKM mixing matrix. Categorization of the top quark decay

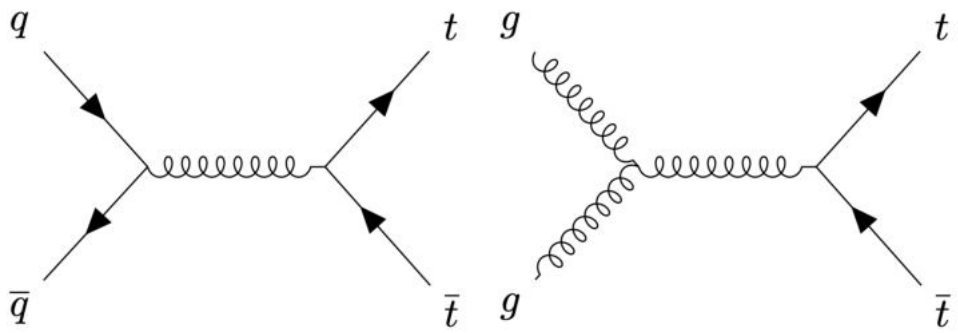

Figure 2: Feynman diagrams representing the Leading-Order $t\bar{t}$ production at the LHC: *quark-antiquark annihilation* on the right and *gluon-gluon fusion* on the left.

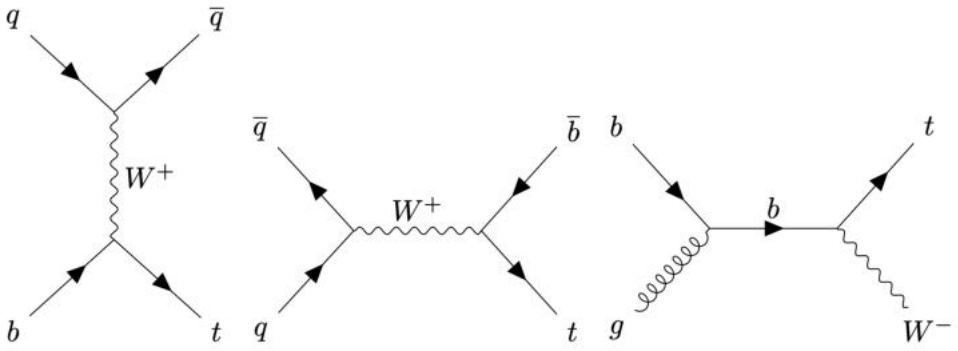

Figure 3: Feynman diagrams corresponding to the single top production at the LHC: on the right, the t-*channel*; in the center, s-*channel*; and on the left, the Wt *associated production*.

relies on the subsequent decay of the produced W boson: It is referred to as *leptonic* if the W boson decays into a lepton and a neutrino, and *hadronic* if the W boson decays into a quark-antiquark pair.

The initial indirect evidence for the existence of the top quark, originated from the requirement of renormalization of the SM Lagrangian. This requirement only holds true if the total sum of weak hypercharge for all left-handed fermions equals zero. Lepton multiplets contribute with $Y = -2$, while quark multiplets contribute with $Y = -2/3$. Consequently, the sum can only cancel out if every quark exists in three color variations and the number of quark flavors matches the number of lepton species. Thus, the presence of a sixth quark seemed to be a mandatory conclusion.

In 1995, the CDF and DØ experiments reported the discovery of the top quark in proton-antiproton collisions ($q\bar{q} \to t\bar{t}$ and $gg \to t\bar{t}$) with a center of mass energy of $\sqrt{s} = 1.8$ TeV at the Fermilab Tevatron collider [22, 23], concluding the search for the three-generation structure of the SM.

At the LHC, the production of top quarks can occur via strong or weak processes. The primary modes of top quark production are pair production ($t\bar{t}$) and single production (single top) mediated by the strong and weak interactions, respectively (See Figures 2 and 3). The dominant mechanisms for $t\bar{t}$ production are

the QCD processes $q\bar{q} \rightarrow t\bar{t}$ and $gg \rightarrow t\bar{t}$. The cross section for $t\bar{t}$ production at a center-of-mass energy of 14 TeV, assuming the SM at Next-to-Next-to-Leading Order (NNLO), is calculated to be $985.7^{+24.1}_{-35.7}$ pb [24, 20].

It distinguishes itself from other quarks with its large mass and its relatively short mean lifetime of 10^{-25} s compared to the mean hadronization time of about 10^{-24} s, meaning it can decay before it can undergo hadronization. Consequently, it enables the investigation of the properties of a free quark, which is otherwise impossible due to the rapid hadronization of all the other quark flavors. By examining the decay products, the properties of the quark before decay can be measured with precision, providing an opportunity to probe the predictions of the SM. The measurement of the top quark polarization through the analysis of its decay products is a notable example. The polarization of a top quark pair at the production level is entirely transferred to the decay products of the system. While top quark pairs are unpolarized in production at hadron colliders, their spins exhibit strong correlations [25, 26].

1.3 Dark Matter

The nature of Dark Matter (DM) stands as one of the most significant unresolved questions in physics today [6]. There have been various astronomical observations that strongly suggest the presence of a significant non luminous matter density in the Universe. This matter behaves similarly to ordinary matter but does not interact with particles governed by the strong or electroweak forces of the Standard Model, at least with the same intensity. Currently, only gravitational effects resulting from its existence have been detected, and as a result, there have been no direct observations of DM, so far.

In the subsequent subsection, a succinct overview of the experimental evidence supporting the existence of DM is presented. Following that, a concise overview of the ΛCDM model and the Weakly Interacting Massive Particle (WIMP) framework is provided. Additionally, the methodology and model employed to address the dark matter phenomenon in this thesis are outlined.

1.3.1 Experimental Evidence

Galaxy Rotational Curves

The first clue to the existence of Dark Matter emerged in 1932 when J. H. Oort studied the rotational velocity of stars in the Milky Way. By measuring the Doppler shift of spectral lines, Oort revealed that the observed amount of luminous matter, which produces a gravitational field, was inadequate to explain the stars' orbital motion [27]. Further measurements conducted on the rotational velocity of galaxies and

clusters of galaxies yielded similar results [28].

According to classical mechanics, the rotational velocity of matter located at a distance r from the galactic center is represented by the equation

$$v(r) = \sqrt{G\frac{m(r)}{r}}, \tag{1.29}$$

where, G is the gravitational constant and $m(r)$ is the total mass contained within r, which is derived from simply setting the gravitational force equal to the centripetal force (as planetary orbits are roughly circular) [6].

Based on astronomical observations of luminous matter, when considering sufficiently large values of distance r, the mass value should approach a constant. Consequently, the asymptotic behavior of $v(r)$ is expected to decrease as $1/\sqrt{r}$ [5]. In contrast to the expected asymptotic behavior, the experimental observations (see Figure 4) reveal a roughly constant behavior for $v(r)$ in the asymptotic regime. This discrepancy can be explained by the presence of a *halo* of DM, in which galaxies are embedded, characterized by a constant mass density $\rho(r)$.

Gravitational Lensing

Further experimental evidence to probe existence of DM is obtained through the observation of strong gravitational lensing effects on highly resolved galaxies. Gravitational lensing arises from the Theory of Relativity of Albert Einstein, which postulates that the Universe exists within a flexible fabric of spacetime. Objects with colossal masses bend this fabric, affecting the paths of other bodies around them, including the paths of light rays. Cosmologists study this phenomenon by observing luminous arcs or closed rings, surrounding a foreground galaxy cluster, which were produced by the deviated light rays of a background galaxy [29, 6]. A detailed map showing the mass distribution of the CL0024+1654 cluster has been successfully generated using gravitational lensing techniques. This achievement involved correlating the map with an image from the Hubble Space Telescope. The analysis revealed that visible stars within the cluster are surrounded by a homogeneous matter distribution that does not emit electromagnetic radiation. This finding provides strong support for the hypothesis of a dark matter halo enveloping the galaxies within the cluster. In Figure 5, the Hubble Space Telescope image of CL0024+1654 shows multiple blue, loop-shaped objects, which are actually multiple images of the same galaxy. These duplicates result from the gravitational lensing effect caused by a cluster of yellow elliptical and spiral galaxies [30].

[5] This asymptotic behavior is generally referred to as "Keplerian" behavior.

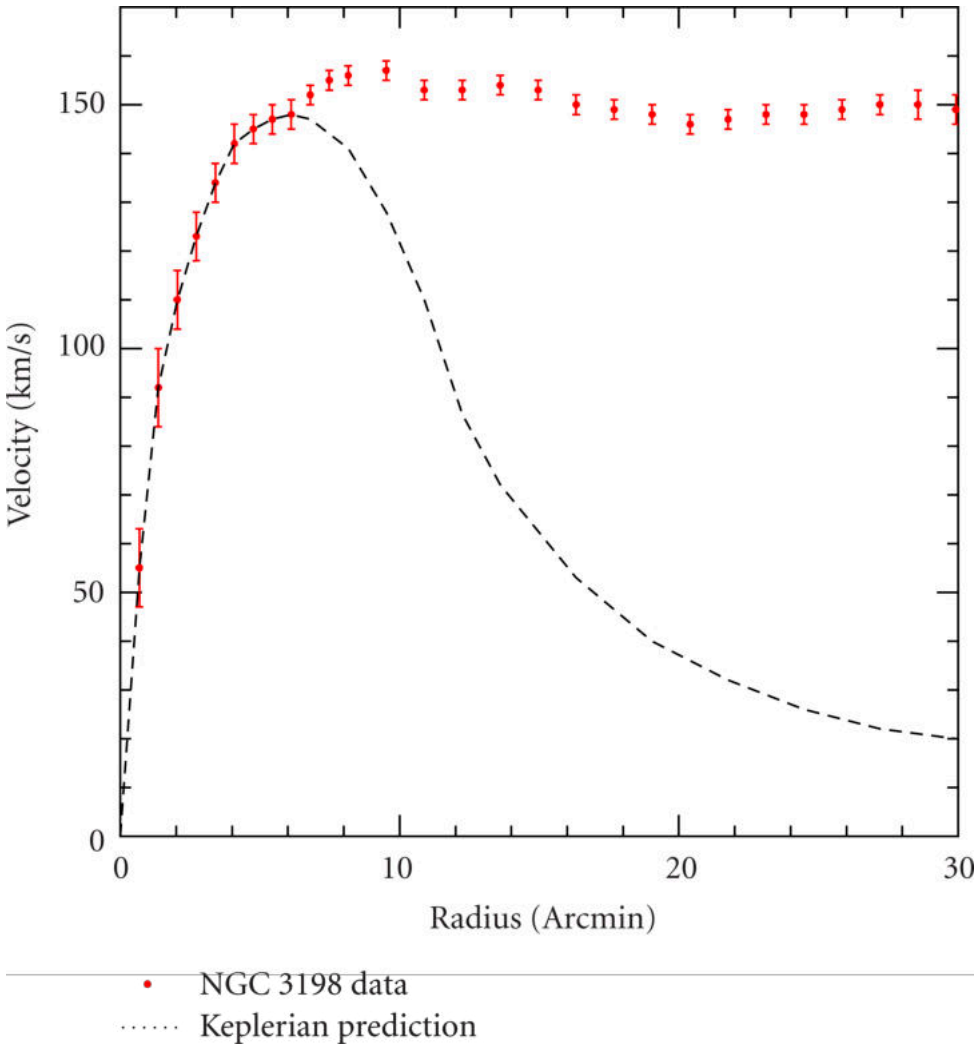

Figure 4: The measured rotational velocities of neutral atomic hydrogen (HI) regions in NGC 3198 are compared to an idealized Keplerian behavior. [6]

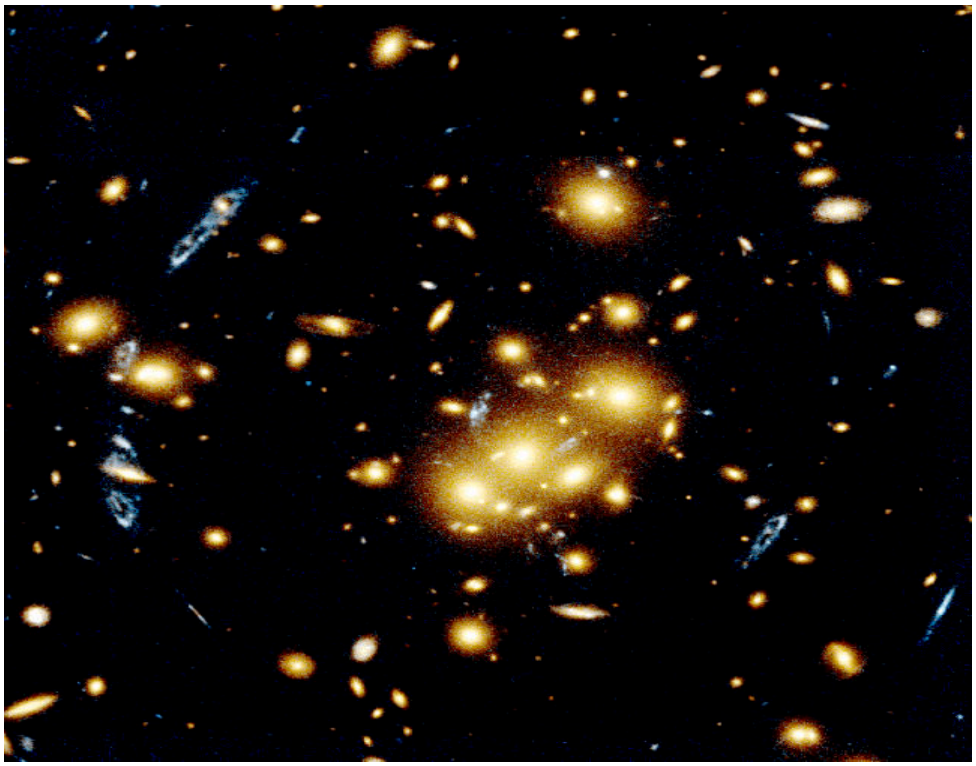

Figure 5: CL0024+1654 [31]: Hubble image shows looping blue objects, multiple images of a galaxy, created by a cluster of yellow galaxies. Reference [32] provides a detailed description of the phenomenon mentioned.

Bullet Cluster

The existence of DM is also supported by the observations of the 1E0657-56 galaxy cluster, also known as the *Bullet* cluster. X-ray observations of this cluster reveal a collision between a larger galaxy cluster and a smaller *bullet* one (see Figure 6). These findings, described in Reference [33], involved a comparison between emission spectra and the mapping of mass distributions derived from gravitational lensing studies. Figure 6 (a) illustrates the results of gravitational lensing studies conducted on the merging cluster. In Figure 6 (b), the X-ray spectrum reveals a cone on the right side. This cone is attributed to the emissions of ordinary baryonic matter[6] in the form of highly-energetic gases. These emissions match the expected shape and intensity resulting from such a collision.

By overlapping the two images, it becomes apparent that the majority of the mass content of the galaxies is displaced with respect to the electromagnetic emissions. This suggests that the DM halos of the two galaxies interacted weakly during the collision and continued moving in their respective directions.

[6] Ordinary baryonic matter, that is, matter made up of protons and neutrons.

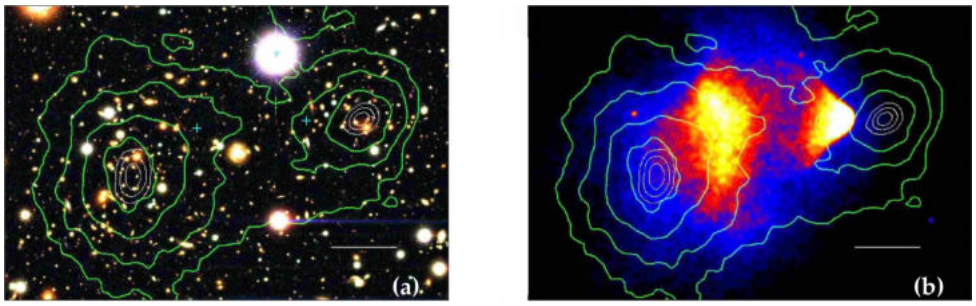

Figure 6: The merging cluster 1E0657-56: the visible (a) and the X-ray (b) images. The colors in image (b) represent the X-ray temperature of the plasma, where blue indicates the coolest temperatures and white represents the hottest temperatures. Additionally, the green contours correspond to the weak lensing reconstruction. [33]

1.3.2 The Cosmic Microwave Background and the ΛCDM model

The Cosmic Microwave Background (CMB) is a nearly uniform and isotropic source of low-energy photons at the eV level present throughout the observable universe. It was discovered in 1964 by the works of Arno Penzias and Robert W. Wilson [34], and its detection has since provided evidence supporting the Big Bang theory.

The present understanding of the Universe and its evolution is condensed in what is known as the ΛCDM model, whose framework is based on the Einstein field equations [35]. These equations establish a connection between the geometry of space-time and the energy content of the Universe. Additionally, they encompass a constant term, referred to as the *cosmological constant* Λ, which was first introduced to obtain a stationary solution for the Universe [29]. The discovery of Hubble's law in 1929 [36] later disproved this hypothesis. However, the constant term remains one of the central parameters in the ΛCDM model.

The hypothesis of a homogeneous and isotropic Universe [37, 29] allows for the simplification of the Einstein equations, leading to the derivation of the two Friedmann equations [38]. The first Friedmann equation relates the expansion rate of the Universe to its total energy density (represented by Ω). On the other hand, the second Friedmann equation describes the temporal evolution of the energy density components.

The Friedmann equations enable the extrapolation of energy densities associated with matter, radiation, and constant components backward in time. This facilitates the reconstruction of a depiction of the primordial Universe as a function of a temperature parameter, T. According to this, it is concluded that the high energy density of initial conditions became diluted over time due to the expansion of the Universe.

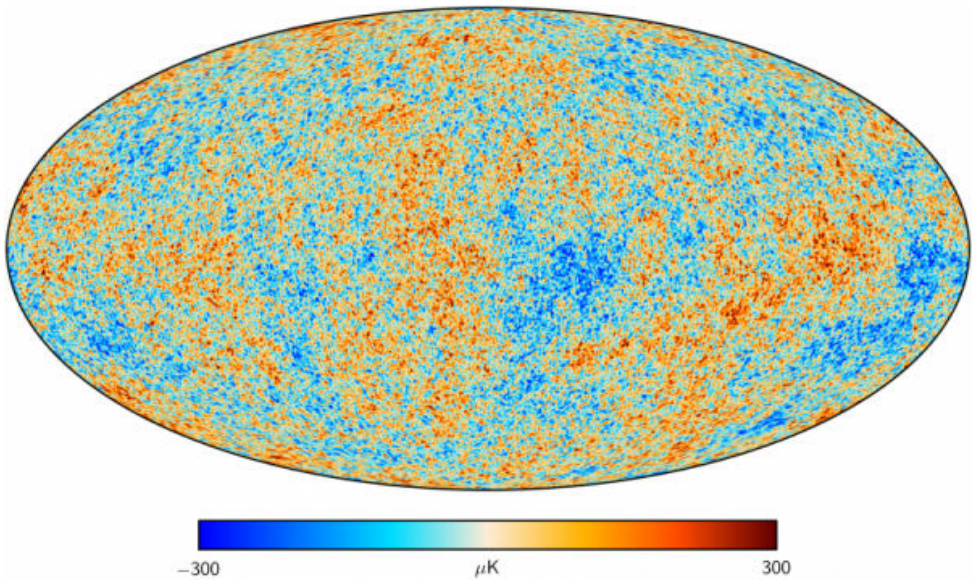

Figure 7: Map of the CMB temperature fluctuations measured by Planck. The color scale represents the deviations from the average temperature of around $^{\sigma T}/_{T} \approx 10^{-5}\ K$. [40]

The Universe began with an energy scale higher than the Planck scale, where quantum gravitational effects prevailed. The expansion of the universe diluted the energy density, leading to the electroweak symmetry era. This era ended with the breaking of the electroweak symmetry around $T \approx 10^2$ GeV. At energies around Λ_{QCD}, quarks and gluons started to form hadrons, while further expansion at electronvolt energies caused electromagnetic radiation and baryonic matter to decouple. The CMB represents this later stage and enables the study of matter distribution during that time [29].

Subsequent experimental observations of the CMB revealed that its spectrum now matches that of a black body with a temperature of approximately $2.726 \pm 0.010\ K$ [39]. Further studies conducted by the Planck collaboration, identified fluctuations in the CMB on the scale of hundreds of μK, as depicted in Figure 7.

Theses fluctuations are linked to the presence of gravity potential wells during the early Universe, allowing for the formation of galaxy structures. To explain this, the existence of a matter component that created gravitational wells is necessary. Additionally, this matter component must have decoupled from ordinary matter before the CMB era through a freeze-out mechanism (Section 1.3.3).

The observed temperature fluctuations in the CMB map can be described using the ΛCDM model, and is possible to extract cosmological parameters, such as the cosmological energy densities.

One such example is the total energy density Ω, which is defined as the sum of the various energy

density terms, ρ_x, normalized to the critical density, ρ_c[7],

$$\Omega = \sum_x \frac{\rho_x}{\rho_c} = \sum_x \Omega_x. \tag{1.30}$$

This convention allows for expressing the contribution of each component in terms of its fraction relative to the critical density. The Planck Collaboration [7] reports the corresponding values for the matter (m) and dark energy (Λ) density terms, which offer valuable insights into the individual contributions of these components,

$$\Omega_m h^2 = 0.1430 \pm 0.0011 \quad \text{and} \quad \Omega_\Lambda h^2 = 0.3107 \pm 0.0082. \tag{1.31}$$

Here, $h = H_0/100$ km s^{-1} Mpc^{-1} is the reduced Hubble constant. Additional terms, like the energy density of radiation or neutrinos, are currently of minimal significance. These results suggest that only 31% of the total energy component of the Universe is attributed to matter. Moreover, the matter density term can be further categorized into baryonic and non-baryonic components, and their measurements are obtained accordingly,

$$\Omega_b h^2 = 0.02237 \pm 0.00015 \quad \text{and} \quad \Omega_c h^2 = 0.1200 \pm 0.0012. \tag{1.32}$$

In this context, Ω_b represents the baryonic matter energy density, while Ω_c denotes the non-baryonic matter, specifically Cold Dark Matter (CDM). These observations indicate that approximately 16% of the matter component in the Universe can be attributed to ordinary baryonic matter, while the remaining portion is accounted for by the presence of CDM.

1.3.3 The Freeze-out Mechanism

The Freeze-out Mechanism is postulated as the cause behind the observed relic density of dark matter in the Universe [29]. Considering a stable, non-relativistic DM particle χ of mass m that is produced thermally during the early evolution of the Universe, the time-dependent evolution of its number density n in an expanding Universe is described by the Boltzmann equation [42]:

$$\frac{dn}{dt} = -3Hn - \langle \sigma v \rangle (n^2 - n_{eq}^2). \tag{1.33}$$

H is the Hubble parameter, which provides a measure of the universal expansion rate, $\langle \sigma v \rangle$ is the thermal average of the product between the particle velocity and the annihilation cross-section of DM particles into SM particles, and n_{eq} is the particle number density at the thermal equilibrium. Figure 8 illustrates the time evolution of the equation, depicting the variation of the particle number density n as a function of the ratio between the mass m of the DM particle and its initial density T, which is a proxy for "time" [42].

[7] ρ_c refers to the sum of all contributions to the energy density and pressure in the universe at $T = T_0$, denoting the earliest Universe [41].

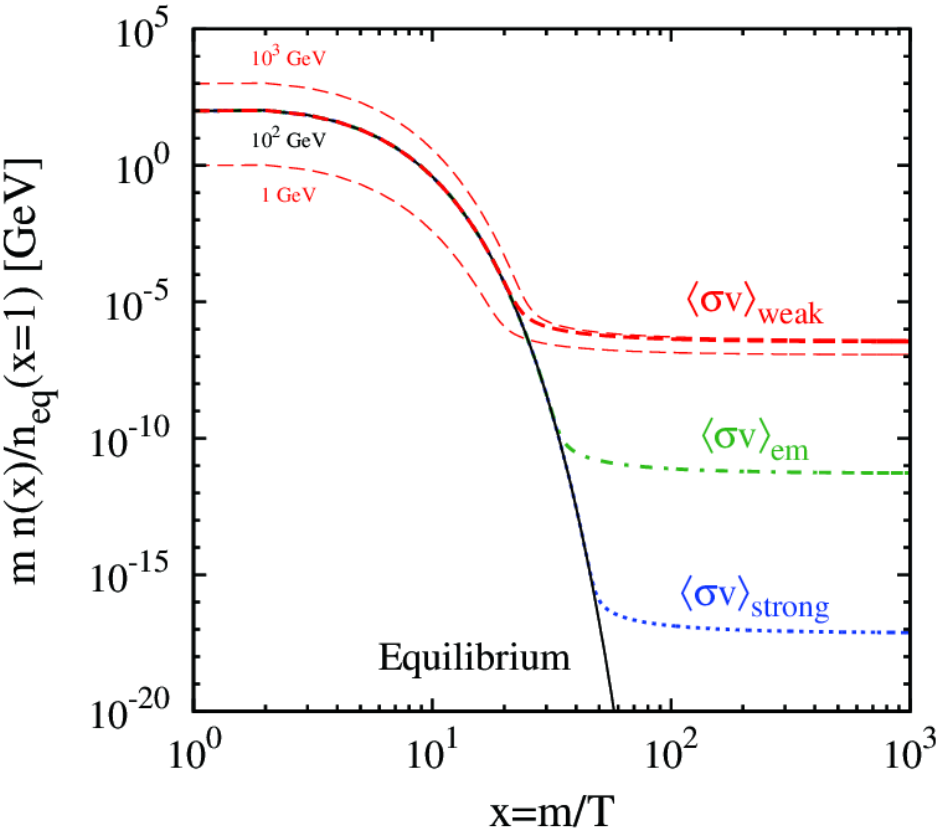

Figure 8: Evolution of DM Particle Number Density vs. $x = m/T$. The black line represents the equilibrium abundance for $m_\chi = 100$ GeV. Different colors indicate different hypotheses on the magnitude of the interaction cross-section σ, leading to distinct asymptotic constant values. [42, 29]

During the early stages of the Universe, when the energy density was such that $T \gg m$, the production and annihilation rates of particles surpassed the expansion rate determined by H. In this regime, the particle number density followed the expected equilibrium density. However, when the values of $T \leq m$, the production of DM particles through pair production was suppressed, and as a consequence, the annihilation rate was reduced due to the decreased production rate of DM particles. Once this process came to a halt, the evolution of the particle number ceased, leaving behind a relic density of DM particles.

The final value of this density is directly proportional to the scale of the interaction cross-sections, with the weak interaction cross sections specifically matching the observed cosmological density of dark matter when considering particles with masses in the GeV/TeV scale [29].

1.3.4 Weakly Interacting Massive Particles

Constraints imposed by cosmological observations on particle candidates for DM can be summarized as follows:

1. The mass and interaction cross-section of DM candidates must result in a relic density consistent with its measured value;

2. DM candidates must be stable or long-lived, as they were produced in the early Universe and their effects persist to this day;

3. DM candidates must be neutral under all SM forces.

In the SM, with the exception of neutrinos, no particles satisfy the aforementioned criteria. Additionally, the observed evidence supports the existence of CDM, ruling out relativistic neutrinos. Therefore, the need for new phenomena arises. Weakly Interacting Massive Particles (WIMPs) have been proposed as a natural solution that fulfills these requirements [29]. WIMPs are expected to have interaction cross-sections comparable to electroweak processes. Consequently, their mass is anticipated to be in the range of GeV to TeV, which conveniently falls within the sensitivity region of several experiments, including the LHC.

WIMP Search Strategies

The searches for Weakly Interacting Massive Particles are commonly classified into three categories:

1. *Direct Detection* experiments search for low-background nuclear recoils and assume a scattering interaction $\chi + \text{SM} \rightarrow \chi + \text{SM}$;

2. *Indirect Detection* experiments aim to identify an excess in the production of SM particles or high-energy photons resulting from the annihilation processes of DM particles $\chi + \chi \rightarrow \text{SM} + \bar{\text{SM}}$.

3. *Collider Detection* searches aim to produce pairs of WIMPs in high-energy collisions of SM particles. To identify the presence of WIMPs, collider experiments rely on detecting associated phenomena involving SM particles, enabling the tagging of events.

The work on this thesis mainly focuses on *Collider Detection* searches. Specifically, exploring the feasibility of generating WIMP DM candidates through the presence of a new mediator particle Y, which interacts with both the SM particles and an additional dark sector. In order to identify these elusive final states, it is crucial to create them alongside one or more SM particles, enabling their detection and identification.

1.3.5 Simplified Dark Matter Models

To study these phenomena, the concept of Simplified Dark Matter Models, as discussed in the literature [43, 8], is adopted. These models introduce the possibility of the existence of a new boson with either

spin-0 or spin-1, which mediates the interaction between WIMPs and SM particles.

The predicted interactions in these simplified models are carefully constructed to uphold the conservation of both exact and accidental symmetries of the SM, such as the preservation of leptonic and baryonic numbers. Imposing the requirement of Minimal Flavour Violation (MFV) allows for the avoidance of significant constraints on the allowed parameter space, ensuring that any additional interactions in the quark sector maintain the flavor symmetry of the SM or adhere to the observed quark Yukawa matrices in the SM Higgs sector [29].

These models are termed "simplified" because they rely on a small number of parameters to describe the relevant dynamics. These parameters include the mass of the WIMP DM candidate and the new mediator, as well as the couplings of the mediator with the SM and WIMP candidate. Furthermore, these models consider only one type of new interaction at a time. It is also postulated that the masses of WIMPs and the new mediator are generated through a dark Brout-Englert-Higgs mechanism, which is not explicitly accounted for in the predicted interactions with SM particles.

Spin-0 Mediator Model

The present thesis builds upon the theoretical framework proposed in prior studies [8, 43, 44], and adopts a version of the DM simplified model originally introduced by Backović et al. [13]. The primary focus of this work revolves around conducting a comprehensive phenomenological study of the interactions between a DM spin-0 mediator and the top quark, as elaborated in the forthcoming chapters of this thesis.

The Spin-0 Mediator Model (`DMSimp_spin_0`) proposed by [13] denotes the spin-0 mediator as Y_0. In this framework, the WIMPs DM candidates are considered to be massless Dirac fermions (X_D), and their interaction with the SM occurs via the exchange of the mediator Y_0, which corresponds to a new field. This new field can take the form of either a scalar or a pseudo-scalar.

In this scenario the interaction component of the Lagrangians is defined as follows:

$$\mathcal{L}_{Y_0}^{X_D} = \bar{X_D}(g_{X_D}^S + ig_{X_D}^P\gamma^5)X_D Y_0, \tag{1.34}$$

$$\mathcal{L}_{SM}^{Y_0} = \sum_{i,j}\left[\bar{d_i}\frac{y_{ij}^d}{\sqrt{2}}\left(g_{d_{ij}}^S + ig_{d_{ij}}^P\gamma^5\right)d_j + \bar{u}_i\frac{y_{ij}^u}{\sqrt{2}}\left(g_{u_{ij}}^S + ig_{u_{ij}}^P\gamma^5\right)u_j\right]Y_0 \tag{1.35}$$

In the interaction Lagrangian between the mediator and the SM particles $(\mathcal{L}_{SM}^{Y_0})$, the sum runs over the three generations of up- (u_i) and down-type (d_i) quarks. $y_{ii}^f = \sqrt{2}m_f/v$ is the Yukawa coupling of the i^{th} quark. To meet the MFV constraint, a Yukawa-like interaction is necessary [29]. This thesis focuses on processes of the form $pp \to t\bar{t} + Y_0$ where a DM mediator is produced in association with a pair of top quarks.

Mediator Type	$g^S_{X_D}$	$g^P_{X_D}$	$g^S_{u_{33}}$	$g^P_{u_{33}}$
Pure Scalar	1	0	1	0
Pure Pseudo-scalar	0	1	0	1

Table 3: In both scenarios, the remaining components in the Lagrangian, pertaining to the other quarks, are set to zero according to the specifications outlined by [13].

The coupling constant between the mediator and particles in the SM is defined by the parameters $g^{S/P}_{u_{ij}}$ and $g^{S/P}_{d_{ij}}$, while the interaction strength between the new mediator and DM particles (X_D) is parameterized by $g^{S/P}_{X_D}$. The scenarios of a pure scalar $(J^{CP} = 0^+)$ and pure pseudo-scalar $(J^{CP} = 0^-)$ mediator coupling with a top quark pair can be achieved by setting the parameters in the Lagrangian to specific values (see Table 3). To allow for a long lived and stable mediator, it is important to note that a null decay width is assumed $(\Gamma_Y = 0)$.

Chapter 2

The LHC and the ATLAS Detector

A comprehensive description of the experimental setup used to study the production and phenomenology of Dark Matter is presented. Section 2.1 provides a description of the LHC (Large Hadron Collider) and its operation. The LHC was specifically constructed to collide protons or heavy ions, aiming for a target center-of-mass energy of 14 TeV and 5.6 TeV, respectively. With the ongoing *LHC Run 3* presently underway, extensive prospects arise for the exploration of new physics phenomena, and in particular for Dark Matter. The subsequent section delves extensively into the ATLAS detector (in Section 2.2), one of the LHC experiments where proton-proton collisions take place. A detailed overview of its subsystems facilitates a better understanding of multi-purpose detectors, such as ATLAS. The ATLAS experiment holds special significance in this thesis over the other experiments as the studies presented here, use a fast simulation of the ATLAS detector. The package employed for this purpose was `DELPHES` [11, 12], and its framework is discussed in Section 2.3.

2.1 The Large Hadron Collider

The Large Hadron Collider, located at the Accelerator Complex of CERN near Geneva, Switzerland, is currently the world's largest and most powerful particle accelerator [45], comprising a 27 km circumference of superconducting magnets buried at roughly 100 m bellow the surface.

Two counter-rotating beams of proton bunches[1] are accelerated in the beam pipe to high center of mass energies $\sqrt{s}$, and collided at four interaction points. At these points, four major experiments are installed: The ALICE [46], LHCb [47], ATLAS [10] and CMS [48], being the last two general-purpose detectors built to cover nearly the whole solid angle [14].

Collisions between proton bunches occur at a rate of every 25 ns at the interaction points. Every LHC bunch contains, typically, around 10^{11} protons.

[1] in some cases, heavy ion

Before the proton bunches are produced and reach the desired collision energy, they undergo a series of acceleration stages embedded within the LHC complex. First, protons are produced from an ionized hydrogen gas using an ion source technique called Duoplasmatron. Then, they are accelerated to 160 MeV using LINAC4, and injected into the Proton Synchrotron Booster, where the energy of the protons is further boosted to 2 GeV.

Protons are then injected into the 628 m diameter Proton Synchrotron, which not only accelerates them to 26 GeV, but also bunches the protons, before sending them to the Super Proton Synchrotron (SPS), in which the desired injection energy of 450 GeV is achieved. Finally, the proton bunches are split into two beams, and fed into the LHC collider, where they are accelerated using 8 Radio-frequency (RF) cavities per beam. This cavities maintain an oscillating electric field which accelerates particles from 450 GeV to 6.8 TeV (7 TeV) [2] each time they pass by.

Presently, the LHC comprises 1232 superconducting dipole magnets, all of which are helium-colled down to 1.9 K. This setup is able to generate a magnetic field of up to 8.3 T [49].

Additionally, one can find supplementary magnets, quadrupoles, and correctors positioned along the ring, that allow for the focusing and confinement of the beams to their optimal trajectories.

2.1.1 Machine Specifications

Since the commencement of the LHC operation in 2008, its activities have been staged between Run and Long Shutdown (LS) periods (see Figure 10). *LHC Run 1* was the first fully operational run that lasted between the end of 2009 and the early beginning of 2013. Over that period, proton-proton collision data was produced at $\sqrt{s}$ =7 and 8 TeV [51].

For the remainder of 2013 until the beginning of 2015, the *LS1* took place. During that period, the LHC and its detectors were upgraded, and the center of mass energy of pp collisions was increased to 13 TeV. This was the energy adopted for the *LHC Run 2*, which subsequently ran from 2015 until the end of 2018 [52].

After the completion of *LHC Run 2*, the LHC entered once more in a long shutdown period, the *LS2*. This maintenance primarily focused on achieving the maximum collision energy possible of 14 TeV, for which the LHC was designed [53, 54]. Ultimately, this target has not yet been achieve, and the collision energy is currently settled at 13.6 TeV for the remaining part of *LHC Run 3*, which started in 2022.

The *LHC Run 3* is currently ongoing in 2023, and is expected to conclude sometime in 2025 [55].

[2] For the *LHC Run 3 (High-Luminosity Phase of the LHC)*.

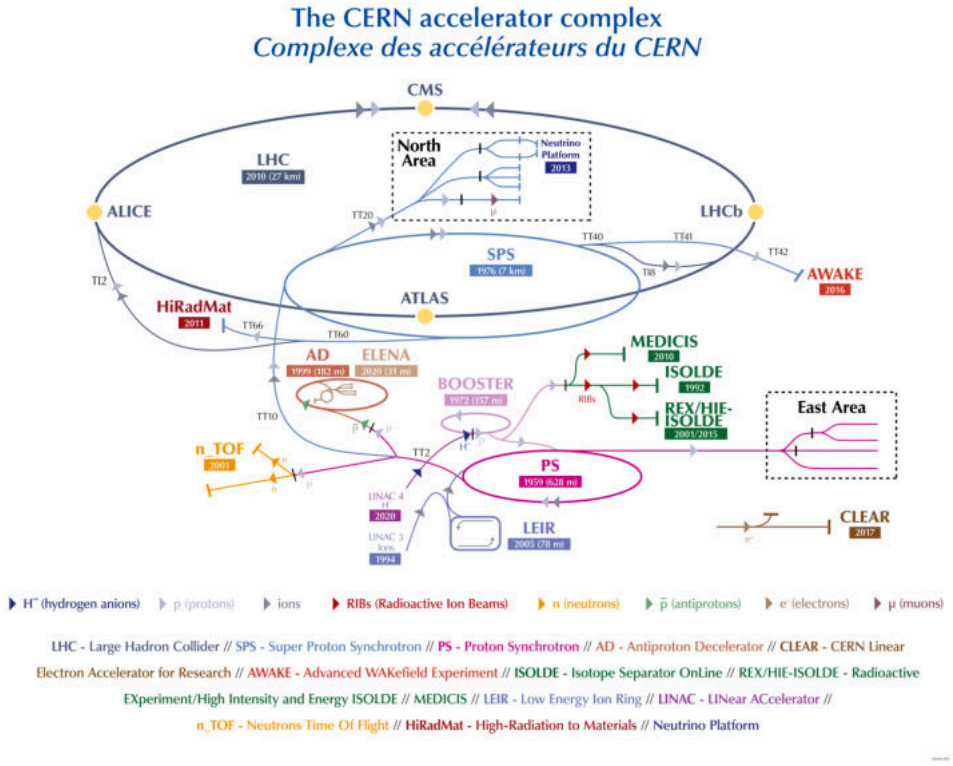

Figure 9: The CERN accelerator complex in 2023. This schematic illustrates the detailed acceleration chain that protons undergo. [50]

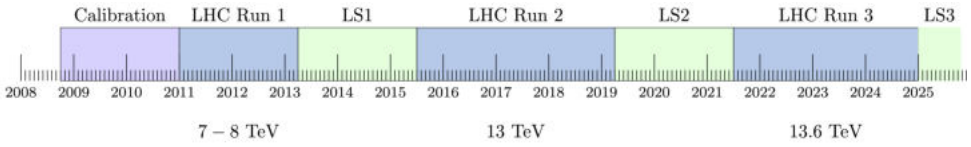

Figure 10: The LHC Schedule, with a timeline of Run and LS periods to date.

Parameter	Description
N	Number of protons per bunch
n_{b_p}	Number of proton bunches per beam
f	Bunch frequency
σ_x, σ_y	Root mean square of the beam sizes in the transverse plane.
Λ	Geometrical factor

Table 4: The following is a description of the parameters appearing in the equation 2.2.

Luminosity

The number of proton-proton collisions per second for a given process, $pp \rightarrow X$, is directly proportional to its interaction cross-section $\sigma_{pp\rightarrow X}$ [3]:

$$\frac{dN_{pp\rightarrow X}}{dt} = \mathcal{L}\sigma_{pp\rightarrow X}. \tag{2.1}$$

The constant of proportionality, $\mathcal{L}$, is known as instantaneous luminosity. It can also be expressed solely in terms of the parameters of the beam:

$$\mathcal{L} = \frac{N^2 n_{b_p} f}{4\pi\sigma_x\sigma_y}\Lambda. \tag{2.2}$$

Table 4 provides a concise summary of the parameters referenced in Equation 2.2.

As Equation 2.1 illustrates, a higher instantaneous luminosity $\mathcal{L}$ leads to an increased likelihood of particle collisions. Nonetheless, when multiple collisions occur in close proximity in time, it can be strenuous to distinguish between particles originating from different collisions. Consequently, a selective event trigger system embedded within the detectors is vital.

Another important concept arises from the definition of instantaneous luminosity that is the integrated luminosity ($\mathcal{L}_{int}$), which defines the total amount of data collected over a defined period of time, and is calculated by integrating the instantaneous luminosity over that time span.

Luminosity for the LHC Run 3 Initially, the LHC was designed to deliver a nominal instantaneous luminosity of 10^{34} cm^{-2}s^{-1}. This value has been surpassed in *LHC Run 2*, with experiments recording values up to 2×10^{34} cm^{-2}s^{-1} [56], which is also the maximum instantaneous luminosity achievable with the current *Run 3* configuration of the LHC [57].

[3] This cross-section is normally measured in *barn* ($1b = 10^{-24}$ cm^2)

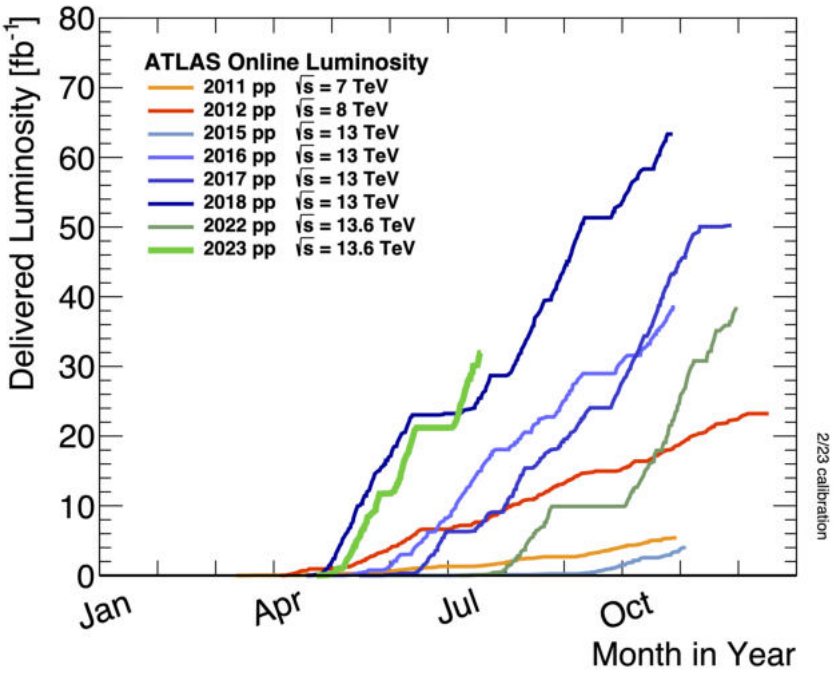

Figure 11: Integrated luminosity delivered to the ATLAS experiment during stable proton-proton collisions over the years. The values vary per year as the specific parameters in the machine are tuned accordingly. [59]

.

Regarding the integrated luminosity $\mathcal{L}_{int}$ delivered to the experiment, the LHC plan is to achieve a total of around 300 fb^{-1} by the end of *LHC Run 3* at 13.6 TeV [57, 58].

As shown in Figure 11, the integrated luminosity delivered to the ATLAS experiment has increased significantly over the years. This defines the total number of particle collisions that have occurred during that period of time.

Pileup

As discussed earlier, high-energy proton bunches collide at the interaction points in the LHC. Just as the collision happens, multiple primary vertices are created when the bunches cross, due to their considerable size. This is commonly termed as *in-time pileup*. Additionally, there is also the *out-of-time pileup*, whereupon particles from previous bunch crossings still actively participate in the detected events. Although both types of pileup contribute to measurement inaccuracies, *in-time pileup* is more prevalent in the LHC.

Figure 12 displays the luminosity-weighted distribution of the mean number of interactions per crossing for proton-proton collisions at various center-of-mass energies over the years of LHC operation, including the 2022 preliminary run at 13.6 TeV [59]. As shown in the figure, the number of collisions per bunch

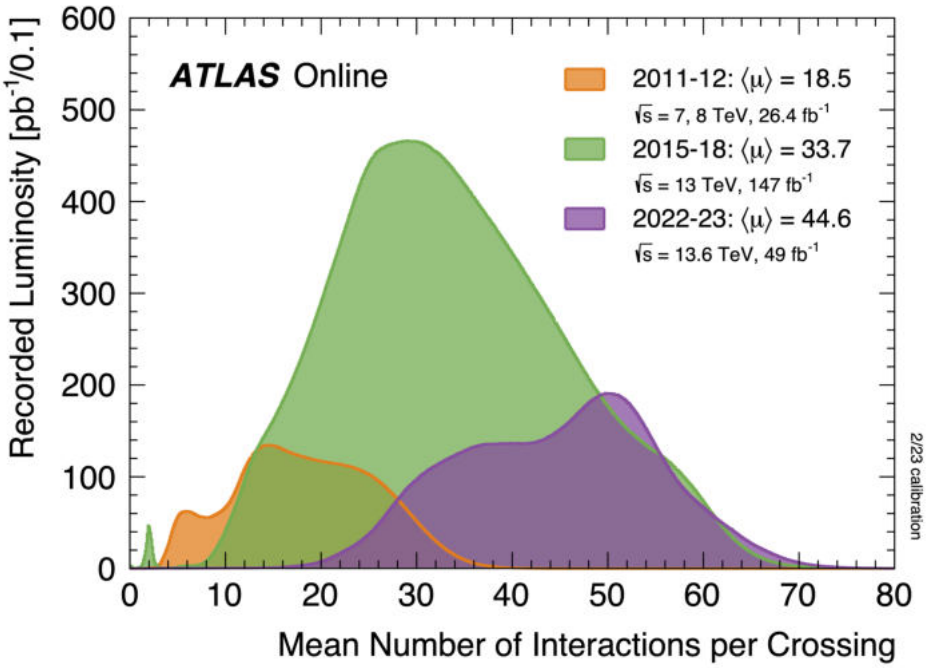

Figure 12: Mean number of interactions per crossing for proton-proton collisions over the different years of the LHC operation, in data collected by ATLAS [59].

crossing has risen significantly as the center of mass energy increased over time.

2.2 The ATLAS Detector

The ATLAS detector, located at the Interaction Point 1 (IP1), is the largest general-purpose detector at the LHC and has a broad physics program that includes searches for phenomena both within and beyond the SM [10]. The experiment comprises a cylindrical volume with a length of 46 meters and a diameter of 25 meters, which is filled with multiple layers of particle detectors arranged concentrically [10, 55].

This experimental setup, depicted in Figure 13, allows for the detection, classification, and reconstruction of different particle trajectories following proton collisions. In this section, the different subsystems of the ATLAS detector are described, starting with the Inner Detector (ID) and moving outwards through the calorimeter system to the muon spectrometer (MS). Each subsystem is introduced, highlighting its unique purpose and functional principles.

Coordinate System An important aspect regarding the ATLAS detector is its coordinate system. The detector adopts a right-handed Cartesian coordinates system with the origin at the interaction point. The $\hat{x}$ axis points towards the center of the LHC, and the $\hat{y}$ axis upwards. The $\hat{z}$ axis is directed along the

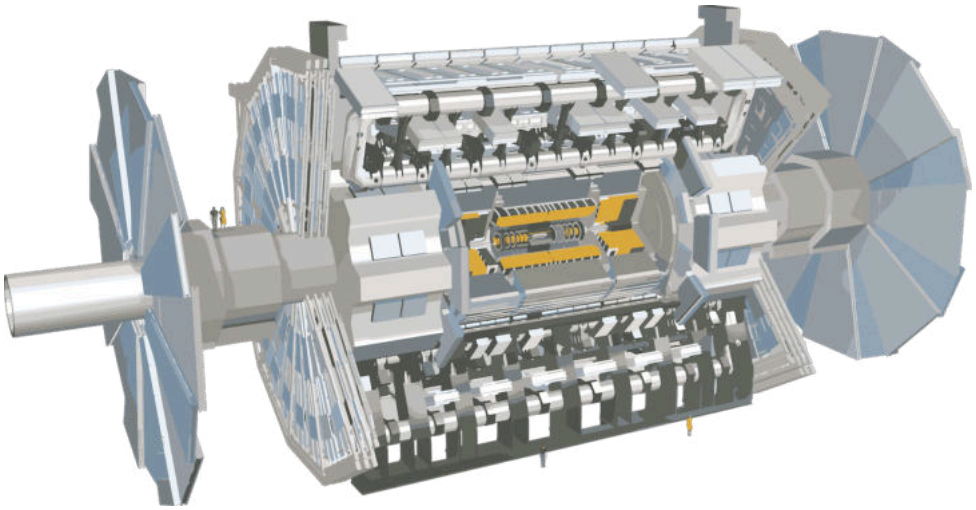

Figure 13: Schematic of the ATLAS experiment at the Large Hadron Collider (LHC), depicting the different components of the detector, including the inner detector, the calorimeters, and the muon spectrometer [60]

.

beam pipe.

Based on its rotational symmetry, the detector has standardized the use of spherical coordinates. (r, ϕ) for the transverse plane (x, y), with θ representing the polar angle around the $\hat{z}$ axis. These coordinates allow for the definition of pseudorapidity η, which can be expressed as:

$$\eta = -\ln\left(\tan\frac{\theta}{2}\right). \tag{2.3}$$

By considering the pseudorapidity and the azimuthal angle, a geometrical distance between two objects i and j in the (η,ϕ) plane can be defined as:

$$\Delta R = \sqrt{\Delta\eta^2 + \Delta\phi^2} = \sqrt{(\eta_i - \eta_j)^2 + (\phi_i - \phi_j)^2}. \tag{2.4}$$

This quantity is generally used to measure the spatial separation between energy deposits or reconstructed physics objects in the final collision states.

A schematic view of the ATLAS coordinate system, is represented in Figure 14, providing a visual reference for the concepts discussed.

2.2.1 Inner Detector

The Inner Detector (ID) [62, 63] represents the innermost layer of the ATLAS detector. Due to its proximity to the interaction point, the ID efficiently handles an extensive number of high-energy collisions. Within the Inner Detector, there is a uniform 2 T magnetic field, running parallel to the beam direction. This

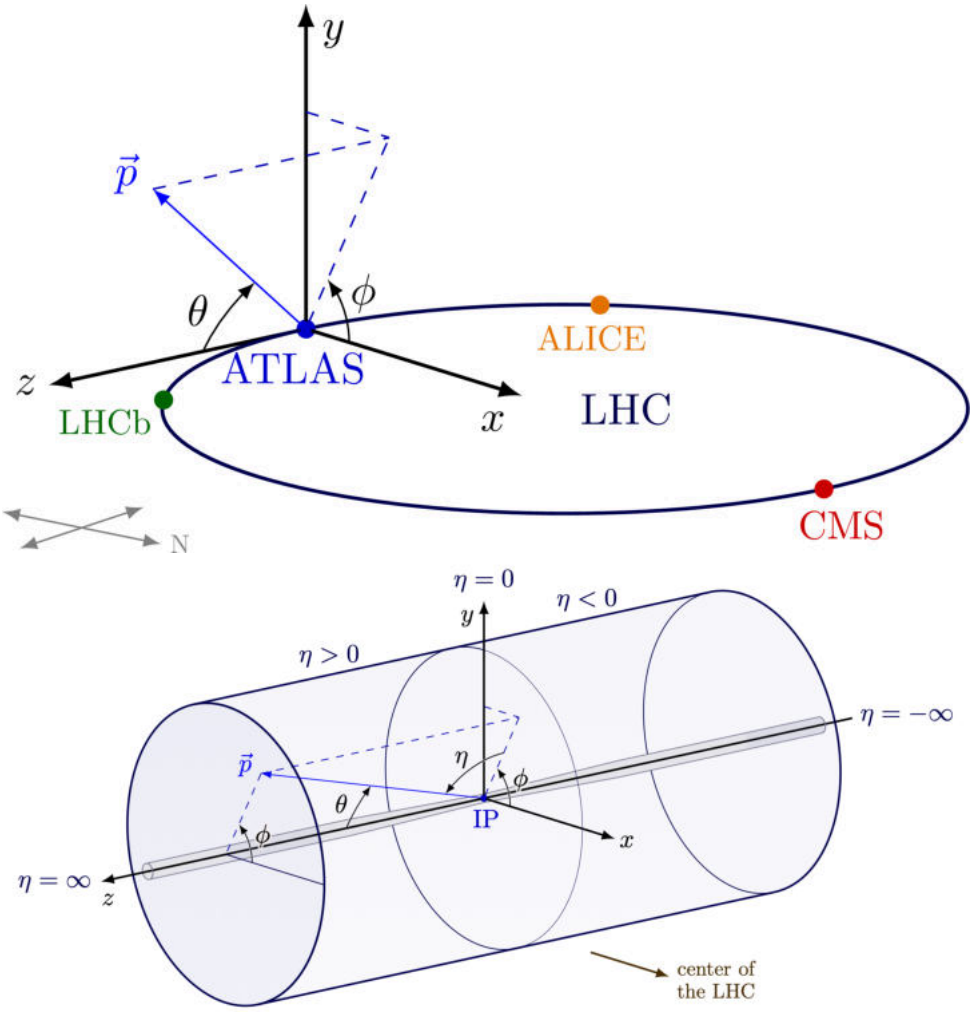

Figure 14: Pseudorapidity η is employed in the reconstruction process of physics objects for setting experimental cuts, benefiting from the Lorentz invariance of Δy (corresponding to $\Delta\eta$). [61]

magnetic field is generated by a superconducting solenoid that envelops the ID. Its purpose is to facilitate the measurement of particle momentum and charge by deflecting the paths of charged particles. This deflection allows for the accurate determination of their charge and momentum as well as enabling a precise reconstruction of their interaction vertices.

The ID system can be viewed as a combination of three subsystems: the pixel detector, the semiconductor tracker (SCT), and the transition radiation tracker (TRT), each with structures casing the barrel region and the end-cap regions.

Pixel Detector

The pixel sensors in the barrel region are arranged in four cylindrical layers commencing from a minimum distance of 33 mm[4], and extending up to 122.5 mm from the beam line. In the end-cap region, additional detectors are assembled in disks, oriented perpendicular to the $\hat{z}$ axis. These regions utilize millions of high-granularity silicon semiconductor sensors, which provide the finest points for vertex reconstruction and effectively separate primary vertices from secondary vertices.

Semiconductor Tracker (SCT)

The Semiconductor Tracker is constructed around the pixel detector and incorporates silicon microstrips that are arranged in four coaxial cylindrical structures around the beam line. Additionally, there are nine disks on each side of the end-cap region, with their strips aligned radially. This setup allows the measurement of particle tracks when the collisions occur.

Transition Radiation Tracker (TRT)

The Transition Radiation Tracker serves as the outermost layer of the Inner Detector. It consists of approximately 300,000 thin-walled drift tubes, commonly referred to as straws, each with a diameter of 4 mm. Embedded within each straw is a gold-plated tungsten wire.

Additionally, each straw contains a mixture of a noble gas, typically Argon (Ar) or Xenon (Xe). When a charged particle traverses the straw, the gas mixture becomes ionized, leading to the generation of an electric signal that can be detected. This electric signal is crucial for reconstructing the path of the particle.

Furthermore, if the velocity of the charged particle exceeds the threshold for transition radiation, it emits photons as it crosses different media. Notably, the amount of transition radiation emitted correlates with the mass of the traversing particle. As a result, this phenomenon, within the TRT, enables the differentiation

[4] After the installation of the Insertable B-layer (IBL) during the *LHC LS1*. [64]

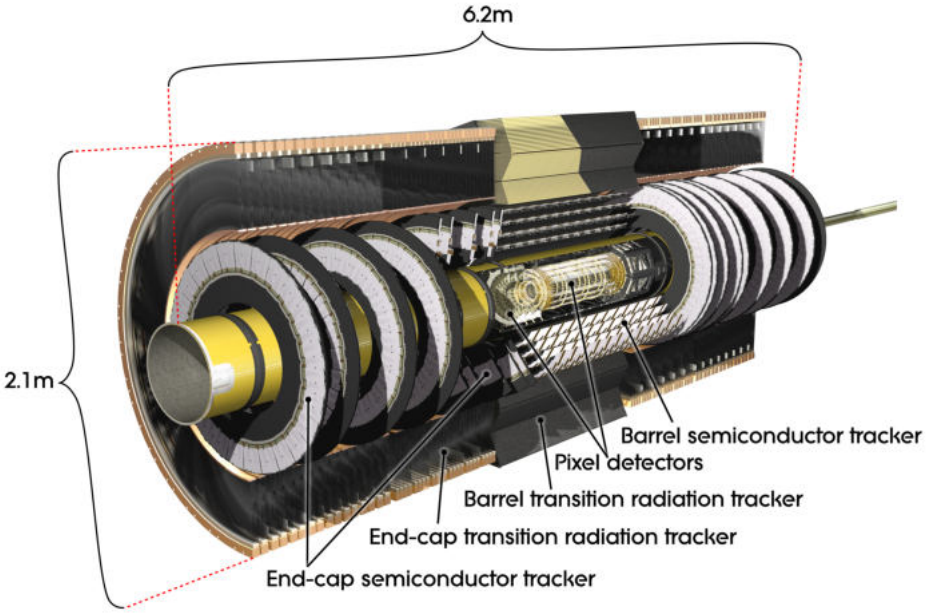

Figure 15: A labeled cutaway view of the Inner Detector (ID). The image demonstrates the ID configuration prior to the inclusion of the innermost pixel layer. [65, 64]

between electrons and heavier particles, like charged pions.

The TRT is strategically designed with 50,000 individual straws in the barrel region, each with a maximum length of 144 cm. In addition, the end-cap regions house a distribution of 250,000 straws, but with a shorter length of 39 cm. This meticulous arrangement results in a spatial resolution of 170 μm per readout channel.

For a visual representation of the Inner Detector (ID) and its constituent components, see Figure 15.

To summarize its capabilities, the Inner Detector (ID) system is designed to reconstruct particle paths within the specified range of $|\eta| \leq 2.5$ and $p_T > 0.4$ GeV[5].

The combined information from all subsystems contributes to the determination of the transverse momentum resolution, according to:

$$\frac{\sigma_{p_T}}{p_T} = 0.05\% \cdot p_T \oplus 1\%. \tag{2.5}$$

The transverse momentum p_T is measured in GeV, and the $\oplus$ symbol denotes a sum in quadrature.

[5] The transverse momentum p_T represents the magnitude of the projection of the momentum vector of the particle in the plane perpendicular to the beam direction.

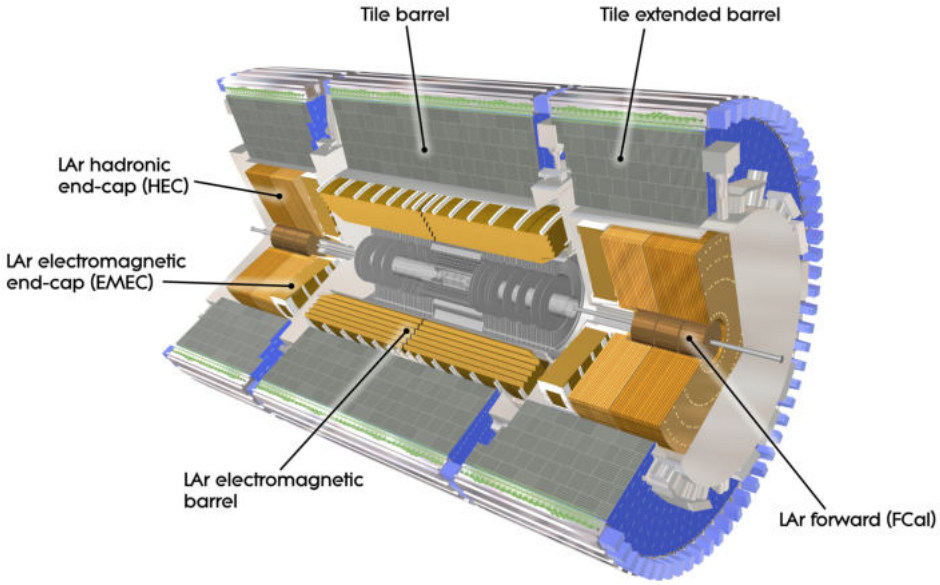

Figure 16: A labeled cutaway view of the Calorimeter System. [68]

2.2.2 Calorimeter System

Adjacent to the superconducting solenoid of the Inner Detector lies the Calorimeter System [66, 67], represented in Figure 16. This crucial component serves the purpose of measuring particle energy while determining their flight direction in a process known as destructive measurement. This involves the reconstruction of hadronic and electromagnetic showers, enabling accurate determination of particle energies and directions. The calorimeter system in ATLAS is able to provide coverage up to $|\eta| < 4.9$. The layout of the system is divided between the Electromagnetic Calorimeter (ECal) and the Hadronic Calorimeter (HCal), both of which are based on a sampling principle. This configuration incorporates alternating intervals of passive material that induce particle showering and active material that allows for energy deposition to be read out by electronics. As a result, the calorimeter system in ATLAS achieves complete containment of particle showers, enabling the detection and quantification of all interacting particles produced in collisions, while minimizing the likelihood of non-muon particles generating signals in the muon spectrometers.

Electromagnetic Calorimeter

The Electromagnetic Calorimeter, situated closer to the beamline, serves as the detector layer where primarily photons and electrons, deposit their energy and remain contained. It encompasses a barrel region within $|\eta| < 1.475$, and two end-cap regions situated on either side, effectively expanding the

coverage in the range of $1.375 < |\eta| < 3.2$. In the barrel region, the ECal resides within the cryostat alongside the central solenoid. It is composed of two half-barrels, with a separation of 4 mm, at $z = 0$.

The half-barrels are configured in an accordion shape, comprising layers of lead, liquid argon (LAr), and copper-deposited electrodes encased in kapton. This configuration ensures both complete and symmetric coverage in ϕ throughout the detector, precluding any gaps. The lead plates, characterized by their high density, serve as absorbers within the detector. This component facilitates the showering effect, ensuring that electromagnetic particles are effectively contained within the inner layers of the detector and do not penetrate into the outer regions. The liquid argon, serving as the active material, enables the generation of an electric current in the electrodes, which is subsequently detected and recorded. This phenomenon occurs as the particles passing through the liquid cause ionization of the argon atoms, leading to the flow of electrical charges.

Due to the sampling principle employed in the calorimeters of ATLAS, not all of the energy carried by particles in the shower is fully recovered. Instead, only a fraction of the energy is sampled and measured. Through precise calibration within the ECal, it is possible to achieve a comprehensive energy measurement and obtain a spatial distribution of the deposited energy.

Prior to its installation in the ATLAS experiment, the energy resolution of the electromagnetic calorimeter was assessed using test beams containing electrons. An energy resolution was achieved for the electromagnetic calorimeter of:

$$\frac{\sigma_E}{E} = \frac{10\%}{\sqrt{E}} \oplus 0.7\%. \tag{2.6}$$

The energy E is measured in GeV, and the $\oplus$ symbol denotes a sum in quadrature.

Hadronic Calorimeter

The Hadronic Calorimeter follows the electromagnetic calorimeter and is specifically designed to measure and contain the energy of hadronic particles that are not captured by the electromagnetic calorimeter. Similar to the electromagnetic calorimeter, the hadronic calorimeter employs a sampling principle to measure the energy deposition of transverse hadronic particles. The HCal comprehends three subsystems: the tile calorimeter located in the barrel region adjacent to the ECal, the LAr hadronic end-cap calorimeter consisting of two wheels per end-cap, and the LAr forward calorimeter, which is responsible for detecting and measuring energy deposition in the forward direction of the particle detector.

The tile calorimeter provides coverage for a range of up to $|\eta| < 1.7$, with inner and outer radii of 2.28 m and 4.25 m, respectively. It is divided into three separate barrels: the tile barrel, which covers the region of $|\eta| < 1$, and the two extended barrels, which encompass the range of $0.8 < |\eta| < 1.7$. Inside,

the tile calorimeter utilizes steel as the absorber material and scintillating tiles as the active material. This configuration, similar to the ECal, enables the production and detection of signals originated from particles interacting within the calorimeter. The scintillating tiles radiate UV light when charged particles cross them. This radiation, which is proportional to the energy of the particle, is then absorbed by the two optical wavelength-shifting fibers located at the edge of each tile. These fibers, organized into bunches, are connected to the photo-multiplier tubes (PMT) that convert the light into an electric signal for subsequent analysis.

The LAr hadronic end-cap calorimeter is positioned directly behind the electromagnetic end-cap calorimeter, with the two sharing the same cryostat as the LAr forward calorimeter. It covers a range of $1.5 < |\eta| < 3.2$ and is constructed with parallel copper plates alternated with layers of LAr, which act as the active medium. The copper plates maintain a pitch of 8.5 mm between them within the wheels. The two wheels, HEC1 and HEC2, each have an outer diameter of approximately 4 m and comprise 32 identical modules. The copper absorber plates have a thickness of 25 mm for HEC1 and 50 mm for HEC2, with the first plate in each wheel being half of the normal thickness [10, 69].

Lastly, the LAr forward calorimeter (FCal) completes the discussion on the hadronic calorimeter. It has the capacity to detect particles within the $3.1 < |\eta| < 4.9$ range. It is constructed as a cylinder-shaped structure embedded within the wheel structure of the hadronic end-cap calorimeter. The LAr forward calorimeter consists of three sub-modules: FCal1, FCal2, and FCal3, each with a thickness of 45 cm. FCal1 is specifically optimized for electromagnetic calorimetry and employs copper as the passive material. Its design ensures effective containment of electromagnetic showers. In contrast, FCal2 and FCal3 are primarily dedicated to hadronic calorimetry and utilize tungsten as the passive material. The electrode structure is composed of parallel rods and tubes arranged concentrically along the beam axis. The region between each tube and the inner rod acts as the active medium, filled with LAr.

The energy resolution for the tile calorimeter and the LAr hadronic end-cap calorimeter is expressed as:

$$\frac{\sigma_E}{E} = \frac{50\%}{\sqrt{E}} \oplus 3\%. \tag{2.7}$$

Meanwhile, the energy resolution for the LAr forward calorimeter is given by:

$$\frac{\sigma_E}{E} = \frac{100\%}{\sqrt{E}} \oplus 10\%. \tag{2.8}$$

In both cases, σ_E represents the energy resolution, E denotes the energy measured in GeV, and the symbol $\oplus$ represents a sum in quadrature.

2.2.3 Muon Spectrometer

The Muon Spectrometer (MS) assumes a crucial role within the ATLAS detector, addressing the unique characteristics of muons, which exhibit minimal interaction with other ATLAS components due to their heavy mass and low ionization properties. As the outermost component of the detector, the muon spectrometer is dedicated to detecting and reconstructing these particular particles. Operating within a magnetic field generated by superconducting toroids, the muon spectrometer benefits from precise tracking capabilities. This magnetic field is generated by a total of three toroids systems: one situated in the barrel region, offering a magnetic bending over the range of $|\eta| < 1.2$, and the remaining two located in each end-cap, performing the same function within the range of $1.0 < |\eta| < 2.7$. The end-cap toroids reach a peak magnetic strength of 3.5 T, while the barrel toroid maintains a magnetic strength of 2.5 T.

The MS comprises four distinct subsystems. One of these subsystems is the Monitored Drift Tube (MDT) subsystem, which is specifically designed for precise momentum reconstruction within the muon spectrometer. The MDT subsystem consists of chambers with three to eight layers of drift tubes. These chambers are filled with a mixture of carbon dioxide (CO_2) and argon (Ar), covering a pseudorapidity range of $|\eta| < 2.7$. With a spatial resolution of 80 μm per tube, the MDT subsystem operates on a principle similar to that of the TRT in the inner detector.

However, there are challenges posed by the high maximum drift time of 700 ns in the Monitored Drift Tube (MDT) subsystem. To mitigate this, the muon spectrometer incorporates the Cathode Strips Chambers (CSCs) as the subsequent subsystem. Specifically positioned in the innermost layer for $|\eta| > 2.0$, the CSCs offer a solution for achieving more precise tracking capabilities. This is primarily attributed to their capability to handle higher hit rates, with a maximum drift time of only 80 ns, and their superior time resolution.

Apart from the detection chambers, the muon spectrometer incorporates Resistive Plate Chambers (RPCs) and Thin Gap Chambers (TGCs) to enhance its triggering capabilities. These chambers offer significantly higher time resolutions, allowing for the differentiation of consecutive bunch crossings. While the Monitored Drift Tube (MDT) subsystem primarily provides measurements of the pseudorapidity, the azimuthal angle information is derived from hits registered in the RPCs.

Figure 17 depicts a schematic view of the Muon Spectrometer (MS) with the different components appropriately labeled, providing a clear visual representation of its structure and functionality.

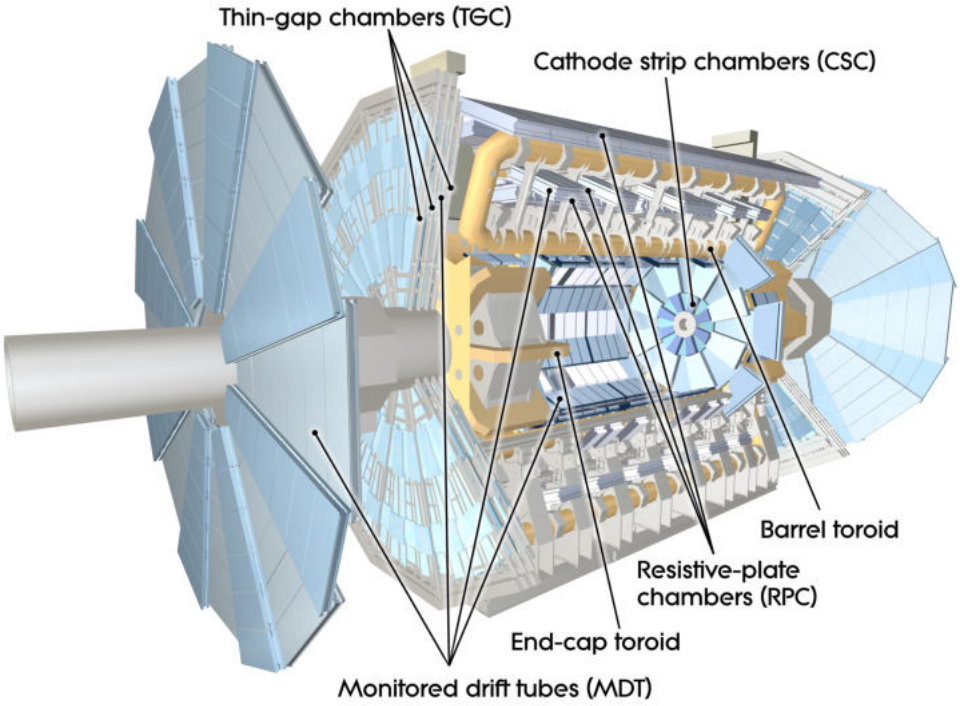

Figure 17: The chambers of the Muon Spectrometer in the ATLAS detector. [70]

2.2.4 Trigger System and Data Acquisition

Given the high luminosity at the LHC, storing and processing every collision event becomes infeasible due to limitations in computing resources and disk space [14]. To mitigate this challenge and alleviate the data overload, a real-time trigger system is implemented within ATLAS [71, 72]. This system selectively captures events of interest, typically characterized by high transverse momenta of particles (p_T) and relatively low cross-sections.

The selection process in the ATLAS system is performed in two stages by the trigger system: the Level-1 (L1) trigger and the High-Level (HLT) trigger.

The Level-1 trigger utilizes custom-designed electronics to analyze data from the trigger chambers in the muon spectrometer and the calorimeters[6]. It focuses on identifying particles such as muons, electrons, photons, jets, and τ-leptons with high transverse momentum (p_T). The system exhibits a low latency of around 2.5 μs, enabling it to promptly identify and designate regions of interest (*RoI*) within the detector. The entirety of data collected within these *RoI* is stored in memory buffers. This data includes the coordinates (η,ϕ) of the highlighted feature, along with its identification tracks and the employed selection criteria. The L1 trigger system processes events at a maximum rate of 100 kHz, which is lower than the original bunch crossing rate of approximately 40 MHz.

[6] The L1 trigger incorporates fast algorithms and reduced-granularity information from the calorimeters to facilitate this particle selection process.

The High-Level trigger is a software-based trigger that takes the *RoI* data provided by the L1 trigger and further analyzes it. It is capable of performing full object reconstruction if necessary, utilizing all the available information and complete granularity provided by the array of detectors located within the highlighted region of interest. It primarily employs offline analysis methods for its selection process, which effectively decrease the event rate. This reduction enables the permanent storage of data. On average, the HLT maintains an output rate of 1.2 kHz.

2.2.5 Particle Reconstruction in ATLAS

The ATLAS detector employs a comprehensive reconstruction process to transform signals acquired from collisions into precise representations of particle-like objects [73]. Electrons, muons, and photons are reconstructed as 4-vectors, undergoing stringent quality criteria to ensure their validity as candidates. Concurrently, hadron-like objects are identified as energy depositions within the calorimeter cells and are subsequently reconstructed as jets. These jet reconstructions establish a vital link between detector signals and the associated hadronic final states [18].

Electrons and Photons

The reconstruction of these particles begins at the aforementioned electromagnetic calorimeter (ECal), where an energy deposit is left as the electromagnetic (EM) particles traverse the medium. Simultaneously, the reconstructed tracks left by these particles in the inner detector (ID) are scanned to find the one that most closely matches the energy cluster in the ECal. Furthermore, the search for the corresponding matching photon conversion in the inner detector is taken into consideration when analyzing the particle candidate [74]. From the combined results of these searches, the energy cluster candidates can be distinguished between photons and electrons. Typically electrons carry an associated track, but no associated conversion, whereas the photons do not possess an associated track, but often are matched to a conversion.

Providing a more comprehensive overview, ATLAS incorporates a wide range of reconstruction parameters for electron identification. These parameters encompass various aspects, such as transition radiation hits on the track, the ratio of energy (measured by the calorimeter) to momentum (measured at the inner detector), and the comparison between the reconstructed coordinates (η and ϕ) from the energy cluster and those obtained through track extrapolation into the calorimeter.

In the analysis of high-p_T electrons, their energy is determined primarily from calorimeter measurements, while their direction (η and ϕ) is more precisely derived from matched tracks. For the identi-

fication of isolated high-p_T electrons, a combination of criteria is employed, including cuts on particle shower shapes and information from associated tracks. The specific selection of cuts depends on the requirements of each physics analysis, resulting in varying electron identification efficiencies and jet rejection rates. To achieve different levels of identification stringency, different sets of cuts are applied. For instance, *loose cuts* involve simple shower-shape criteria and relaxed matching between reconstructed tracks and calorimeter clusters. Conversely, *tight cuts* enforce stricter track-matching criteria and energy-to-momentum ratio thresholds. Additionally, calorimeter energy isolation beyond the electron cluster itself can be mandated to further enhance electron isolation.

In the case of photons, their direction (η and ϕ) as well as their energy can be determined primarily from the energy deposits in the calorimeters. However, distinguishing between photons and the jet background produced in the calorimeters can be challenging. To address this issue, ATLAS has developed and refined an optimized set of cuts for photon identification. These cuts are designed to effectively constrain the shower shapes produced in the calorimeter, with a particular focus on separating single neutral pions from photons. This separation is aided by the fine granularity of the silicon strip layer, which allows for precise tracking in the η direction.

Muons

The process of muon reconstruction integrates track information from the inner detector (ID) and the muon spectrometer (MS), allowing for accurate muon identification and momentum measurement. The reconstruction can be supplemented by incorporating calorimeter signals that exhibit energy deposits consistent with minimum ionizing particles (MIP) [18, 75].

The muon spectrometer alone achieves its highest resolution for muons with a transverse momentum of approximately 100 GeV. However, for muons with p_T lower than 100 GeV, combining the information from the muon spectrometer with the inner detector yields better resolutions. Specifically, when the p_T falls below a threshold of 30 GeV, the capabilities of the inner detector alone provide a sufficiently good resolution for computing momentum measurements. The toroidal field employed in the muon spectrometer ensures excellent momentum resolution, even at the highest values of η.

When conducting momentum measurements, the muon tracks within the spectrometer are traced back to the interaction point (IP). However, to account for the energy lost by the muon in the calorimeters, a momentum correction is necessary. This correction is performed using an algorithm that utilizes a parameterized expected energy loss, obtained from Monte Carlo simulations. Alternatively, if the muon track is isolated and the measured energy loss exceeds the expected loss based on the parameteriza-

tion, the measured energy loss can be employed instead. This approach ensures accurate momentum measurements by considering the actual energy deposition of the muon.

Jets

The partons, which originated from the initial scattering event, undergo hadronization producing hadrons that can be detected by the calorimeters. As a result of this phenomenon, collimated sprays of particles, commonly referred to as jets, are formed. These jets, comprising charged and neutral hadrons, can be detected and subsequently reconstructed [18].

In the context of the LHC, different jet reconstruction algorithms are employed based on the specific physics analysis requirements. One commonly used algorithm in the ATLAS experiment is the anti-k_T clustering algorithm [76]. Within this algorithm, the ΔR parameter is typically considered when analyzing jets, with a default set of parameters commonly used: $\Delta R = 0.4$ for narrower jets and $\Delta R = 0.6$ for wider jets. After applying the clustering algorithm, a calibration step follows. Jet-clustering algorithms have the flexibility to accept various object collections as input for jet finding, provided that these objects possess defined directions and energies.

In most ATLAS analyses, the preferred approach involves utilizing locally-calibrated three-dimensional topological clusters, known as topo-clusters, which are constructed from calorimeter cells [77, 73]. The topo-clustering procedure begins by identifying seed cells with an energy significance 4σ above the noise level, where the noise is calculated as the quadrature sum of electronic and pile-up noise. Subsequently, neighboring cells with an energy significance higher than 2σ are progressively added to form seed clusters. An additional ring of directly neighboring cells is incorporated into the final clusters. Following the identification of topo-clusters, a splitting algorithm is employed to further segregate clusters based on local energy maxima within each cluster.

Missing Transverse Energy

When protons collide in the LHC, they give rise to partons. These partons often carry different fractions of momentum compared to their mother particles, the protons. As a result, subsequent interactions and collisions between them seemingly violate the principle of conservation of momentum, as the sum of the momentum of their daughter particles does not add up to zero. This discrepancy in momentum conservation, specifically in the transverse plane, leads to the extensive utilization of transverse quantities in hadron collider experiments, such as the LHC.

One can think of the Missing Transverse Energy ($\not{E}_T$) as the negative vectorial sum of all p_T values

from the detected particles:

$$\not{E}_T = -\left| \sum_{i \in \text{tracks}} p_T(i) \right|. \tag{2.9}$$

In the case of non-detected particles with significant energy, the missing transverse energy must approximately correspond to the transverse component of the sum of their momenta.

In ATLAS, the missing transverse energy is calculated using information from both topo-clusters, and reconstructed muons [73, 78]. The contribution of muons to the missing transverse energy is determined solely based on the momentum measurement obtained from the muon spectrometer. This approach ensures that energy losses of muons in the calorimeters are not double-counted, as they only contribute to the $\not{E}_T$ through the calorimeter term. Occasionally, in events featuring highly energetic jets, numerous constituents of the jets can reach the muon spectrometer, leading to the identification of a "fake" muon. To mitigate this undesired effect, the selection process focuses only on muons that are successfully matched to an inner detector track.

Following the contribution from the muons, a correction in the form of the cryostat term is employed. This term accommodates for the energy losses that occur when particles traverse the cryostat between the electromagnetic calorimeter (ECal) and the hadronic calorimeter (HCal).

Lastly, a meticulous ordering of high-p_T reconstructed objects is conducted, and each object is then associated with its globally calibrated calorimeter cell. The process of calibrating the $\not{E}_T$ involves replacing the initial contribution made by globally calibrated cells with the contribution from the corresponding calibrated high-p_T objects. Additionally, cells that pass a noise cut but are not associated with any reconstructed object are also calibrated using the global calibration scheme and taken into account for the missing transverse energy calculation.

b-tagging

The identification of jets originating from b-quarks is of great importance to explore new physics. It plays a crucial role in precise measurements of the SM, including the Higgs sector, as well as in the exploration of physics beyond the standard model (BSM) enabled by the higher collision energy provided by the LHC [79].

To perform b-tagging in the ATLAS experiment, a crucial input is the reconstruction of charged particle tracks in the Inner Detector. Various algorithms are employed to distinguish between different jet flavors by utilizing these charged particle tracks and generating a set of variables. In the initial stage, calorimeter jets are matched with tracks based on their angular separation ΔR (jets, tracks). The specific association requirement for ΔR varies depending on the transverse momentum of the jet, resulting in a narrower

cone for high-p_T jets due to their higher collimation. Following this angular separation-based matching, the tracks undergo a dedicated quality selection process tailored to each b-tagging algorithm. ATLAS employs three distinct algorithms, each providing unique and complementary information [79].

The *impact parameter-based algorithms (IP2D and IP3D)* utilize the impact parameter of the tracks associated with the jet, which represents the distance between the track and the primary vertex at the point of closest approach. The sign of the impact parameter is determined as positive or negative depending on whether this point lies in front or behind the primary vertex relative to the direction of the jet.

The *secondary vertex-based algorithm (SV)* focuses on explicitly reconstructing an inclusive displaced secondary vertex within the jet. The initial stage involves reconstructing two-track vertices using the candidate tracks. However, tracks are discarded if they form a secondary vertex that can be attributed to photon conversions or hadronic interactions with the detector material. Subsequently, a single vertex is reconstructed using the tracks that pass this pre-selection step.

The *JetFitter algorithm* is a decay chain multi-vertex reconstruction algorithm that leverages the topological characteristics of weak b- and c-hadron decays occurring within the jet. It aims to reconstruct the complete decay chain from the primary vertex (PV) to the bottom-hadron and further to the charm-hadron. By analyzing the topology of these decays, the algorithm strives to accurately reconstruct the full decay chain within the jet.

The outputs of these b-tagging algorithms are subsequently integrated into a multivariate discriminant analysis. This analysis aims to achieve the highest possible separation between the various flavors of jets, resulting in an effective classification of different jet flavors [79, 74].

2.3 The DELPHES Fast Simulation

The research presented in this thesis utilized the DELPHES Fast Simulation package [11, 12]. In the field of phenomenological studies, including this thesis, it is a common practice to rely on fast software tools capable of parameterize the detector response to a certain level of realism. These tools, exemplified by DELPHES, provide a viable alternative for smaller collaborations or individual researchers who may not have access to the extensive computational resources required by the comprehensive frameworks used by large collaborations [74].

The DELPHES framework is designed to simulate the response of a multipurpose detector. It consists of various components arranged with cylindrical symmetry around the beam axis, including an inner tracker immersed in a uniform magnetic field, electromagnetic and hadronic calorimeters, and a muon detection

system. Users have the flexibility to adjust parameters such as calorimeter segmentation, the strength of the uniform magnetic field, and the active volume of the detector according to their requirements.

Each sub-detector within the DELPHES framework exhibits a specific response, which will now be described in further detail.

2.3.1 Particle Propagation

The first step carried by the simulation is to propagate the particles resulting from the physics process (after generation and hadronization) through the uniform magnetic field present in the inner tracker. There, particles will exhibit different behaviours according to their charge: neutral particles will maintain a straight trajectory from the production point to the calorimeter cell, whereas charged particles will acquire a helicoidal trajectory until they reach the calorimeter[7].

DELPHES assumes near-realistic conditions for tracking with perfect angular resolution. Users have the ability to define energy and transverse momentum resolutions based on particle type, p_T and pseudorapidity. Additionally, the probability of reconstructing charged particles as tracks can be adjusted as a user-defined parameter.

2.3.2 Calorimeter System

After the particle propagation step, the long-lived particles encounter the Calorimeter System. Similar to the arrangement in ATLAS, there is an Electromagnetic Calorimeter (ECAL), responsible for measuring the energy of photons and electrons, and a Hadronic Calorimeter (HCAL), which measures the long-lived charged and neutral hadron deposit energies. Both calorimeters are segmented in a rectangular grid in (η,ϕ), and its size can be modified by the user. DELPHES assumes an uniform segmentation in ϕ, and for computational reasons the granularity in both the ECAL and HCAL are the same.

Upon reaching the calorimeters, long-lived particles deposit a consistent fraction of their energy into the corresponding cells of the ECAL and HCAL, denoted as f_{ECAL} and f_{HCAL}, respectively. The default configuration in DELPHES assigns a value of $f_{\text{ECAL}} = 1$ for photons and electrons, and a value of $f_{\text{HCAL}} = 1$ for stable hadrons, with the exception of particles such as kaons and lambda hadrons, for which $f_{\text{ECAL}} = 0.3$ and $f_{\text{HCAL}} = 0.7$. Muons and neutrinos do not deposit any energy in the calorimeters. The default parameters in place, such as the assumption that hadrons do not interact with the ECAL and the omission of muon interaction with the calorimeters, are simplifications incorporated into the software. However, it is important to acknowledge that these parameters can be adjusted to more appropriate values if required.

[7] Particles originating from a point outside the tracker volume are discarded in this phase of the simulation.

Since the ECAL and HCAL are perfectly overlaid, a straight line originating from the interaction point traverses one ECAL cell and one HCAL cell, precisely covering the same region in (η,ϕ). These paired cells, known as calorimeter towers, are utilized alongside tracks in the object reconstruction process.

The energy detected in each calorimeter tower is determined by summing up the contributions from all particles passing through that particular tower. Each particle adds an ECAL term and an HCAL term, representing the energy deposited in the respective calorimeter, after applying smearing techniques. The energy resolution, used to account for measurement uncertainties, is independently parameterized as a function of the particle total energy and the pseudorapidity. Notably, the energy resolution varies between the ECAL and HCAL terms.

2.3.3 Particle-Flow Reconstruction

The particle-flow approach strives to achieve optimal measurements by utilizing information from all subdetectors. In real experimental scenarios, the momentum of a charged particle can be estimated by utilizing either the particle track or the calorimeter data. The choice of the preferred measurement method relies on an energy threshold. Below the threshold, the momentum resolution derived from the particle track is higher. Bellow the threshold, the calorimeter energy deposit becomes more reliable for estimating momentum. Within the context of particle-flow reconstruction, if a track is available for a particular particle, the information obtained from the track is consistently prioritized and preferred over other sources.

The particle-flow algorithm generates two sets of 4-vectors that serve as input for the subsequent reconstruction of high resolution jets and missing transverse energy. These 4-vectors comprise *particle-flow tracks* and *particle-flow towers*. For every track detected in the inner tracker, a corresponding *particle-flow track* is generated within the particle-flow algorithm. Subsequently, for each calorimeter tower, the energy contributions from particles associated with reconstructed tracks are subtracted. If the remaining energy, denoted as $E_{\text{Tower}}^{\text{eflow}}$, is found to be positive, a *particle-flow tower* is created using this energy value and positioned in the direction specified by the tower coordinates (η,ϕ).

According to this definition, *particle-flow tracks* primarily consist of charged particles, and their estimation is associated with a higher resolution. Conversely, *particle-flow towers* encompass a combination of neutral particles, charged particles without corresponding reconstructed tracks, and additional excess deposits resulting from the positive smearing effect in the calorimeters. The measurements of these components in the *particle-flow towers* generally have lower resolution compared to the *particle-flow tracks*. Despite its simplicity compared to the intricate requirements of real experiments, the algorithm described above has been proven to reproduce to a good extent the performance achieved at the LHC.

2.3.4 Object Reconstruction

In DELPHES, the object reconstruction and identification process relies on a set of approximations designed to enhance the efficiency of the procedure without compromising the overall accuracy [11, 12].

Taus

τ leptons decay prior to being detected, and only electrons and muons are directly considered as charged leptons within the DELPHES framework.

Muons

In DELPHES, the reconstruction of muons is based on a user-defined efficiency parameterization, which determines the probability of a muon originating from the interaction being successfully reconstructed. However, this probability becomes zero outside the tracker acceptance and for muon momenta below a certain threshold to reject looping particles. The final momentum of the reconstructed muon is obtained by applying a Gaussian smearing to the initial 4-momentum vector. The resolution of this smearing is parameterized by the user as a function of the transverse momentum and pseudorapidity of the muon.

Electrons

Typical identification of electrons requires combining information from the tracking system and the calorimeter. DELPHES circumvents this requirement by parameterizing the efficiency of electron reconstruction as a function of energy and pseudorapidity. The resolution of electron energy is a combination of the tracker and ECAL resolutions, with the tracker resolution dominating at low energy and the calorimeter resolution dominating at high energy. The efficiency of electron identification diminishes outside the acceptance range of the tracker and below a certain energy threshold, which is similar to muon reconstruction process.

Photons

Photons are reconstructed in DELPHES using only the Electromagnetic Calorimeter, without considering any conversions into electron-positron pairs. The ECAL resolution function is applied to obtain the energy of the reconstructed photons. In DELPHES, true photons and electrons that do not have a reconstructed track but reach the ECAL are treated as photons during the reconstruction process.

Isolation Requirement In order to reconstruct a lepton or photon, it is necessary to satisfy an isolation requirement. This requirement ensures a more accurate differentiation between particles that come

directly from the primary interaction and those that are produced in association with other particles[8].

The isolation variable, denoted as I, for a reconstructed particle P is defined as the sum of the p_T of all the particles with a transverse momentum above a threshold p_T^{min} and within a cone of $\Delta R < R$ around the particle of interest, normalized to the $p_T(P)$. In the DELPHES framework, particle P is considered isolated if the isolation variable is less than the specified threshold value I_{min}. The user has the flexibility to customize the three isolation parameters, namely p_T^{min}, R, and I_{min}, through the configuration file. The default values for these parameters are $p_T^{\text{min}} = 0.1$ GeV, $R = 0.5$, and $I_{\text{min}} = 0.1$.

Jets

In DELPHES, the process of jet reconstruction can utilize up to three different input collections: the long-lived particles resulting from parton shower and hadronization, the calorimeter towers, or the *particle-flow tracks* and *particle-flow towers*. The FASTJET package [80] is integrated into the DELPHES framework, offering a selection of popular jet clustering algorithms and the ability to adjust their parameter values. Additionally, a minimum transverse momentum threshold can be defined to determine which jets are included in the final jet collection. To prevent double-counting, DELPHES automatically excludes jets that have already been reconstructed as leptons or photons.

b and τ Jets An entirely parametric approach, relying on information from Monte-Carlo generators, is employed to identify jets originating from τ decays or the hadronization of heavy flavor quarks, such as the case of the b quark.

The procedure for identifying jets associated with b quarks and τ decays follows a specific algorithm. A jet is considered a potential b or τ jet candidate if a generated b-quark or τ particle is located within a certain angular distance, referred to as ΔR, from the axis of the jet. ΔR is calculated using the formula:

$$\Delta R = \sqrt{(\eta^{\text{jet}} - \eta^{b,\tau})^2 + (\phi^{\text{jet}} - \phi^{b,\tau})^2}. \tag{2.10}$$

The likelihood of a jet being identified as a b or τ jet is determined by user-defined parameterizations that capture the b and τ tagging efficiency. Additionally, the user can specify a mis-tagging efficiency parameterization, representing the probability of misidentifying a non-b or non-τ particle as a b or τ jet [11, 12].

[8] An isolated object has a small probability to originate from a jet.

Missing Transverse Energy and Scalar Transverse Energy

The Missing Transverse energy $\not{E}_T$ can be determined by evaluating the transverse component of the total energy deposited in the detector. The Scalar Transverse Energy H_T, is calculated by summing the individual transverse momenta of all detected particles.

$$H_T = \sum_i |\vec{p_T}(i)|. \tag{2.11}$$

Similarly to the jet reconstruction process, both the $\not{E}_T$ and H_T can be calculated using one of three different input collections: generated particles, calorimeter towers, or the *particle-flow tracks* and *particle-flow towers* [74, 11].

2.3.5 ATLAS Parameters

The particle propagation phase occurs within a cylindrical volume with a radius of 1.15 m and a half-length of 3.51 m, subjected to a magnetic field of 2 T. Tracking efficiencies for particles are evaluated in specific segments of $|\eta|$ and p_T, and are calculated independently for charged hadrons, muons, and electrons. Nevertheless, it is important to note that all tracking efficiencies are equal to zero for particles with $p_T \leq 0.1$ GeV or $|\eta| > 2.5$. Within the interval where $1.5 < |\eta| \leq 2.5$, and for $0.1 < p_T \leq 1.0$, the tracking efficiencies are relatively modest, ranging from 50% for electrons to 70% for muons. However, for electrons with higher p_T, the efficiencies consistently exceed 83%. Notably, for charged hadrons, the efficiencies are always above 85%, while for muons, they are consistently higher than 98%. The momentum resolution for charged tracks, including electrons, is assessed in segments of $|\eta|$ and p_T,. Similarly, the muon momentum resolution is also evaluated in segments of $|\eta|$ and p_T. In general, the resolution deteriorates for higher p_T and higher $|\eta|$.

Calorimeters are segmented into (η, ϕ) rectangular cells with dimensions (η, ϕ) = $(0.02, 0.02)$ within the range of $|\eta| \leq 3$. The energy deposition fractions, f_{ECAL} and f_{HCAL}, are defined differently for distinct particle types. For electrons, photons, and π^0 mesons, $f_{\text{ECAL}} = 1$ and $f_{\text{HCAL}} = 0$. For kaons and Λ particles, $f_{\text{ECAL}} = 0.3$ and $f_{\text{HCAL}} = 0.7$. Muons and neutrinos exhibit $f_{\text{ECAL}} = f_{\text{HCAL}} = 0$, while for any other long-lived particle, $f_{\text{ECAL}} = 0$ and $f_{\text{HCAL}} = 1$. The isolation criteria, as previously described in 2.3, are set at $p_T^{\text{min}} = 0.5$ GeV, $R = 0.5$, and $I_{\text{min}} = 0.1$ for the fast ATLAS simulation.

Photon, electron, and muon identification efficiencies are parameterized in segments of $|\eta|$. The identification efficiencies are 95% for the central region ($|\eta| \leq 1.5$), 85% for the intermediate region ($1.5 \leq |\eta| \leq 2.5$[9]), and 0% for $|\eta| > 2.5$[9] or $p_T \leq 10$ GeV. The anti-k_T clustering algorithm [76] is

[9] For muons, $|\eta| \leq 2.7$

employed for jet reconstruction, utilizing a ΔR parameter of 0.6. The event information stores only those jets with transverse momentum exceeding 20 GeV. The efficiency of b-tagging increases asymptotically with the transverse momentum separately for b-jets and c-jets. At the p_T limit of 20 GeV, the b-tagging efficiency for b-jets is 53%, and for c-jets, it is 7%. For all other jets, the default b-tagging efficiency is set to 0.2% to account for misidentification rates.

Part III

Analysis of Dark Matter Mediators

Chapter 3

Analysis

A comprehensive phenomenological analysis aimed at uncovering DM mediators produced in association with pairs of top quarks is presented here. Within this chapter, the essential stages of the analysis, accompanied by a description of the tools employed, are presented.

The generation of the event samples and the general-purpose detector simulation is detailed in Section 3.1. The identification of signal and background processes is addressed in Section 3.2. Subsequently, the analysis is introduced in Section 3.3. This encompasses event selection cuts, truth-matching techniques to correlate generated particles with reconstructed objects, and the kinematic fit, a key procedure of this analysis used for reconstructing undetected neutrinos and intermediate heavy particles in the events. After outlining the analysis, the angular observables being investigated are discussed in Section 3.4. The motivation behind studying these observables is then presented.

3.1 Generation of Samples

The signal and background simulated event samples were generated with `MG5_aMC@NLO` [81, 82]. The `MadSpin` [83] package was employed to manage the decay chains of heavy particles, such as top quarks and vector bosons, while preserving spin correlation effects during their decays. Subsequently, the generated events underwent parton shower and hadronization using `Pythia` [84].

All events were generated for pp collisions at a center-of-mass energy of 14 TeV. The masses of the $W^{\pm}$ bosons and the top quarks were set to $m_{W^{\pm}} = 80.4$ GeV and $m_t = 172.5$ GeV, respectively. Jets and leptons were required to have a transverse momentum above 20 GeV and 10 GeV respectively, at generation level. The maximum pseudorapidity value for jets was restricted to 5, while for leptons, it was set to 2.5.

Background Event Samples The background samples were generated at Next-to-Leading Order (NLO) in QCD, with the exception of the single top samples (including s-, t-, and Wt- channels) which were generated at Leading-Order (LO). All datasets consisted of 1×10^6 events each.

Table 5 provides a comprehensive list of all the generated background samples, accompanied by a few generation details. These details encompass the enabled decay channels in `MadSpin` and the product of the cross-section with the branching ratios.

Background Samples

Process	Decay Channels	$\sigma \times$ BR [pb]
$t\bar{t}$	$t\bar{t} \rightarrow$ Dileptonic	4.49×10^{1}
$t\bar{t}H$	$H \rightarrow$ All, $t\bar{t} \rightarrow$ Dileptonic	1.90×10^{-1}
$t\bar{t}Z$	$Z \rightarrow \nu\bar{\nu}$; $t\bar{t} \rightarrow$ All	2.73×10^{-2}
$t\bar{t}V$ ($V = W^{\pm}, Z$)	$V \rightarrow$ All, $t\bar{t} \rightarrow$ Dileptonic	7.34×10^{-2}
t (s-channel)	$t \rightarrow$ Leptonic	2.43×10^{0}
t (t-channel)	$t \rightarrow$ Leptonic	5.22×10^{1}
t (Wt-channel)	$t \rightarrow$ Leptonic	2.00×10^{1}
W	$W^{\pm} \rightarrow$ Leptonic	4.16×10^{4}
$Wb\bar{b}$	$W^{\pm} \rightarrow$ Leptonic	2.12×10^{2}
WW	$W^{\pm} \rightarrow$ All	1.12×10^{2}
WZ	$W^{\pm}, Z \rightarrow$ All	4.95×10^{1}
Z	$Z \rightarrow$ Leptonic	3.83×10^{3}
$Zb\bar{b}$	$Z \rightarrow$ Leptonic	9.77×10^{1}
ZZ	$Z \rightarrow$ All	1.51×10^{1}

Table 5: Generated Background Event Samples: Leptonic decays are limited to electrons and muons.

It should be emphasized that the single top quark cross-sections were evaluated at Next-to-Next-to-Leading-Order (NNLO) in QCD for the s–channel [85], t–channel [86, 87], and Wt–channel [88] for the leptonic channel. For the top quark pair production [89], its cross-section has also been calculated at NNLO in QCD for the dileptonic channel, and its value is presented in the same table. The cross-section values were inferred using the most recent branching ratios listed by the Particle Data Group [16].

Signal Event Samples The signal generation was performed at Next-to-Leading Order (NLO) in QCD. The $t\bar{t}Y_0$ processes were generated separately for the two scenarios involving a pure scalar ($J^{CP} = 0^{+}$)

mediator and a pure pseudo-scalar ($J^{CP} = 0^-$) mediator. Each scenario consisted of a set of particle mediator masses varying from $m_Y = 0.01$ GeV, 1 GeV, 10 GeV, 100 GeV to 125 GeV. The decays of the mediator particle were set to zero by assigning a decay width of $\Gamma_{Y_0} = 0$ GeV. Table 6 presents a comprehensive list of the generated signal samples along with relevant generation details. Similar to the background samples, each of the signal samples also consisted of 1×10^6 events each.

Pseudo-scalar Samples

m_{Y_0}	Decay Channels	$\sigma \times$ BR [pb]
0.01 GeV	$t\bar{t} \rightarrow$ Dileptonic $Y_0 \rightarrow Y_0$	3.42×10^{-2}
1 GeV		3.41×10^{-2}
10 GeV		3.26×10^{-2}
100 GeV		1.47×10^{-2}
125 GeV		1.19×10^{-2}

Scalar Samples

m_{Y_0}	Decay Channels	$\sigma \times$ BR [pb]
0.01 GeV	$t\bar{t} \rightarrow$ Dileptonic $Y_0 \rightarrow Y_0$	1.12×10^{1}
1 GeV		4.45×10^{0}
10 GeV		1.44×10^{0}
100 GeV		4.94×10^{-2}
125 GeV		2.71×10^{-2}

Table 6: Generated Signal Event Samples: The decay channel of the top quark includes only leptonic decays (electrons and muons only).

Based on the concepts introduced in section 2.3, a fast simulation of a general-purpose detector was carried out using the DELPHES framework [11, 12]. This simulation utilized default ATLAS parameters, without incorporating pile-up effects. The pertinent parameters are summarized in the subsection 2.3.5.

3.2 Signal/Background Classification

In this thesis, an analysis is carried out to search for a DM mediator produced associated with a $t\bar{t}$ pair. The $t\bar{t}$ system decays through the dileptonic channel, while the mediator itself remains stable without decaying (Figure 18 illustrates an example of a Feynman diagram for a signal event, at parton-level). The final state leptons must be either electrons or muons, since decays into τ-leptons are not considered as signal. As τ-leptons can decay into either hadrons or a lighter lepton along with two neutrinos, they are not considered as signal.

While only approximately 4% of $t\bar{t}$ decays yield dileptonic final states characterized by electrons and muons of either charge, it is noteworthy that this final state demonstrates an enhanced signal-to-background ratio. Furthermore, the smaller number of jets in the final state is advantageous for the kinematic fit, as it reduces the chances of making mistakes when assigning reconstructed jets to the decay products of t and $\bar{t}$.

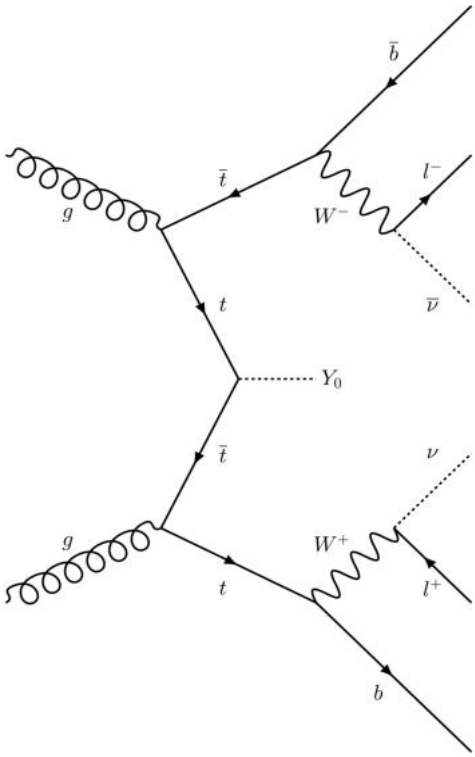

Figure 18: Feynman diagram for the $t\bar{t}Y_0$ production via gluon fusion, followed by dileptonic decay resulting in 2 charged leptons, 2 b-jets, and 2 neutrinos in the final state.

The backgrounds considered in this search can be categorized into three distinct classes, all of which represent different types of SM backgrounds exhibiting some similarity to a $t\bar{t}Y_0$ signal [90]:

- *Top backgrounds*: This class includes final states with $t\bar{t}$ and single top baseline samples (including s-, t-, and Wt- channels), each involving one or two top quarks. These backgrounds are characterized by substantial jet activity resulting from top quark decays and the presence of b-jets.

- *Reducible backgrounds*: The second category of backgrounds consists of events from WW, WZ, ZZ, W to Z, where jets originate from QCD radiation. These configurations typically exhibit lower average jet activity and often lack b-tagged jets.

- *Irreducible backgrounds*: The third class of backgrounds consists of final states denoted as $t\bar{t}H$ and $t\bar{t}V$, where $V = W, Z$. These backgrounds are considered irreducible since the resulting configurations in the final states closely resemble that of $t\bar{t}Y_0$, which involves top quark pairs decaying through the dileptonic mode, in association with at least two jets.

3.3 Event Reconstruction

The analysis of events was performed within the `MadAnalysis5` framework [91]. This package is responsible for parsing all the simulated events, sequentially processing each event and retaining all essential variables for subsequent phenomenological studies. In the ouptut files, the recorded event information is structured into three levels of information, with identical sets of variables present in each level. The output files generated by `MadAnalysis5` are in `.ROOT` format [92].

Parton-Level The first level (Generator level - `GEN`) contains information directly obtained from the generated particles, before quarks and gluons undergo hadronization or interact with the detector. This level allows for the identification of particles in the $t\bar{t}Y_0$ entire decay chain, including t and $\bar{t}$ quarks, b-quarks, and W^+ and W^- bosons. Additionally, the decay chain of each final state particle is known. At this level, the momenta of the neutrino and anti-neutrino resulting from the $t\bar{t}$ dileptonic decay can be directly obtained from the generator information.

Reconstruction Level with Truth-match In the second level (Reconstruction with Truth-match - `REC`), particles are reconstructed using information from both the detector objects (such as leptons and jets) and the generated particles. This process involves truth-matching, where each parton-level particle is associated with a detector object (lepton or jet) based on their proximity in (η, ϕ) space. Each generated lepton or quark is consistently matched with the closest reconstructed lepton and jet, respectively.

Reconstruction Level without Truth-match The third level (Reconstruction without Truth-match - `EXP`) does not use information from generated particles. It relies on correctly identifying the lepton charge, which is ensured to be accurate since `DELPHES` provides 100% efficiency for charge identification. Additionally, it must assign 2 jets, out of all reconstructed jets to the 2 b-quarks present in the final state of the $t\bar{t}$ event. Simultaneously, it must eliminate potential choices of 2 jets that are not consistent with the decay of the $t\bar{t}$ system. This level closely replicates real experimental conditions, making it particularly relevant for this DM study. The premise here is that any variable or set of variables that show discrimination between backgrounds and signals at this level could be of great interest for further use with real data [74].

3.3.1 Event Selection

At the pre-selection level, specific selection criteria (cuts) matching the topology of the $t\bar{t}Y_0$ dileptonic events are applied to all background and signal events. These cuts are designed to maximize the selection

of signal events while simultaneously rejecting a larger portion of the background events. The primary objective is to effectively distinguish the desired signal events, making it possible to apply the reconstruction routine more effectively. To meet the pre-selection criteria, all events must satisfy the requirements outlined in Table 7 below:

Pre-Selection Requirements for Events	
Number of opposite sign Leptons	≥ 2
Number of Jets	≥ 2
Transverse Momentum of Leptons (p_T^l) and Jets (p_T^j)	≥ 20 GeV
Pseudorapidity of Leptons $(\lvert\eta^l\rvert)$ and Jets $(\lvert\eta^j\rvert)$	≤ 2.5

Table 7: Summary of pre-selection cuts used: Events must have at least 2 opposite sign leptons and 2 jets with transverse momentum not below 20 GeV and $|\eta| \leq 2.5$.

For the $t\bar{t}Y_0$ pure scalar event samples, around 31% of the generated and simulated events successfully satisfy the pre-selection cuts. Similarly, the $t\bar{t}Y_0$ pure pseudo-scalar event samples exhibits a 33% selection efficiency, resembling the pure scalar case in a comparable manner. For the backgrounds, the number of events that survive the pre-selection varies according to each background.

For the final selection, further cuts are imposed as only events with exactly 2 jets are accepted. Additional cuts are also applied to the invariant mass of the 2-lepton system, denoted as m_{ll}, requiring it to be outside a 20 GeV window centered around the Z boson mass peak (≈ 91 GeV). These cuts aim to reduce the Z background. While this assumes perfect lepton identification and b-tagging, two valid conclusions emerge. First, requiring dilepton final states with more than 2 b-jets and $|m_{ll} - m_Z| > 10$ GeV mitigates most background processes at the LHC. Second, following such a selection, $t\bar{t}$ becomes the dominant background, exhibiting a much larger expected number of events compared to $t\bar{t}Y_0$.

Table 8 presents the number of events that successfully met the final selection criteria for each specific background. The final selection cuts are presented for a reference luminosity of 100 fb^{-1}.

3.3.2 Truth-Match

The reconstruction level with truth-match involves matching between detector objects, reconstructed by DELPHES, and generator-level particles as follows. Reconstructed leptons are matched to generated leptons by checking if they lie inside a cone with an angular separation of $\Delta R < 0.1$ relative to the direction of the parton-level lepton they are being matched with. The process involves running a loop over all reconstructed leptons. Within this loop, the reconstructed lepton that has the smallest ΔR value relative to the

Number of Events (100 fb^{-1})

Process	Final Selection
$t\bar{t}$	282058 ± 1830
$t\bar{t}H$	135 ± 1
$t\bar{t}Z$	685 ± 27
$t\bar{t}V$ ($V = W^{\pm}, Z$)	341 ± 2
t (Wt-channel)	5377 ± 104

Table 8: The number of events that survive the final selection cuts for a reference integrated luminosity of 100 fb^{-1} (only statistical uncertainties are shown). Background processes not featured in the table had no events that met the final selection requirements.

parton-level lepton is identified as the matched parton-level lepton. It is important to note that the charge information of the reconstructed leptons is not utilized during this matching procedure.

A similar procedure is applied to the jets. A matched reconstructed jet is found when it is within a cone of $\Delta R < 0.5$ with respect to the corresponding parton-level quark. The algorithm loops through all available jets in the event, choosing the one with smallest ΔR value.

Figure 19 shows the p_T resolution for positive leptons (left) and b-quarks (right). Results are presented for signal events with a mediator mass of 10 GeV. The resolution $^{\Delta p_T}/_{p_T^{\text{Parton}}}$ is characterized as the difference between the reconstructed p_T and the parton-level p_T, normalized to the parton-level value. The p_T resolution for b-quarks is poorer when compared with that of leptons, and this discrepancy is anticipated to affect the reconstruction of intermediate particles.

3.3.3 Kinematic Fit from Truth-Match

The reconstruction of top and anti-top quarks is performed using the kinematic information of their respective decay products. Nevertheless, the momenta of neutrinos and anti-neutrinos remain unobserved in general-purpose experiments, as neutrinos evade direct detection. In the kinematic reconstruction, the missing transverse energy ($\not{E}_T$) is assumed to be the transverse projection of the combined momenta of the neutrino (p_{T_ν}) and anti-neutrino ($p_{T_{\bar{\nu}}}$). This implies:

$$p_\nu^x + p_{\bar{\nu}}^x = \not{E}_T^x \quad \text{and} \quad p_\nu^y + p_{\bar{\nu}}^y = \not{E}_T^y. \tag{3.1}$$

To fully determine all components of the momenta for both the neutrino and anti-neutrino (comprising six quantities in total), at least four additional constrains are necessary. The conservation of momentum in

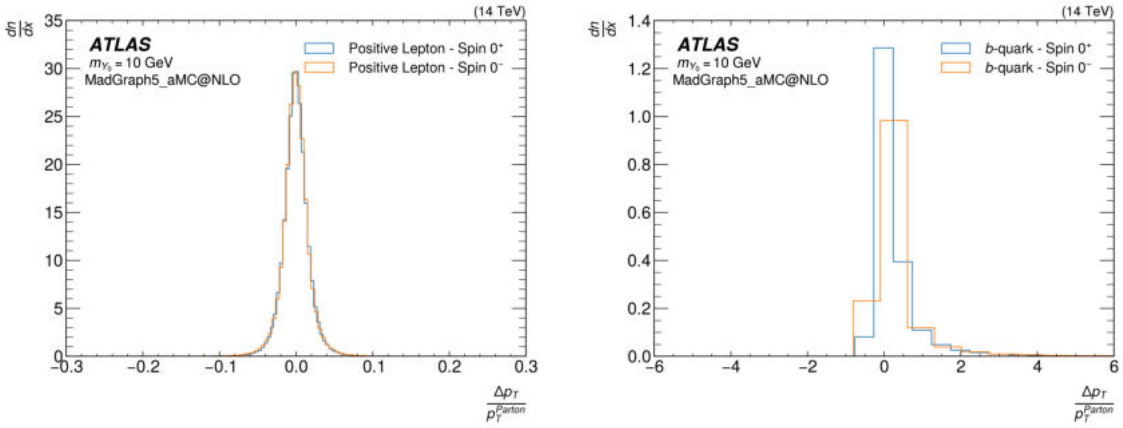

Figure 19: The p_T resolution of the reconstructed positive leptons (left) and b-quarks (right). The bin content $^{dn}/_{dx}$ represents the fraction of the total number of events per bin. The b-quark p_T resolution is noticeably poorer.

a particle decay establishes that the momentum 4-vector P of the decaying particle is equal to the sum of the momenta of the decay products. In this particular case, $P_t = P_W + P_b$, and similarly, $P_W = P_\nu + P_l$.

The four additional constrains are then,

$$\begin{aligned} (P_{W^+} + P_b)^2 &= m_t^2 \\ (P_{W^-} + P_{\bar{b}})^2 &= m_{\bar{t}}^2 \\ (P_\nu + P_{l^+})^2 &= m_{W^+}^2 \\ (P_{\bar{\nu}} + P_{l^-})^2 &= m_{W^-}^2 \end{aligned} \tag{3.2}$$

The quadratic nature of these equations suggests that multiple solutions may exist for the momenta of the neutrino and anti-neutrino, satisfying the mass constraints and accounting for the observed missing transverse energy [74].

Likelihood Method In the process of selecting a particular solution from the available options, a likelihood-based approach is used. $\mathcal{P}_U(U')$ is defined as the probability density function (PDF) of the variable U, computed at the value $U = U'$. PDFs can be extended to multiple dimensions. For instance, in two dimensions, $\mathcal{P}_{U,V}(U', V')$ represents the probability density function of two variables, U and V, evaluated at the point (U', V').

The utilization of PDFs of dimension two or higher becomes particularly significant when handling correlated variables. In the majority of scenarios presented, U' and V' do not assume specific values, allowing the shorthand notation $\mathcal{P}_{U,V}(U', V') = \mathcal{P}(U', V')$ to be employed without any ambiguity [74].

For the kinematic fit, the selected solution is the one that maximizes the following likelihood:

$$\frac{1}{p_{T_\nu} p_{T_{\bar{\nu}}}} \mathcal{P}(p_{T_\nu}) \mathcal{P}(p_{T_{\bar{\nu}}}) \mathcal{P}(p_{T_t}) \mathcal{P}(p_{T_{\bar{t}}}) \mathcal{P}(p_{T_{t\bar{t}}}) \mathcal{P}(m_t, m_{\bar{t}}). \tag{3.3}$$

The probability density functions used were derived from generator-level $t\bar{t}Y_0$ events with a mediator mass of 0.01 GeV, in a pure scalar scenario.

Here, each PDF is incorporated sequentially to ensure that the transverse momentum and mass distributions of reconstructed events mirror those observed at the parton-level. However using only the PDFs introduces a tendency towards solutions where neutrinos have higher energies than initially generated. This bias is enhanced in NLO signal events due to gluon emission by any colored particle. Should the gluons bear sufficient energy, they have the potential to originate additional jets. Since the kinematic fit follows a leading-order approach, the decrease of energy of any detected colored object, results in an increase in the number of solutions where neutrinos are more energetic. For this reason, the initial factor of $1/p_{T_\nu} p_{T_{\bar{\nu}}}$ is incorporated to counterbalance this influence, by prioritizing solutions featuring lower p_T neutrinos [74].

In the kinematic fit, this implementation is carried out as follows. The input masses of t and $\bar{t}$ are randomly sampled, up to 500 times, using the 2D probability density function, $\mathcal{P}(m_t, m_{\bar{t}})$, derived from generator-level events. Subsequently, the masses of W^+ and W^- are produced in accordance with the probability density functions $\mathcal{P}(m_{W^+}, m_t)$ and $\mathcal{P}(m_{W^-}, m_{\bar{t}})$, respectively. Following the initial sampling of the four masses, a fine random sampling is applied to the values obtained for the masses whenever a solution is found within the bins of the $\mathcal{P}(m_{W^+}, m_t)$ and $\mathcal{P}(m_{W^-}, m_{\bar{t}})$ probability density functions (each with a granularity of 1 GeV $\times$ 1 GeV)[1]. The objective here is to identify potential solutions (up to 2 times) with mass values that deviate from the central mass value for a given solution by no more than the mass plot resolution.

For a scalar mediator signal, the kinematic fit efficiency to reconstruct at least one solution is 75% for $t\bar{t}Y_0$ events with a mediator mass of 0.01 GeV. For a mediator mass of 125 GeV, the efficiency is 66%. The pseudo-scalar signal follows a similar pattern. For a mediator mass of 0.01 GeV, the efficiency is 73%. It decreases to 69% for a mediator mass of 125 GeV.

Figures 20 and 21 show the correlations between kinematic variables, namely the momentum (p_T) on the left and the pseudorapidity (η) on the right, for reconstructed particles with truth-level and their corresponding parton-level counterparts. It is important to acknowledge that while this type of kinematic fitting procedure aims to approximate parton-level distributions, it may not perfectly replicate the exact parton-level kinematics for each individual event. This limitation is attributed to factors including detector

[1] The introduction of fine variations enhances the efficiency of the kinematic fit and contributes to improving the quality of the identified solutions.

resolution, inefficiencies, and constraints imposed by kinematic fit [74].

Figure 20 displays the distributions related to the pure scalar mediator with a mass of 0.01 GeV, whereas Figure 21 illustrates the distributions for the pure pseudo-scalar mediator, also for the same mediator mass of 0.01 GeV. For different mediator masses and scenarios, please consult Appendix A.1[2].

[2] Similar distributions are obtained for the particles counterparts ($\bar{t}$,$\bar{\nu}$,W^-); however, these are omitted from display

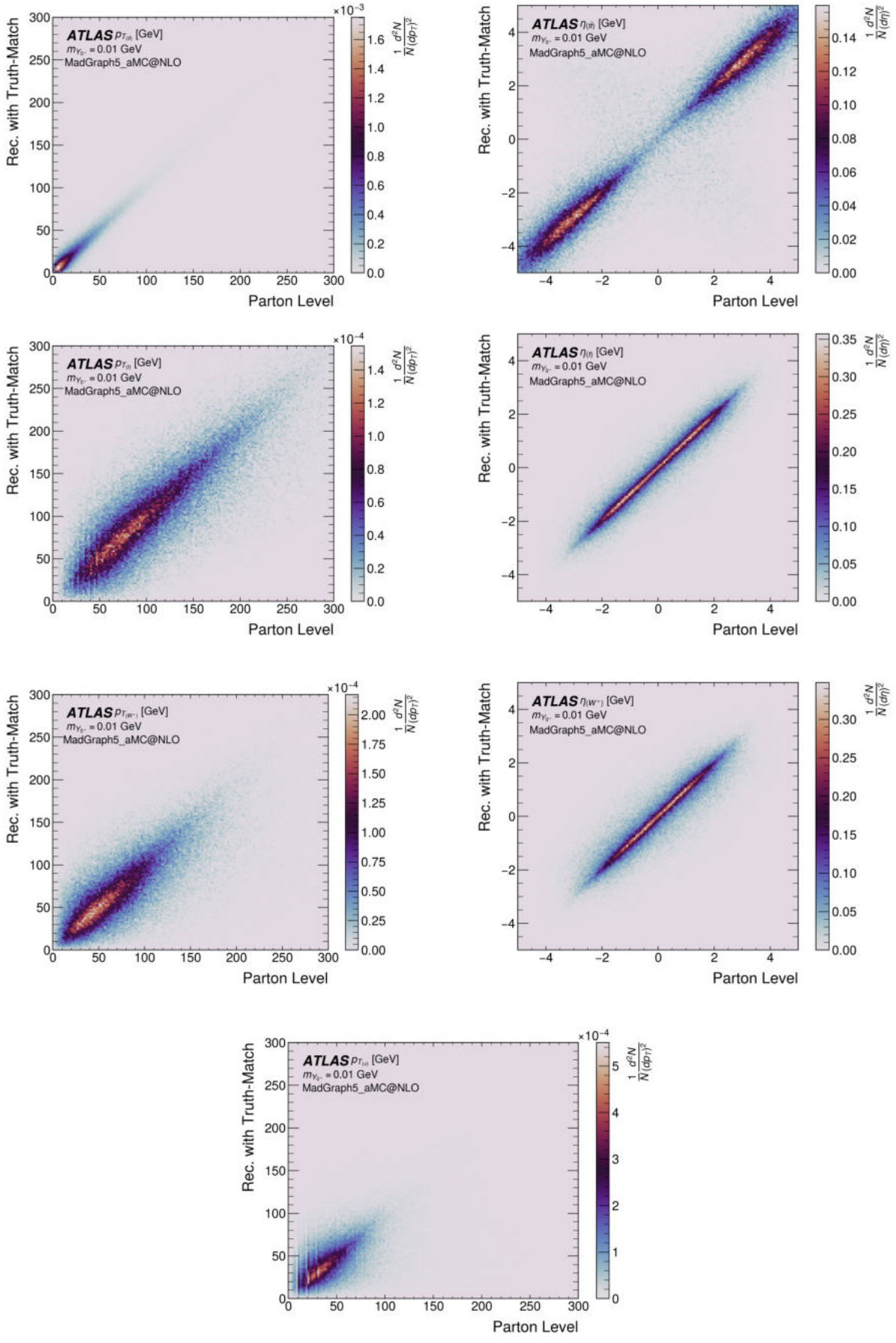

Figure 20: Two-dimensional kinematic distributions for $t\bar{t}Y_0$ events with $m_{Y_0} = 0.01$ GeV ($J^{CP} = 0^+$). *1st line:* p_T (left) and η (right) of $t\bar{t}$, *2nd line:* p_T (left) and η (right) of t, *3rd line:* p_T (left) and η (right) of W^+, and the 4th line: p_T of ν.

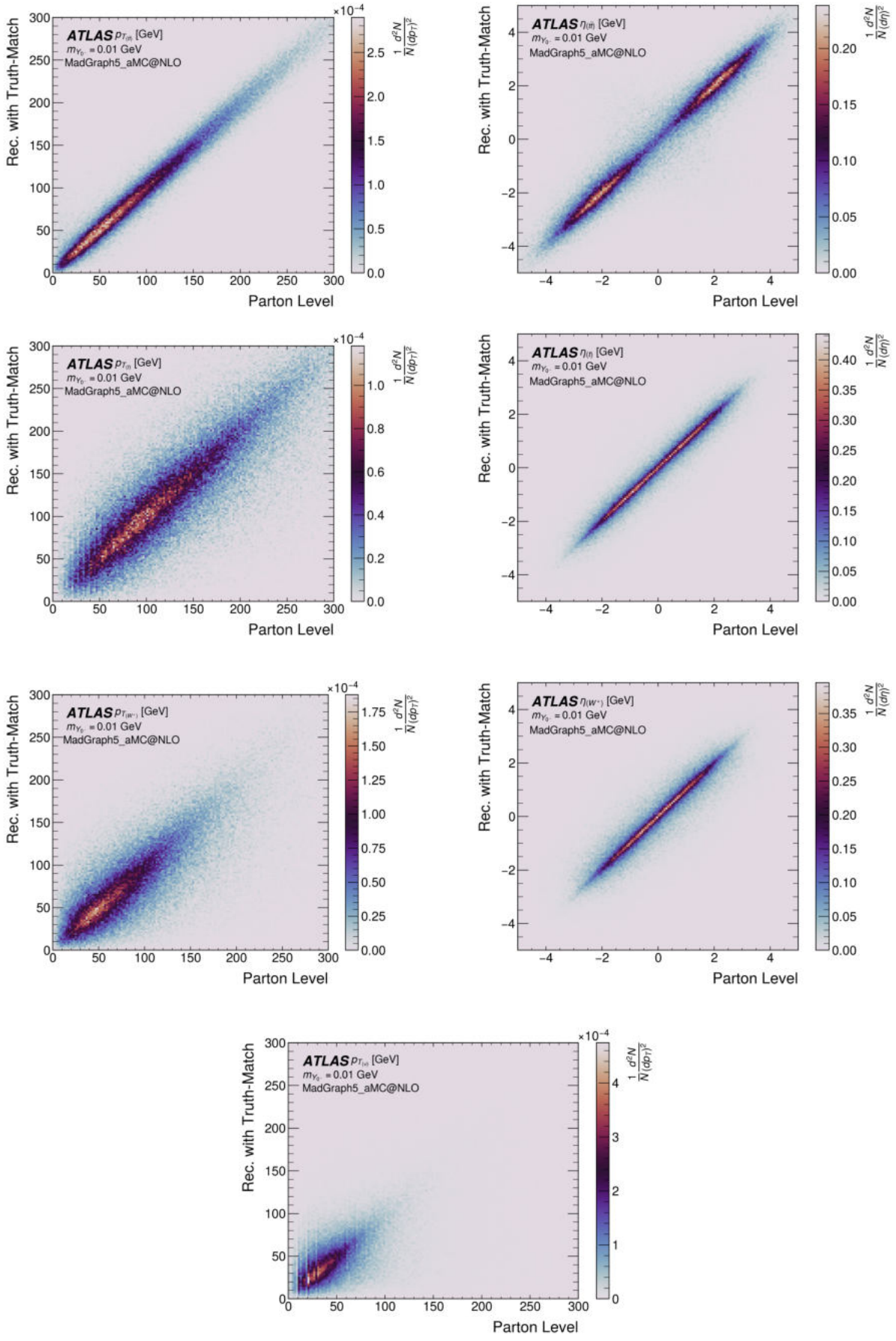

Figure 21: Two-dimensional kinematic distributions for $t\bar{t}Y_0$ events with $m_{Y_0} = 0.01$ GeV ($J^{CP} = 0^-$). *1st line:* p_T (left) and η (right) of $t\bar{t}$, *2nd line:* p_T (left) and η (right) of t, *3rd line:* p_T (left) and η (right) of W^+, and the 4th line: p_T of ν.

Clear correlations are observed between the reconstructed and the parton-level kinematics, demonstrating the efficacy of the fit. The enhanced correlation in η is, in part, due to the requirement that truth-matched objects fall within a $\Delta R < 0.5$ cone around the parton-level particle.

The effect of the reconstructed neutrinos to compensate for energy losses and resolution effects within the event, results in appreciable differences from the parton-level neutrinos. Yet, upon combining the reconstructed neutrino with the reconstructed lepton, the resulting W boson closely resembles its parton-level counterpart. This resemblance is even more pronounced in the top quark, formed by combining the W boson with the jet matched to its corresponding b-quark. Ultimately, the reconstructed $t\bar{t}$ system exhibits remarkable similarity to its parton-level counterpart.

In certain cases (e.g. the $t\bar{t}$ system for the pseudo-scalar mediator of mass 100 GeV in Appendix A.1), the reconstructed p_T tends to be lower when compared to parton-level. The differences in p_T can be attributed to energy losses from jets associated with the b-quarks from the top decay process. These energy losses can occur through out-of-cone emissions, where, for instance, an energetic gluon radiated off by the b-quark falls outside the cone defined by the jet algorithm, or via particle decays within the jet, leading to neutrinos or muons, which prevent full energy recovery from the calorimeter deposits [74].

3.3.4 Kinematic Fit without Truth-Match

The reconstruction without truth-match closely replicates real experimental conditions, where access to generation information is not possible. While the reconstruction process with truth-match uses parton-level information, the scenario without truth-match requires determining whether each reconstructed jet originates from the b or $\bar{b}$ quarks produced in the decay of t and $\bar{t}$, respectively. If the number of jets in $t\bar{t}Y_0$ events is large, the possibility for erroneous assignments increases significantly. To enhance the precision of jet and lepton assignment, the application of an association criteria becomes necessary, if no parton-level information is used.

Jet and Lepton Pairing using TMVA

In order to assign not only the jets, but also the leptons to their parent top quarks, this analysis employs a multivariate statistical approach using `TMVA` (Toolkit for Multivariate Data Analysis) toolkit [93].

To achieve this, different distributions are used to distinguish between correct and incorrect pairings of leptons and jets assigned in the same top quark decay. These include the mass difference $\Delta m = m_{(l^+,b)} - m_{(l^-,\bar{b})}$, as well as ΔR, $\Delta\phi$, and $\Delta\theta$ for the pairs of jets and leptons (l^+, b_t) and $(l^-, \bar{b}_{\bar{t}})$, where b_t and $\bar{b}_{\bar{t}}$ refer to the bottom quark from the top decay and the anti-bottom quark

from the anti-top decay, respectively[3]. Figure 22 shows these variables for the pure scalar, and pure pseudo-scalar cases, respectively. The displayed pairing is (l^+, b_t), but analogous distributions are obtained for the $(l^-, \bar{b}_{\bar{t}})$ pairing. Clear differences between incorrect and correct pairings are observed in all distributions.

`TMVA` is employed to train various multivariate statistical methods. For both training and testing, distributions involving both correct (signal) and incorrect (background) combinations are used. These different distributions are then combined to create a single discriminant classifier for each method. The corresponding *Receiver Operating Characteristic* (ROC) curves obtained from the different methods used are presented in Figure 23.

From the ROC curves across all mediator mass values explored, for scalar and pseudo-scalar signals, the best methods found were the *Boosted Decision Tree* (BDT) and the *Gradient Boosted Decision Tree* (BDTG) (Figure 24). The latter method is employed for lepton-jet pairing, and the selected combination is the one that yields the highest BDTG discriminant value.

It should be remarked that the scalar mediator presents greater challenges, characterized by a slightly worse ROC curve. Consequently, the pairing process derived exclusively from the scalar mediator signal is used in this analysis, as this case embodied a more conservative approach.

Following the pairing of jets and leptons using `TMVA`, the kinematic fit is conducted using the equations presented in 3.1 and 3.2, according to the previously outlined approach of subsection 3.3.3.

In the pure scalar mediator case, assuming a mass of 0.01 GeV, the kinematic fit succeeds in approximately 62% of the selected $t\bar{t}Y_0$ events. This efficiency decreases to around 47% when the mediator mass is increased to 125 GeV. Similarly, in the pseudo-scalar case, with a mediator mass of 0.01 GeV, the reconstruction efficiency is roughly 55%, but decreases to about 47% for a mass of 125 GeV.

Figures 25 and 26 illustrate the correlations between kinematic variables of the reconstructed particles without truth-match and the corresponding variables at the parton-level. Specifically, p_T is displayed on the left, while η is shown on the right. These correlations correspond to the identical scenarios presented in the preceding figures, which were reconstructed with truth-match. Additional plots related to varying masses and scenarios are found in Appendix A.2[4].

[3] The variables ΔR, $\Delta\phi$, and $\Delta\theta$ are also evaluated for the incorrect combinations (l^-, b_t) and $(l^+, \bar{b}_{\bar{t}})$.

[4] Equivalent distributions are obtained for the particle counterparts ($\bar{t}$, $\bar{\nu}$, W^-); however, these are not displayed here.

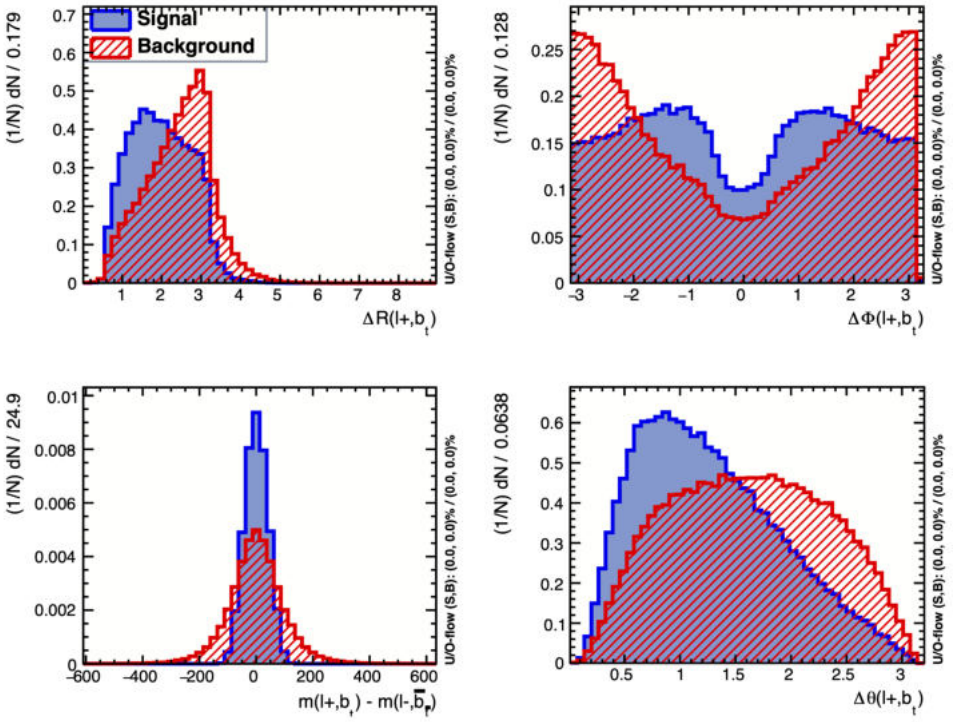

(a) $m_{Y_0} = 0.01$ GeV ($J^{CP} = 0^+$)

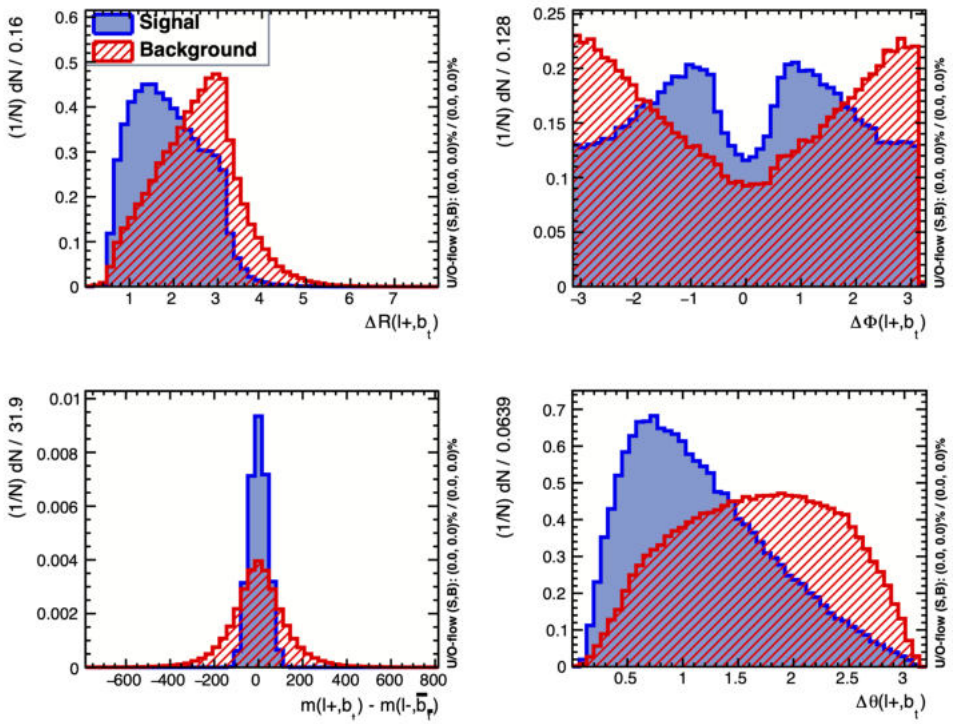

(b) $m_{Y_0} = 0.01$ GeV ($J^{CP} = 0^-$)

Figure 22: Distributions of the TMVA input variables are shown for $t\bar{t}Y_0$ events. The good (bad) pairings of jets and leptons originating from the same top quarks are represented in blue (red), and labeled as signal (background), respectively. Both scalar ($J^{CP} = 0^+$) and pseudo-scalar ($J^{CP} = 0^-$) distributions are shown.

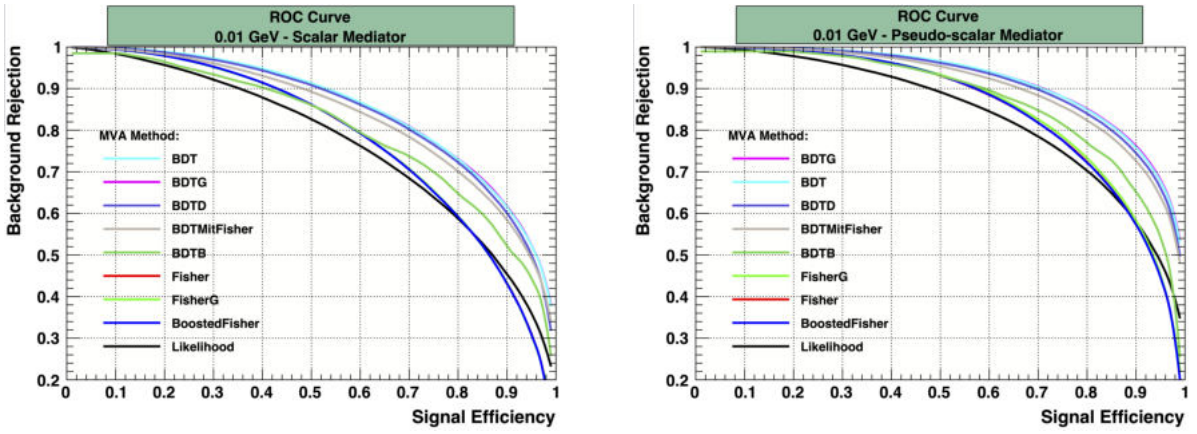

Figure 23: The ROC curve is shown for several TMVA classifiers, for both the scalar (left) and pseudo-scalar (right) Y_0 cases. The most effective methods for accurate jet assignment in $t\bar{t}Y_0$ events are consistently BDT or BDTG across all studied mediator masses.

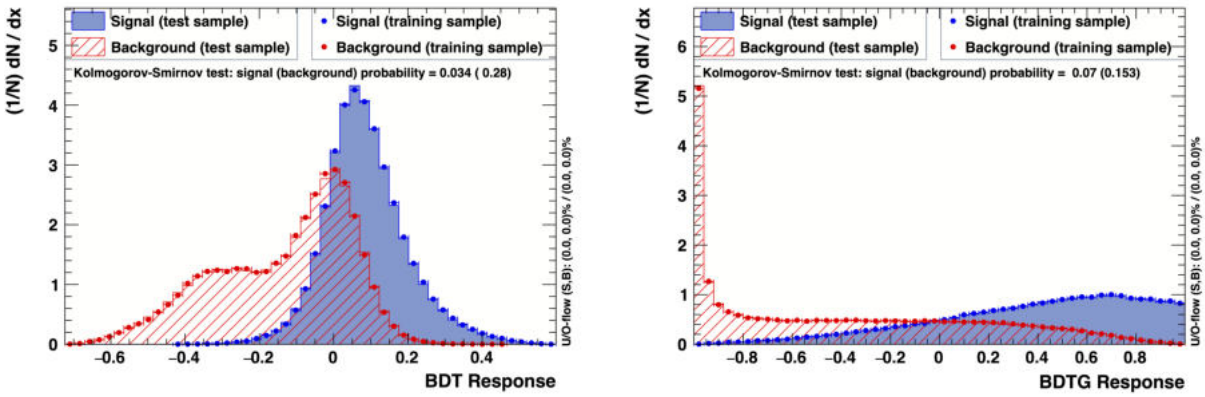

(a) $m_{Y_0} = 0.01$ GeV ($J^{CP} = 0^+$)

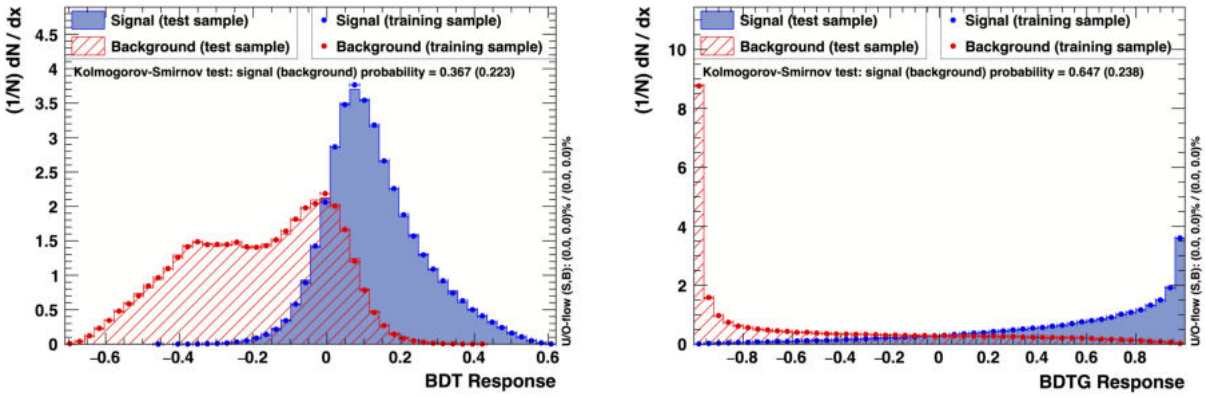

(b) $m_{Y_0} = 0.01$ GeV ($J^{CP} = 0^-$)

Figure 24: BDT (left) and BDTG (right) discriminant distributions for signal and background in training and test samples, for both the scalar (top) and pseudo-scalar (bottom) Y_0 cases.

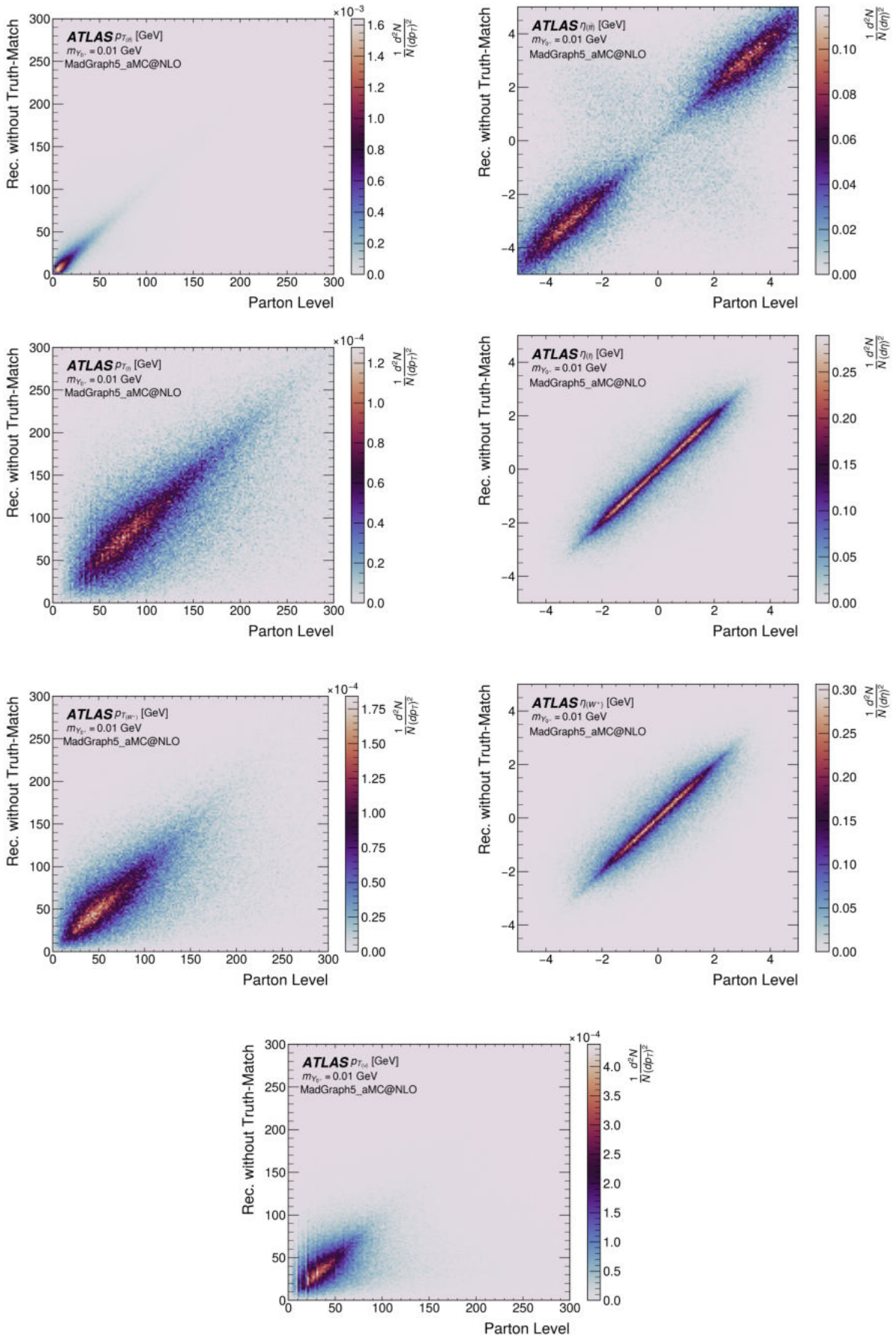

Figure 25: Two-dimensional kinematic distributions for $t\bar{t}Y_0$ events with $m_{Y_0} = 0.01$ GeV ($J^{CP} = 0^+$). *1st line:* p_T (left) and η (right) of $t\bar{t}$, *2nd line:* p_T (left) and η (right) of t, *3rd line:* p_T (left) and η (right) of W^+, and the 4th line: p_T of ν.

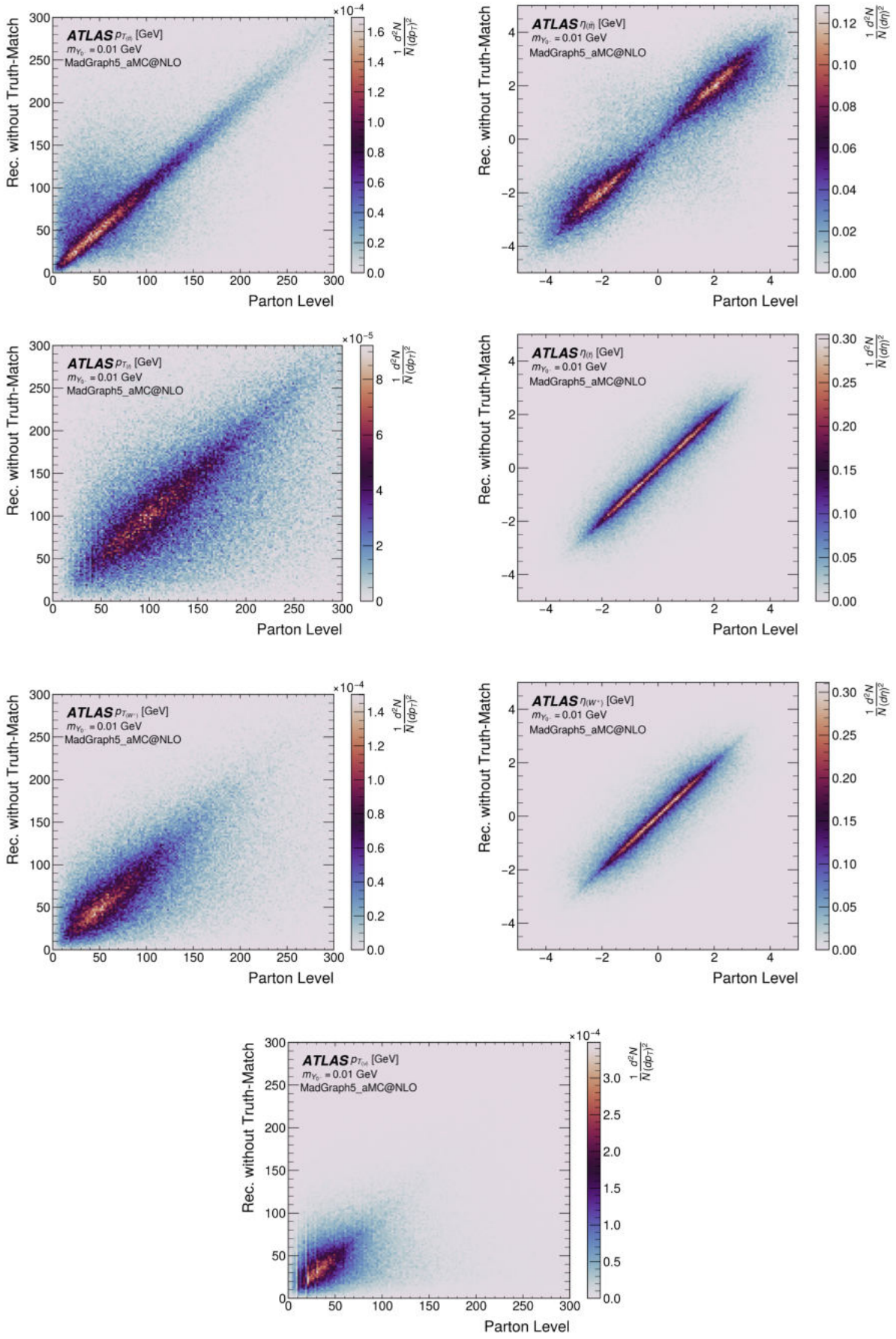

Figure 26: Two-dimensional kinematic distributions for $t\bar{t}Y_0$ events with $m_{Y_0} = 0.01$ GeV ($J^{CP} = 0^-$). *1st line:* p_T (left) and η (right) of $t\bar{t}$, *2nd line:* p_T (left) and η (right) of t, *3rd line:* p_T (left) and η (right) of W^+, and the 4th line: p_T of ν.

Similar to the truth-match scenario, the η variable has better resolution when compared to the p_T variable. Here, however, the presence of combinatorial background resulting from incorrect combinations of jets and leptons has an impact on the kinematic reconstruction.

Evidently, the strong correlation between parton-level, and the reconstructed kinematic properties of individual particles and particle systems remains evident. This suggests that even considering the impact of experimental factors, reconstructing the $t\bar{t}$ system is possible without directly taking into account the DM mediator. This insight is important as it allows for studying angular distributions of $t\bar{t}$ systems, even when they are accompanied by undetected particles.

3.4 Angular Observables

The study of angular distributions of SM particles offers a pathway to delve into the hidden *Dark Sector* via possible modifications caused by the presence of DM mediators. While certain angular observables have proven valuable in probing the (Charge-Parity) CP-nature of the Yukawa top quark coupling in $t\bar{t}H$ events [94, 95, 96], their adaptation to probe the coupling between top quarks and the DM mediator in this particular context remains largely unexplored [5].

This thesis examines the b_2 angular observable, originally proposed by Gunion et al. [9] to study the CP nature of the new DM mediator. More importantly, two new angular observables derived from the b_2 observable are introduced and additionally explored, with a focus on assessing their potential as discriminating variables. The purpose for the introduction of these observables is to study their sensitivity to the DM mediator CP-nature within the framework of $t\bar{t}Y_0$ production [6]. By probing the CP nature of the mediator-top quark coupling, confidence level (CL) limits for Yukawa couplings can be set, as a function of the mediator mass. Below, the definitions of the tested observables are provided, along with the underlying reasoning for their formulation.

3.4.1 The b_2 Observable: New Derived Observables

The b_2 angular observable is defined as:

$$b_2 = \frac{(\vec{p_t} \times \hat{n}) \cdot (\vec{p_{\bar{t}}} \times \hat{n})}{|\vec{p_t}||\vec{p_{\bar{t}}}|}. \tag{3.4}$$

where $\hat{n}$ represents a unit vector along the beam line direction, defining the z axis. $\vec{p_t}$ and $\vec{p_{\bar{t}}}$ denote the 3-momentum vectors of the top and anti-top quarks, respectively. The b_2 variable depends on the t and $\bar{t}$

[5] Given the considerable likeness between the final states of $t\bar{t}H$ and the associated production of DM mediators $t\bar{t}Y_0$.

[6] Any mixed state can be reconstructed by overlapping pure scalar and pseudo-scalar components, and thus a CP-violating state.

polar angles, namely θ_t and $\theta_{\bar{t}}$, i.e., the angles defined with respect to the z-direction. Therefore, is also possible to represent the b_2 observable as follows:

$$b_2 = \sin(\theta_t) \times \sin(\theta_{\bar{t}}) \tag{3.5}$$

In this thesis, in contrast to previous publications [74, 96], which just explore the original b_2 variable in the $t\bar{t}H$ channel, a new alternative approach involving projections with respect to different axis is proposed. This thesis specifically explores (x, y, z) projections of the b_2 variable onto the $(0, 1, 0)$ and $(0, 1/\sqrt{2}, 1/\sqrt{2})$ axes. The new $\tilde{b_2}$ angular observables are defined as:

$$\tilde{b_2}^{\,k_d} = \frac{(\vec{p_t} \times \hat{k_d}) \cdot (\vec{p_{\bar{t}}} \times \hat{k_d})}{|\vec{p_t}||\vec{p_{\bar{t}}}|}. \tag{3.6}$$

where $\hat{k_d}$ is either $(0, 1, 0)$ or $(0, 1/\sqrt{2}, 1/\sqrt{2})$. It is worth noting that the kinematic reconstruction of the $t\bar{t}$ system described above is an absolute prerequisite for assessing these variables. The discussion of the sensitivity of the new variables for DM studies is presented in the next chapter.

Chapter 4

Results

In this Chapter, the results of the DM studies are presented and discussed using angular observables. This chapter is divided into two sections, corresponding to the twofold motivation given for the use of new angular observables: discrimination between DM mediator CP-scenarios (scalar and pseudo-scalar), and establishing confidence level (CL) limits on the Yukawa couplings between the mediator and the top quarks. The first section addresses the discrimination between scalar and pseudo-scalar scenarios of the DM Mediator. The distributions of the angular observables are shown and interpreted. Subsequently, a comparison is made between all considered variables. Brief discussions are also included regarding the impact of detector simulation and the kinematic fit. The second section delves into the evaluation of Confidence Level (CL) limits for the Yukawa couplings. The results are presented for different signal hypotheses, for two distinct integrated luminosities.

4.1 The CP Nature of the Dark Matter Mediator

All the observables outlined in Section 3.4 have been examined. In Figure 27 the parton-level distributions for b_2, $\tilde{b}_2^{(0,1,0)}$, and $\tilde{b}_2^{(0,1/\sqrt{2},1/\sqrt{2})}$ are shown for a DM mediator mass of 0.01 GeV. Figure 28 shows the analogous distributions, but considering reconstruction without truth-match.

The new angular show clear differences between scalar and pseudo-scalar signals, even after event selection and kinematic reconstruction without truth match. This contrasts to the standard b_2 observable, which shows a rather poor discrimination between CP-even and CP-odd signals.

In Figure 29, the expected number of events after event selection and kinematic reconstruction is presented for a reference luminosity of 100 fb^{-1}. All SM backgrounds outlined in section 3.1 are accounted for. The distributions are compared to scalar and pseudo-scalar signals, both with a mass of 0.01 GeV, for the same observables under study. The scalar signal is scaled by a factor of 2, and the pseudo-scalar signal is scaled by 500 for representation purposes only.

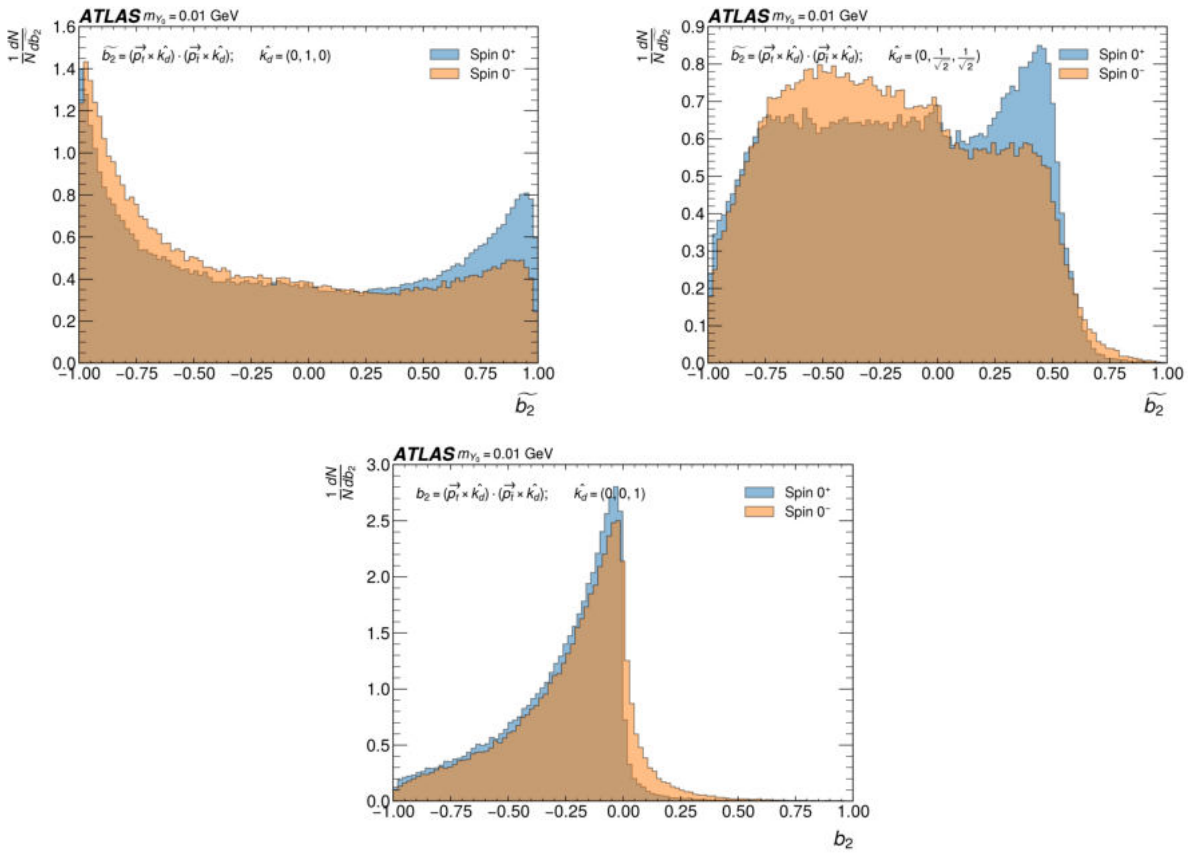

Figure 27: *Parton-Level* distributions of $\tilde{b_2}$ projected onto the $(0, 1, 0)$ axis (top left) and onto the $(0, 1/\sqrt{2}, 1/\sqrt{2})$ axis (top right), presented as discriminants. The standard b_2 distribution is provided for comparison (bottom).

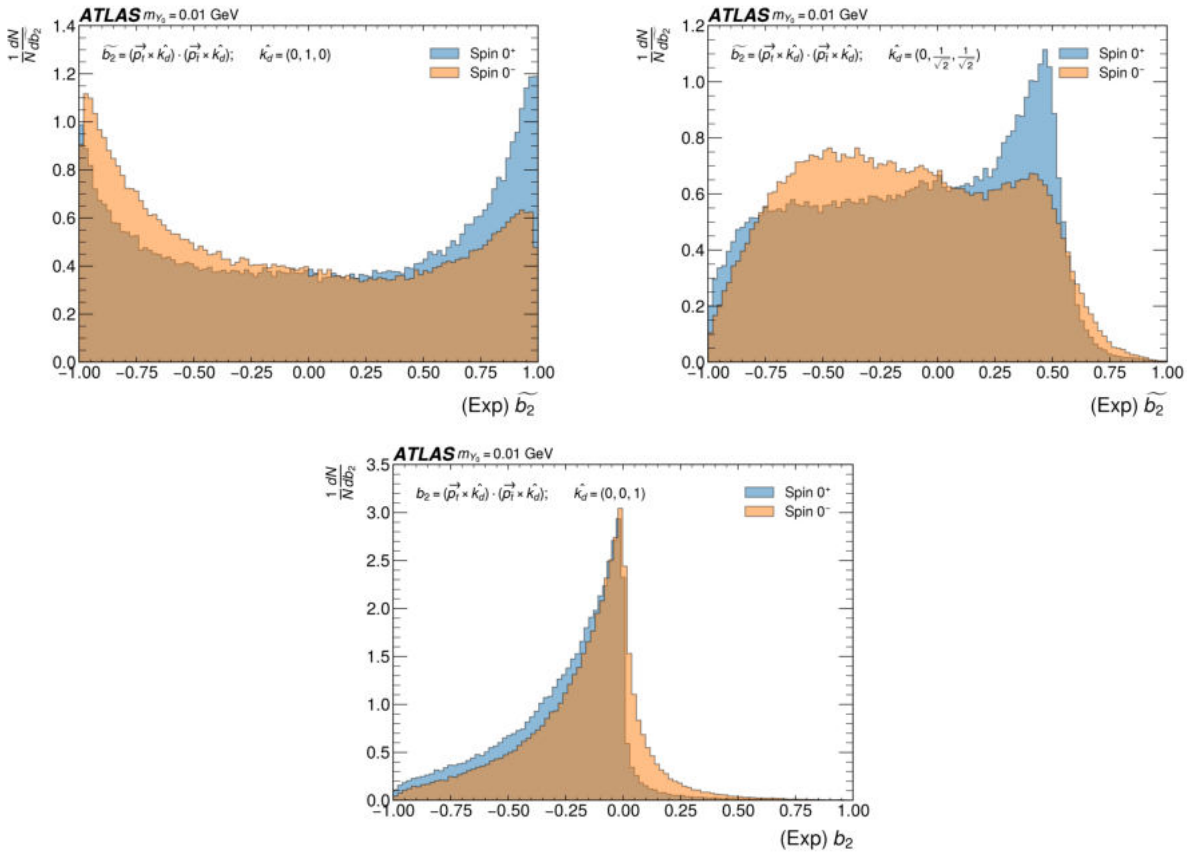

Figure 28: *Reconstruction Level without Truth-Match* distributions of $\tilde{b_2}$ projected onto the $(0, 1, 0)$ axis (top left) and onto the $(0, 1/\sqrt{2}, 1/\sqrt{2})$ axis (top right), presented as discriminants. The standard b_2 distribution is provided for comparison (bottom).

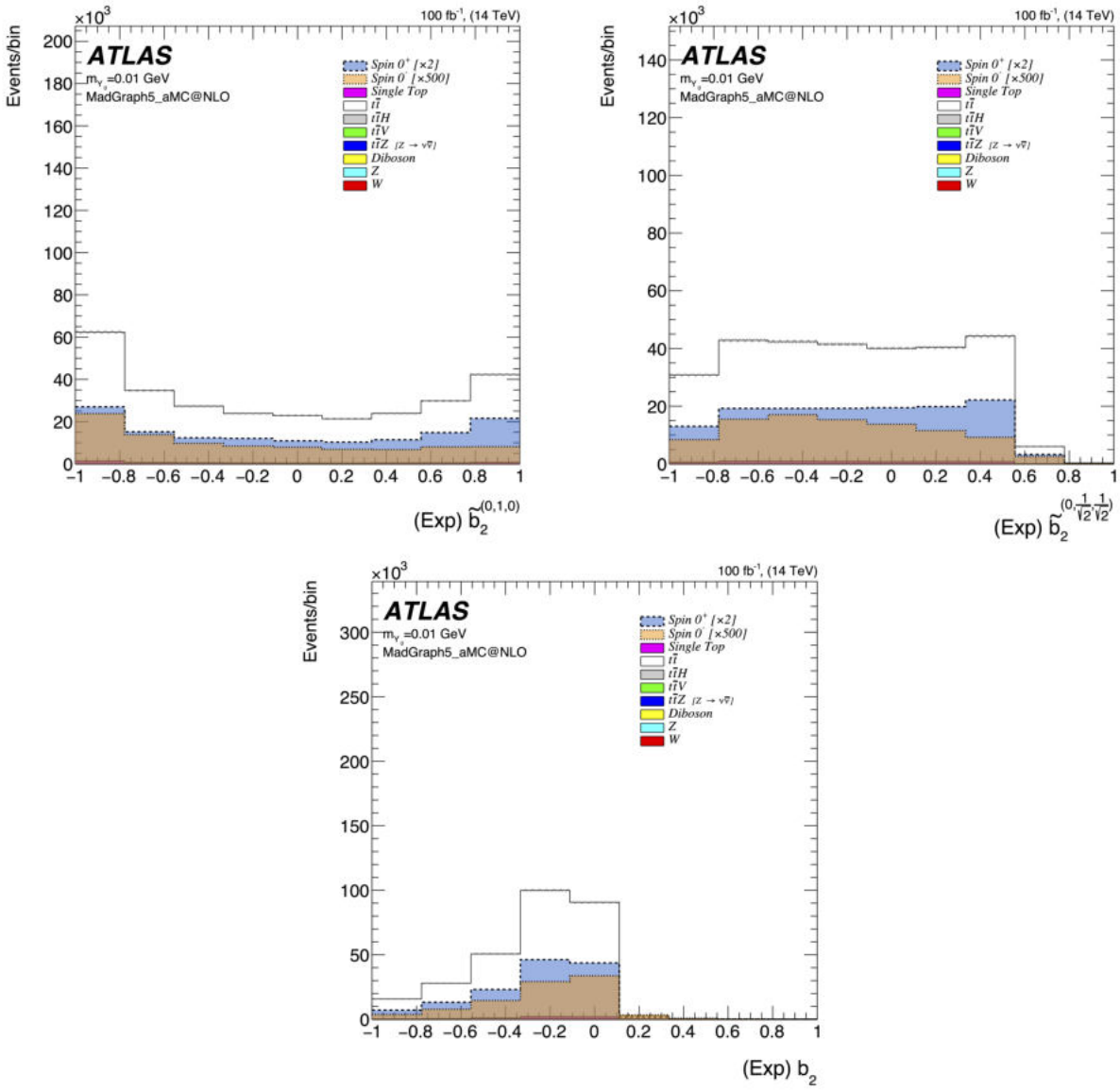

Figure 29: The expected number of events for the distributions of $\tilde{b}_2^{(0,1,0)}$ (top left), $\tilde{b}_2^{(0,1/\sqrt{2},1/\sqrt{2})}$ (top right), and b_2 (bottom) after event selection and kinematic reconstruction, for a luminosity of 100 fb^{-1}.

As anticipated, the primary source of SM background stems from the $t\bar{t}$ process, mainly because of its resemblance to the $t\bar{t}Y_0$ final state topology. All remaining backgrounds[1] have residual contributions when compared to the dominant $t\bar{t}$ background.

In all plots, changes in shapes of the background distributions become apparent when compared to signals. Of particular interest is the behavior of the scalar and pseudo-scalar signals in the two newly introduced $\tilde{b_2}$ variables. In the case of $\tilde{b}_2^{(0,1,0)}$, both signals appear to be evenly distributed among negative values. However, differences exist when considering positive values. The scalar signal exhibits a more symmetrical distribution, with events being almost evenly distributed among positive and negative values, while the pseudo-scalar distribution exhibits a noticeable decrease in events for positive values. The pronounced difference between scalar and pseudo-scalar signals is even more visible in the $\tilde{b}_2^{(0,1/\sqrt{2},1/\sqrt{2})}$ distribution. The scalar signal exhibits a nearly equal distribution within the range of -0.8 to 0.6, with a noticeable decrease towards the tails of the distribution. This behavior is not replicated in the pseudo-scalar scenario. In this case, events cluster and primarily occupy the range between -0.6 and -0.4, followed by a gradual decline.

The b_2 observable also exhibits differences in the shapes of the distributions, although these differences are not as pronounced as those observed in the other two cases.

4.2 Exclusion Confidence Level Limits

Exclusion confidence levels (CLs) on the scalar and pseudo-scalar nature of the top quark couplings to the DM mediator are established in two different scenarios. For each scenario, these CLs are calculated for two luminosities: one corresponding roughly to the expected integrated luminosity of the *LHC Run 3* and the other to the High-Luminosity phase of the LHC (HL-LHC). All generated mass values for the DM mediator are taken into consideration.

The distributions of b_2, $\tilde{b}_2^{(0,1,0)}$, and $\tilde{b}_2^{(0,1/\sqrt{2},1/\sqrt{2})}$ are utilized for establishing the CLs. This analysis considers the contribution from all SM backgrounds, which are normalized to the LHC luminosities of *LHC Run 3* and HL-LHC. In each analyzed scenario, one hundred thousand pseudo experiments are generated by applying bin-by-bin Poisson fluctuations around a mean value, which is set to the number of events in each individual bin of the angular distributions [96]. The assessment of whether a null hypothesis (H_0) or an alternative hypothesis (H_1) can effectively explain the pseudo experiment entails the evaluation of the probabilities associated with each hypothesis. The likelihood ratio of the probabilities linked to H_1 and H_0

[1] Z encompasses Z and $Zb\bar{b}$, while W comprises W and $Wb\bar{b}$. Diboson events consist of WW, ZZ, and WZ

is utilized as the test statistic to compute the confidence level at which hypothesis H_1 can be excluded under the assumption that H_0 is true.

The calculation of these confidence levels adheres to the guidelines established in references [97]. The two scenarios being examined are as follows:

- *Scenario 1* : Exclusion of the SM with the addition of a new CP-mixed DM mediator, assuming the SM. In this instance, H_0 is the SM-only hypothesis, while H_1 is the SM plus a new CP-mixed DM mediator;

- *Scenario 2* : Exclusion of the SM with the addition of a new CP-mixed DM mediator, assuming the SM plus a new pure CP-even DM mediator has already been discovered. Here, H_0 is the SM plus a new CP-even DM mediator signal hypothesis, while H_1 is the SM plus a new CP-mixed DM mediator signal.

The limits evaluation considered both luminosity values, 300 fb^{-1} and 3000 fb^{-1}, and all the generated mediator masses. The contour plots illustrating the CL limits are depicted in the two-dimensional (g^S_{u33},g^P_{u33}) plane. For *Scenario 1*, the results for all the considered observables are depicted in Figure 30 for a mediator mass of 0.01 GeV. For results corresponding to different mediator masses, please consult Appendix B.

The 68% and 95% exclusion limits for both luminosity values are found in Tables 9, 10, and 11, using all the angular observables.

It is evident that all three observables exhibit similar exclusion limits. However, among the three, the standard b_2 observable shows a slight better exclusion. Furthermore, a consistent pattern emerges: the best exclusion is achieved when the mediator mass is 0.01 GeV. This is attributed to the behavior of the cross-section for the $t\bar{t}Y_0$ production, which is higher for low mediator masses.

Although, with an integrated luminosity of 3000 fb^{-1}, exclusion limits improve by roughly a factor of 2, already for 300 fb^{-1}, a considerable portion of the parameter space can already be excluded for *Scenario 1*.

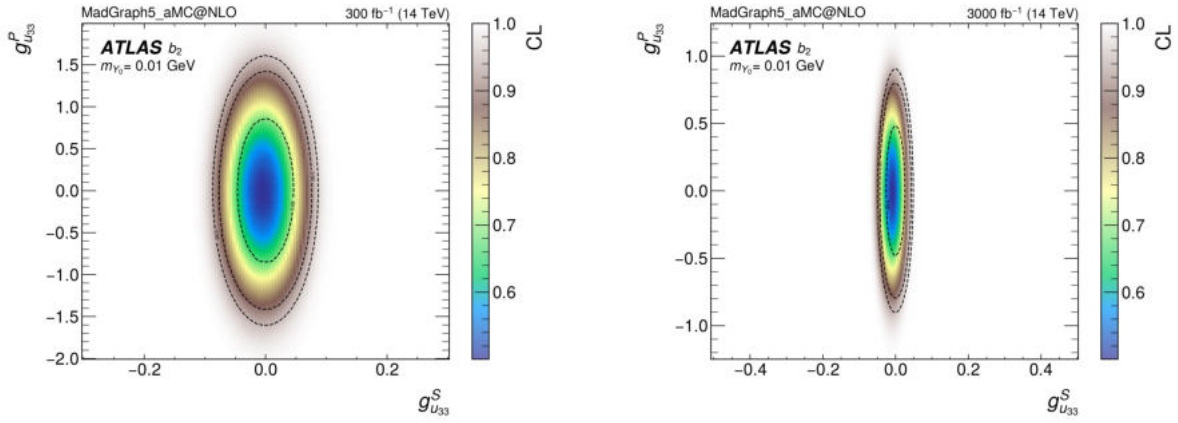

(a) b_2 ($m_{Y_0} = 0.01$ GeV)

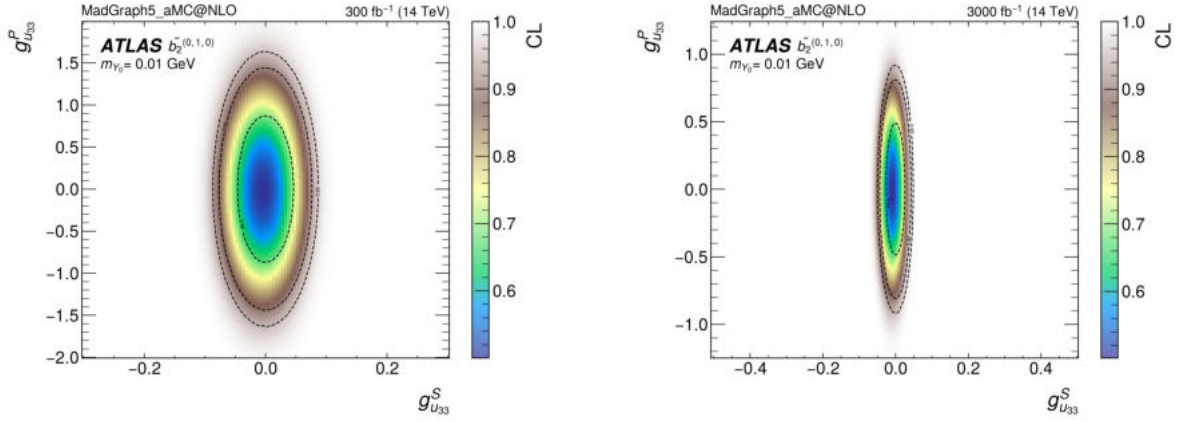

(b) $\tilde{b}_2^{(0,1,0)}$ ($m_{Y_0} = 0.01$ GeV)

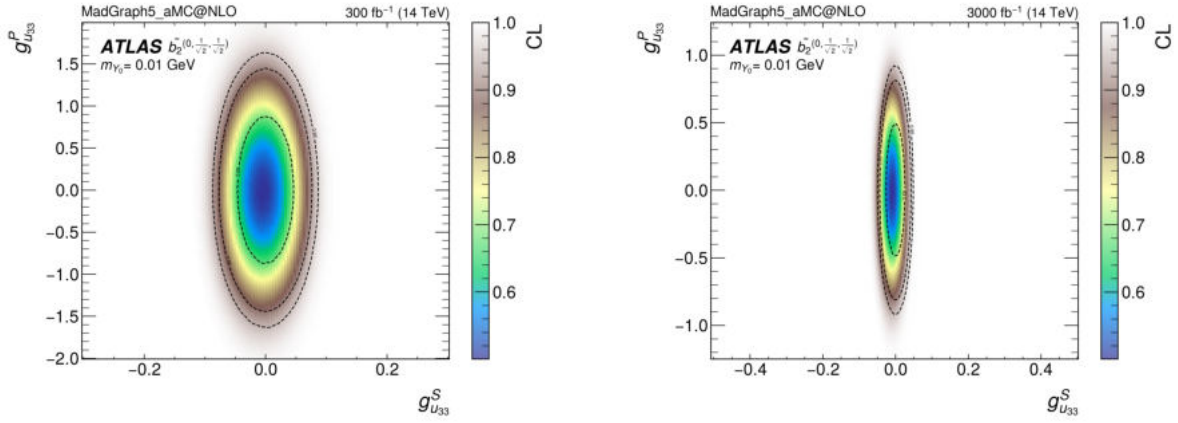

(c) $\tilde{b}_2^{(0,1/\sqrt{2},1/\sqrt{2})}$ ($m_{Y_0} = 0.01$ GeV)

Figure 30: CL limits for excluding the SM with a DM mediator, Y_0, characterized by mixed scalar and pseudo-scalar couplings with the top quarks, considering the SM as the null hypothesis, are shown for b_2 (upper plots), $\tilde{b}_2^{(0,1,0)}$ (middle plots), and $\tilde{b}_2^{(0,1/\sqrt{2},1/\sqrt{2})}$ (lower plots), for integrated luminosities of 300 and 3000 fb^{-1}.

Exclusion Limits from b_2

		300 fb^{-1}		3000 fb^{-1}	
m_{Y_0}		(68% CL)	(95% CL)	(68% CL)	(95% CL)
0.01 GeV	$g^S_{u33} \in$	$[-0.0475, 0.0425]$	$[-0.0875, 0.0875]$	$[-0.0225, 0.0225]$	$[-0.0475, 0.0475]$
	$g^S_{u33} \in$	$[-0.87, 0.87]$	$[-1.63, 1.63]$	$[-0.485, 0.475]$	$[-0.92, 0.91]$
1 GeV	$g^S_{u33} \in$	$[-0.0725, 0.0725]$	$[-0.1425, 0.1425]$	$[-0.0425, 0.0425]$	$[-0.0775, 0.0775]$
	$g^S_{u33} \in$	$[-0.87, 0.87]$	$[-1.65, 1.63]$	$[-0.485, 0.49]$	$[-0.92, 0.925]$
10 GeV	$g^S_{u33} \in$	$[-0.1375, 0.1375]$	$[-0.2575, 0.2625]$	$[-0.0775, 0.0775]$	$[-0.1425, 0.1475]$
	$g^S_{u33} \in$	$[-0.87, 0.89]$	$[-1.65, 1.67]$	$[-0.50, 0.49]$	$[-0.935, 0.94]$
100 GeV	$g^S_{u33} \in$	$[-0.76, 0.74]$	$[-1.41, 1.415]$	$[-0.4125, 0.4275]$	$[-0.7875, 0.7875]$
	$g^S_{u33} \in$	$[-1.25, 1.27]$	$[-2.37, 2.35]$	$[-0.70, 0.70]$	$[-1.325, 1.325]$
125 GeV	$g^S_{u33} \in$	$[-1.01, 1.015]$	$[-1.91, 1.915]$	$[-0.5775, 0.5775]$	$[-1.0725, 1.0725]$
	$g^S_{u33} \in$	$[-1.37, 1.35]$	$[-2.57, 2.59]$	$[-0.775, 0.775]$	$[-1.45, 1.45]$

Table 9: Exclusion limits for the $t\bar{t}Y_0$ CP-couplings, considering the *Scenario 1*, are depicted for various Y_0 masses under fixed luminosities of 300 fb^{-1} and 3000 fb^{-1}. The limits are presented at 68% and 95% confidence levels for the b_2 observable.

Exclusion Limits from $\tilde{b}_2^{(0,1,0)}$

		300 fb^{-1}		3000 fb^{-1}	
m_{Y_0}		(68% CL)	(95% CL)	(68% CL)	(95% CL)
0.01 GeV	$g^S_{u33} \in$	$[-0.0425, 0.0425]$	$[-0.0875, 0.0875]$	$[-0.0225, 0.0225]$	$[-0.0475, 0.0475]$
	$g^S_{u33} \in$	$[-0.87, 0.87]$	$[-1.65, 1.65]$	$[-0.485, 0.49]$	$[-0.935, 0.925]$
1 GeV	$g^S_{u33} \in$	$[-0.0725, 0.0725]$	$[-0.1425, 0.1425]$	$[-0.0425, 0.0425]$	$[-0.0775, 0.0775]$
	$g^S_{u33} \in$	$[-0.89, 0.89]$	$[-1.67, 1.67]$	$[-0.50, 0.49]$	$[-0.935, 0.94]$
10 GeV	$g^S_{u33} \in$	$[-0.1375, 0.1375]$	$[-0.2575, 0.2625]$	$[-0.0775, 0.0775]$	$[-0.1475, 0.1425]$
	$g^S_{u33} \in$	$[-0.89, 0.89]$	$[-1.69, 1.69]$	$[-0.50, 0.505]$	$[-0.95, 0.955]$
100 GeV	$g^S_{u33} \in$	$[-0.76, 0.765]$	$[-1.435, 1.44]$	$[-0.4275, 0.4275]$	$[-0.8025, 0.8025]$
	$g^S_{u33} \in$	$[-1.37, 1.39]$	$[-2.57, 2.59]$	$[-0.775, 0.775]$	$[-1.45, 1.45]$
125 GeV	$g^S_{u33} \in$	$[-1.06, 1.04]$	$[-1.985, 1.965]$	$[-0.5925, 0.5925]$	$[-1.1025, 1.1025]$
	$g^S_{u33} \in$	$[-1.57, 1.55]$	$[-2.93, 2.91]$	$[-0.875, 0.875]$	$[-1.625, 1.625]$

Table 10: Exclusion limits for the $t\bar{t}Y_0$ CP-couplings, considering the *Scenario 1*, are depicted for various Y_0 masses under fixed luminosities of 300 fb^{-1} and 3000 fb^{-1}. The limits are presented at 68% and 95% confidence levels for the $\tilde{b}_2^{(0,1,0)}$ observable.

Exclusion Limits from $\tilde{b}_2^{(0,1/\sqrt{2},1/\sqrt{2})}$

		300 fb^{-1}		3000 fb^{-1}	
m_{Y_0}		(68% CL)	(95% CL)	(68% CL)	(95% CL)
0.01 GeV	$g^S_{u33} \in$	$[-0.0475, 0.0425]$	$[-0.0875, 0.0875]$	$[-0.0225, 0.0225]$	$[-0.0475, 0.0475]$
	$g^S_{u33} \in$	$[-0.89, 0.87]$	$[-1.65, 1.65]$	$[-0.485, 0.49]$	$[-0.935, 0.925]$
1 GeV	$g^S_{u33} \in$	$[-0.0725, 0.0725]$	$[-0.1425, 0.1425]$	$[-0.0425, 0.0425]$	$[-0.0775, 0.0775]$
	$g^S_{u33} \in$	$[-0.89, 0.91]$	$[-1.67, 1.67]$	$[-0.50, 0.49]$	$[-0.935, 0.94]$
10 GeV	$g^S_{u33} \in$	$[-0.1375, 0.1375]$	$[-0.2625, 0.2575]$	$[-0.0775, 0.0775]$	$[-0.1425, 0.1475]$
	$g^S_{u33} \in$	$[-0.89, 0.91]$	$[-1.69, 1.69]$	$[-0.50, 0.505]$	$[-0.95, 0.955]$
100 GeV	$g^S_{u33} \in$	$[-0.76, 0.765]$	$[-1.435, 1.44]$	$[-0.4275, 0.4275]$	$[-0.8025, 0.8025]$
	$g^S_{u33} \in$	$[-1.37, 1.39]$	$[-2.61, 2.59]$	$[-0.775, 0.775]$	$[-1.45, 1.45]$
125 GeV	$g^S_{u33} \in$	$[-1.035, 1.04]$	$[-1.96, 1.965]$	$[-0.5925, 0.5925]$	$[-1.1025, 1.1025]$
	$g^S_{u33} \in$	$[-1.53, 1.55]$	$[-2.89, 2.91]$	$[-0.875, 0.875]$	$[-1.625, 1.625]$

Table 11: Exclusion limits for the $t\bar{t}Y_0$ CP-couplings, considering the *Scenario 1*, are depicted for various Y_0 masses under fixed luminosities of 300 fb^{-1} and 3000 fb^{-1}. The limits are presented at 68% and 95% confidence levels for the $\tilde{b}_2^{(0,1/\sqrt{2},1/\sqrt{2})}$ observable.

For *Scenario 2*, the primary aim here is to assess to which extent a mixed state can be excluded if a new pure CP-even mediator was discovered. The results for all considered observables are displayed in Figure 31, for a mediator mass of 0.01 GeV. For results from different mediator masses, please consult Appendix B.

Similar to *Scenario 1*, in *Scenario 2*, the b_2 observable continues to perform slightly better when compared to the new variables. All observables are most sensitive to the low-mass regions of the DM mediator, and as a result, the best exclusion limits are achieved in these regions. Finally, as expected, a clear improvement is seen in the various exclusion plots when using a luminosity of 3000 fb^{-1}.

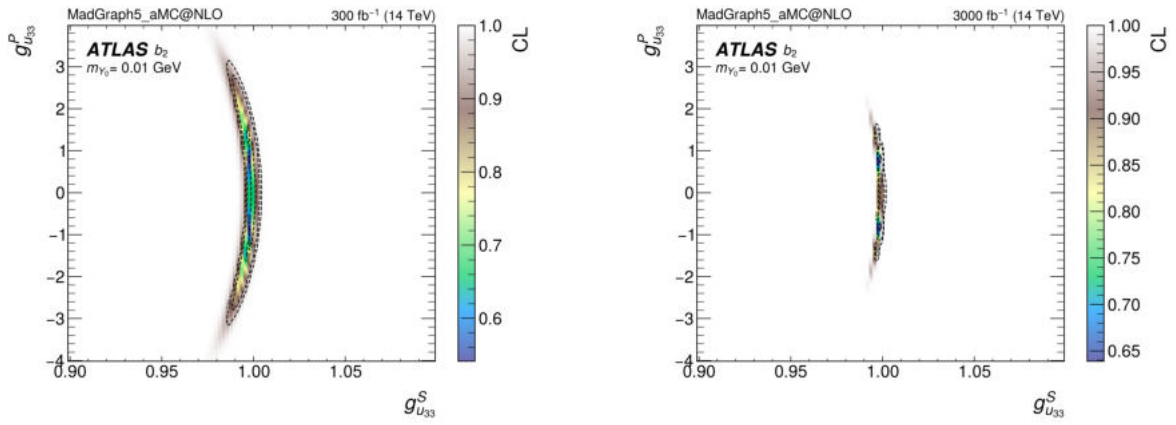

(a) b_2 ($m_{Y_0} = 0.01$ GeV)

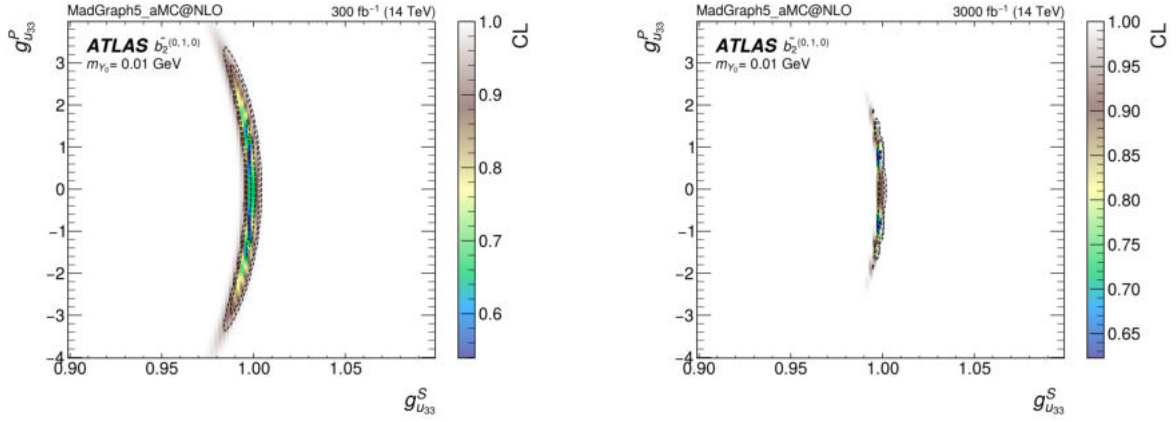

(b) $\tilde{b}_2^{(0,1,0)}$ ($m_{Y_0} = 0.01$ GeV)

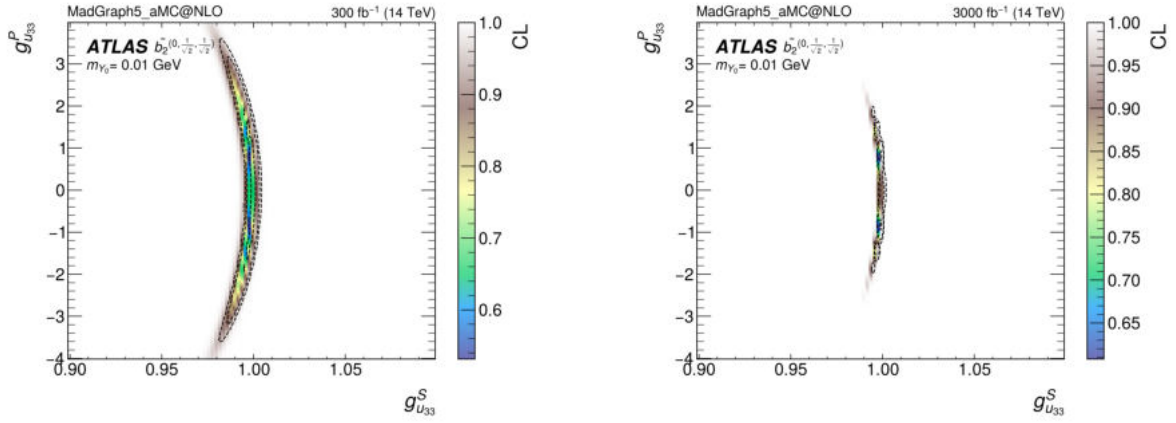

(c) $\tilde{b}_2^{(0,1/\sqrt{2},1/\sqrt{2})}$ ($m_{Y_0} = 0.01$ GeV)

Figure 31: CL limits for excluding the SM with a DM mediator, Y_0, characterized by mixed scalar and pseudo-scalar couplings with the top quarks, considering the SM plus a pure scalar DM mediator as the null hypothesis, are shown for b_2 (upper plots), $\tilde{b}_2^{(0,1,0)}$ (middle plots), and $\tilde{b}_2^{(0,1/\sqrt{2},1/\sqrt{2})}$ (lower plots), for integrated luminosities of 300 and 3000 fb^{-1}.

Part IV

Conclusion

Chapter 5

Conclusion and Outlook

In this thesis, a search for DM mediators produced in association with $t\bar{t}$ events ($t\bar{t}Y_0$) at the LHC was conducted, with the $t\bar{t}$ system assumed to decay dileptonically. The search was conducted within the framework of simplified models of DM production at colliders.

The reconstruction of the kinematics of the $t\bar{t}$ system observed in $t\bar{t}Y_0$ events was achieved, holding a novel approach in the search for DM. Multiple mediator mass scenarios were taken into account during this analysis, adding to its comprehensiveness. In the kinematic reconstruction, the missing transverse energy was entirely attributed to the undetected neutrinos, with no attempt made to reconstruct the invisible DM mediator. Intermediate particles were also reconstructed with their specified masses. The resulting correlations (Figures 25 and 26) between the generated and reconstructed kinematics were strong, with reconstruction efficiencies ranging from 47% to 62%, depending on the mediator mass considered. A dedicated multivariate statistical method was effectively employed to find the best pairing of the b-jets and charged leptons originating from the same top quark decay.

New angular observables in the context of DM searches were introduced ($\tilde{b}_2^{(0,1,0)}$ and $\tilde{b}_2^{(0,1/\sqrt{2},1/\sqrt{2})}$). These observables were found to be sensitive to different DM mediator masses with different CP properties in their interactions with heavy SM particles. The angular distributions were employed to establish exclusion limits for two distinct scenarios: *Scenario 1*, where the SM is assumed as the null hypothesis, and *Scenario 2*, where the null hypothesis comprises the SM plus a pure scalar DM mediator. This last scenario serves as a benchmark in order to assess the sensitivity of the analysis to a potential CP-mixed nature of the DM mediator, if a pure scalar mediator was found. This study considered various mediator masses and evaluated exclusion limits for two integrated luminosities: 300 fb^{-1}, corresponding to the expected final integrated luminosity at the end of *LHC Run 3*, and 3000 fb^{-1}, corresponding to the expected full luminosity during the High-Luminosity Phase of the LHC.

For *Scenario 1*, when comparing all three variables, the b_2 variable exhibited a slight advantage in constraining the parameter space of g_{u33}^S and g_{u33}^P across all the considered mediator masses. Further-

more, it is noteworthy that, the exclusion limits deteriorated as the mediator mass increased. This trend was attributed to the behavior of the $t\bar{t}Y_0$ cross-section, which decreases significantly for high mass mediators. The results for *Scenario 1* presented in Tables 9, 10, and 11, allowed also to infer that with just 300 fb^{-1} of integrated luminosity a significant portion of the parameter space can already be excluded. For instance, for the b_2 observable and a mediator mass of 0.01 GeV, the best exclusion limits at 95% confidence level were set to $g^S_{u_{33}} \in [-0.0475, 0.0425]$ and $g^P_{u_{33}} \in [-0.87, 0.87]$.

Similar observations remained valid in the context of *Scenario 2*. The b_2 still stood out as the best observable, especially in its capacity to better limit the pseudo-scalar nature of DM couplings to the top quark. Also, the impact of the mediator mass on the exclusion limits still prevailed. In both scenarios, as the luminosity reached 3000 fb^{-1}, clear improvements were observed in the exclusion limits.

In conclusion, this dissertation introduces a novel approach to searching for DM in particle colliders. It explores the use of new variables to establish exclusion limits on the scalar and pseudo-scalar nature of the top quark couplings to the DM mediator. The study considers a wide range of DM mediator masses, all within a simplified DM model framework. Future searches include investigating other decay channels, particularly the semi-leptonic decay channel, which is more common than the dileptonic decay and offers opportunities for testing additional observables and techniques. Moreover, a forthcoming paper will explore new observables beyond those presented in this thesis, and ongoing searches are also exploring the possibility of replicating a similar analysis for a spin-1 and spin-2 DM mediator. These studies are currently in progress and will be published soon, heralding exciting prospects for new physics related to Dark Matter.

Bibliography

[1] Sheldon L. Glashow. Partial-symmetries of weak interactions. *Nuclear Physics*, 22(4):579–588, 1961.

[2] Steven Weinberg. A model of leptons. *Phys. Rev. Lett.*, 19:1264–1266, Nov 1967.

[3] Salam Abdus. *Weak and electromagnetic interactions*, pages 244–254.

[4] The ATLAS collaboration. Observation of a new particle in the search for the standard model higgs boson with the ATLAS detector at the LHC. *Physics Letters B*, 716(1):1–29, sep 2012.

[5] The CMS collaboration. Observation of a new boson at a mass of 125 GeV with the CMS experiment at the LHC. *Physics Letters B*, 716(1):30–61, sep 2012.

[6] Katherine Garrett and Gintaras Duda. Dark matter: A primer. *Advances in Astronomy*, 2011:1–22, 2011.

[7] The Planck Collaboration. Planck 2018 results. vi. cosmological parameters. *Astronomy & Astrophysics*, 641:A6, sep 2020.

[8] Jalal Abdallah and Others. Simplified models for dark matter searches at the LHC. *Physics of the Dark Universe*, 9-10:8–23, sep 2015.

[9] John F. Gunion and Xiao-Gang He. Determining the CP nature of a neutral higgs boson at the CERN large hadron collider. *Physical Review Letters*, 76(24):4468–4471, jun 1996.

[10] The ATLAS Collaboration. The atlas experiment at the cern large hadron collider. *Journal of Instrumentation*, 3(08):S08003, aug 2008.

[11] J. de Favereau, , C. Delaere, P. Demin, A. Giammanco, V. Lemaître, A. Mertens, and M. Selvaggi. DELPHES 3: a modular framework for fast simulation of a generic collider experiment. *Journal of High Energy Physics*, 2014(2), feb 2014.

[12] Alexandre Mertens. New features in delphes 3. *Journal of Physics: Conference Series*, 608(1):012045, apr 2015.

[13] Mihailo Backović, Michael Krämer, Fabio Maltoni, Antony Martini, Kentarou Mawatari, and Mathieu Pellen. Higher-order qcd predictions for dark matter production at the lhc in simplified models with s-channel mediators, 2015.

[14] Volker Andreas Austrup. *Search for scalar and vector leptoquarks decaying into quarks and leptons of different generations*. PhD thesis, 2022. Presented 01 Dec 2022.

[15] Particle Data Group and Workman. Review of Particle Physics. *Progress of Theoretical and Experimental Physics*, 2022(8), 08 2022. 083C01.

[16] R. L. Workman and Others. Review of Particle Physics. *PTEP*, 2022:083C01, 2022.

[17] The Nobel Prize in Physics. Summary - nobel prize in physics 2015, 2015.

[18] Galen Rhodes Gledhill. *Two Searches for Signals of Dark Matter with the ATLAS Detector in 139* fb^{-1} *of LHC* $\sqrt{s}$ *= 13 TeV Proton-Proton Collision Data*. PhD thesis, 2022. Presented 21 Nov 2022.

[19] Janosh Riebesell. TikZ - Higgs Potential. Adapted from https://tikz.net/higgs-potential/. [Online; accessed 11-July-2023].

[20] Susana Patrícia Amor dos Santos. *Study of ATLAS sensitivity to the single top s-channel production*. PhD thesis, 2010. Presented 23 Jul 2010.

[21] The ATLAS, CDF, CMS, and D0 Collaborations. First combination of tevatron and lhc measurements of the top-quark mass, 2014.

[22] CDF Collaboration. Observation of top quark production in $\bar{p}p$ collisions with the collider detector at fermilab. *Phys. Rev. Lett.*, 74:2626–2631, Apr 1995.

[23] D0 Collaboration. Observation of the top quark. *Phys. Rev. Lett.*, 74:2632–2637, Apr 1995.

[24] TtbarNNLO. CERN TWiki. https://twiki.cern.ch/twiki/bin/view/LHCPhysics/TtbarNNLO.

[25] M. "Beneke, I. Efthymiopoulos, Michelangelo L. Mangano, J. Womersley, A. Ahmadov, G. Azuelos, U. Baur, A. Belyaev, Berger, and et al. Top Quark Physics. pages 419–529, 2000.

[26] Measurement of spin correlation in top–antitop quark events and search for top squark pair production in proton–proton collisions at $\sqrt{s}$=8 TeV using the ATLAS detector. Technical report, CERN, Geneva, 2014. All figures including auxiliary figures are available at https://atlas.web.cern.ch/Atlas/GROUPS/PHYSICS/CONFNOTES/ATLAS-CONF-2014-056.

[27] J.H. Oort. The force exerted by the stellar system in the direction perpendicular to the galactic plane and some related problems. *Bulletin of the Astronomical Institutes of the Netherlands*, 6:249, 1932.

[28] V. C. Rubin, Jr. Ford, W. K., and N. Thonnard. Rotational properties of 21 SC galaxies with a large range of luminosities and radii, from NGC 4605 (R=4kpc) to UGC 2885 (R=122kpc). *ApJ Lett.*, 238:471–487, June 1980.

[29] Guglielmo Frattari. *Investigating the nature of dark matter and of the Higgs boson with jets and missing transverse momentum at the LHC*. PhD thesis, 2021. Presented 22 Feb 2022.

[30] Hubble Space Telescope Image. https://esahubble.org/images/opo9610a/. Accessed on July 3, 2023.

[31] W.N. Colley and E. Turner and J.A. Tyson and HST and NASA. Giant Cluster Bends. Astronomy Picture of the Day, 1994. https://apod.nasa.gov/apod/ap980614.html.

[32] Matthias Bartelmann. Gravitational lensing. *Classical and Quantum Gravity*, 27(23):233001, nov 2010.

[33] Douglas Clowe, Maruša Bradač, Anthony H. Gonzalez, Maxim Markevitch, Scott W. Randall, Christine Jones, and Dennis Zaritsky. A direct empirical proof of the existence of dark matter. *The Astrophysical Journal*, 648(2):L109–L113, aug 2006.

[34] A. A. Penzias and R. W. Wilson. A Measurement of Excess Antenna Temperature at 4080 Mc/s. *ApJ Lett.*, 142:419–421, July 1965.

[35] Albert Einstein. The Field Equations of Gravitation. *Sitzungsber. Preuss. Akad. Wiss. Berlin (Math. Phys.)*, 1915:844–847, 1915.

[36] Edwin Hubble. A Relation between Distance and Radial Velocity among Extra-Galactic Nebulae. *Proceedings of the National Academy of Science*, 15(3):168–173, March 1929.

[37] John D. Barrow and Richard A. Matzner. The homogeneity and isotropy of the Universe. *Monthly Notices of the Royal Astronomical Society*, 181(4):719–727, 12 1977.

[38] A. Friedman. Über die krümmung des raumes. *Zeitschrift für Physik*, 10:377–386, 1922.

[39] John Mather, E. Cheng, D. Cottingham, Robert Eplee, D. Fixsen, Tilak Hewagama, R. Isaacman, K. Jensen, Stephan Meyer, and P. Noerdlinger. Measurement of the cosmic microwave background spectrum by the cobe firas instrument. *The Astrophysical Journal*, 420:439–444, 01 1994.

[40] Planck Collaboration. Planck 2018 results - iv. diffuse component separation. *A&A*, 641:A4, 2020.

[41] Daniel Baumann. *Cosmology*. Cambridge University Press, 2022.

[42] Gary Steigman, Basudeb Dasgupta, and John F. Beacom. Precise relic WIMP abundance and its impact on searches for dark matter annihilation. *Physical Review D*, 86(2), jul 2012.

[43] Jalal Abdallah and Others. Simplified models for dark matter and missing energy searches at the lhc, 2014.

[44] Daniel Abercrombie and Others. Dark matter benchmark models for early LHC run-2 searches: Report of the ATLAS/CMS dark matter forum. *Physics of the Dark Universe*, 27:100371, jan 2020.

[45] Lyndon R Evans and Philip Bryant. LHC Machine. *JINST*, 3:S08001, 2008. This report is an abridged version of the LHC Design Report (CERN-2004-003).

[46] The ALICE Collaboration. The alice experiment at the cern lhc. *Journal of Instrumentation*, 3(08):S08002, aug 2008.

[47] The LHCb Collaboration. The lhcb detector at the lhc. *Journal of Instrumentation*, 3(08):S08005, aug 2008.

[48] The CMS Collaboration. The cms experiment at the cern lhc. *Journal of Instrumentation*, 3(08):S08004, aug 2008.

[49] CERN. Pulling together superconducting electromagnets. https://home.cern/science/engineering/pulling-together-superconducting-electromagnets. Accessed: June 27, 2023.

[50] Ewa Lopienska. The CERN accelerator complex, layout in 2022. Complexe des accélérateurs du CERN en janvier 2022. 2022. General Photo.

[51] R Alemany-Fernandez, E Bravin, L Drosdal, A Gorzawski, V Kain, M Lamont, A Macpherson, G Papotti, M Pojer, L Ponce, S Redaelli, G Roy, M Solfaroli Camillocci, W Venturini, and J Wenninger. Operation and Configuration of the LHC in Run 1. 2013.

[52] J. T. Boyd. Lhc run-2 and future prospects, 2020.

[53] Fabienne Landua. LHC upgrade during LS2 in four languages. 2022. General Photo.

[54] Frederick Bordry, Michael Benedikt, Oliver Bruning, John Jowett, Lucio Rossi, Daniel Schulte, Steinar Stapnes, and Frank Zimmermann. Machine parameters and projected luminosity performance of proposed future colliders at cern, 2018.

[55] CERN EP News. Atlas faces the challenge of run 3. https://ep-news.web.cern.ch/content/atlas-faces-challenge-run-3, 2021.

[56] B Salvachua. Overview of Proton-Proton Physics during Run 2. pages 7–14, 2019.

[57] O. Aberle and Others. *High-Luminosity Large Hadron Collider (HL-LHC): Technical design report*. CERN Yellow Reports: Monographs. CERN, Geneva, 2020.

[58] S. Fartoukh and Others. LHC Configuration and Operational Scenario for Run 3. Technical report, CERN, Geneva, 2021.

[59] ATLAS Collaboration. Luminosity Public Results - Run 3. https://twiki.cern.ch/twiki/bin/view/AtlasPublic/LuminosityPublicResultsRun3, 2022. Accessed: May 1, 2023.

[60] Atlas experiment. https://atlas.cern/Discover/Detector. Accessed: May 3, 2023.

[61] Izaak Neutelings. TikZ - Axis 3D CMS. Adapted from https://tikz.net/axis3d_cms/. [Online; accessed 9-May-2023].

[62] Atlas experiment - inner detector. https://atlas.cern/Discover/Detector/Inner-Detector. Accessed: June 8, 2023.

[63] *ATLAS inner detector: Technical Design Report, 1*. Technical design report. ATLAS. CERN, Geneva, 1997.

[64] M Capeans, G Darbo, K Einsweiller, M Elsing, T Flick, M Garcia-Sciveres, C Gemme, H Pernegger, O Rohne, and R Vuillermet. ATLAS Insertable B-Layer Technical Design Report. Technical report, 2010.

[65] Joao Pequenao. Computer generated image of the ATLAS inner detector. 2008.

[66] *ATLAS calorimeter performance: Technical Design Report*. Technical design report. ATLAS. CERN, Geneva, 1996.

[67] CERN. Atlas experiment - calorimeter. https://atlas.cern/Discover/Detector/Calorimeter. Accessed: June 8, 2023.

[68] Joao Pequenao. Computer Generated image of the ATLAS calorimeter. 2008.

[69] T. Barillari. The ATLAS liquid argon hadronic end-cap calorimeter: construction and selected beam test results. *Nuclear Physics B - Proceedings Supplements*, 150:102–105, jan 2006.

[70] Joao Pequenao. Computer generated image of the ATLAS Muons subsystem. 2008.

[71] CERN. Atlas experiment - trigger and data acquisition. https://atlas.cern/Discover/Detector/Trigger-DAQ. Accessed: June 8, 2023.

[72] The ATLAS collaboration. Operation of the ATLAS trigger system in run 2. *Journal of Instrumentation*, 15(10):P10004–P10004, oct 2020.

[73] S Xella. Physics objects reconstruction in the ATLAS experiment. Technical report, CERN, Geneva, 2013.

[74] Emanuel Demétrio Mendes Gouveia. Search for tth production at the lhc. Master's thesis, 2016.

[75] Sebastien Rettie. Muon identification and performance in the atlas experiment. page 097, 09 2018.

[76] Matteo Cacciari, Gavin P. Salam, and Gregory Soyez. The anti-kt jet clustering algorithm. *Journal of High Energy Physics*, 2008(04):063, apr 2008.

[77] Jet energy scale and its systematic uncertainty in proton-proton collisions at sqrt(s)=7 TeV in ATLAS 2010 data. Technical report, CERN, Geneva, 2011. All figures including auxiliary figures are available at https://atlas.web.cern.ch/Atlas/GROUPS/PHYSICS/CONFNOTES/ATLAS-CONF-2011-032.

[78] Performance of Missing Transverse Momentum Reconstruction in ATLAS with 2011 Proton-Proton Collisions at $sqrts$ = 7 TeV. 7 2012.

[79] Expected performance of the ATLAS b-tagging algorithms in Run-2. Technical report, CERN, Geneva, 2015. All figures including auxiliary figures are available at https://atlas.web.cern.ch/Atlas/GROUPS/PHYSICS/PUBNOTES/ATL-PHYS-PUB-2015-022.

[80] Matteo Cacciari, Gavin P. Salam, and Gregory Soyez. FastJet User Manual. *Eur. Phys. J. C*, 72:1896, 2012.

[81] J. Alwall, R. Frederix, S. Frixione, V. Hirschi, F. Maltoni, O. Mattelaer, H.-S. Shao, T. Stelzer, P. Torrielli, and M. Zaro. The automated computation of tree-level and next-to-leading order differential cross sections, and their matching to parton shower simulations. *Journal of High Energy Physics*, 2014(7), jul 2014.

[82] R. Frederix, S. Frixione, V. Hirschi, D. Pagani, H.-S. Shao, and M. Zaro. The automation of next-to-leading order electroweak calculations. *Journal of High Energy Physics*, 2018(7), jul 2018.

[83] Pierre Artoisenet, Rikkert Frederix, Olivier Mattelaer, and Robbert Rietkerk. Automatic spin-entangled decays of heavy resonances in monte carlo simulations. *Journal of High Energy Physics*, 2013(3), mar 2013.

[84] Torbjörn Sjöstrand, Stephen Mrenna, and Peter Skands. PYTHIA 6.4 physics and manual. *Journal of High Energy Physics*, 2006(05):026–026, may 2006.

[85] LHCPhysics: Single Top Reference Cross Sections. https://twiki.cern.ch/twiki/bin/view/LHCPhysics/SingleTopRefXsec#Citation. Accessed: July 18, 2023.

[86] John Campbell, Tobias Neumann, and Zack Sullivan. Single-top-quark production in the t-channel at NNLO. *JHEP*, 02:040, 2021.

[87] Richard D. Ball et al. The PDF4LHC21 combination of global PDF fits for the LHC Run III. *J. Phys. G*, 49(8):080501, 2022.

[88] Nikolaos Kidonakis and Nodoka Yamanaka. Higher-order corrections for tW production at high-energy hadron colliders. *JHEP*, 05:278, 2021.

[89] LHCPhysics: Top Quark Pair Production at NNLO in QCD. https://twiki.cern.ch/twiki/bin/view/LHCPhysics/TtbarNNLO. Accessed: July 18, 2023.

[90] Ulrich Haisch, Priscilla Pani, and Giacomo Polesello. Determining the CP nature of spin-0 mediators in associated production of dark matter and $t\bar{t}$ pairs. *Journal of High Energy Physics*, 2017(2), feb 2017.

[91] Eric Conte, Benjamin Fuks, and Guillaume Serret. MadAnalysis 5, a user-friendly framework for collider phenomenology. *Computer Physics Communications*, 184(1):222–256, jan 2013.

[92] I. Antcheva, M. Ballintijn, B. Bellenot, M. Biskup, R. Brun, N. Buncic, Ph. Canal, D. Casadei, O. Couet, V. Fine, L. Franco, G. Ganis, A. Gheata, D. Gonzalez Maline, M. Goto, J. Iwaszkiewicz, A. Kreshuk, D. Marcos Segura, R. Maunder, L. Moneta, A. Naumann, E. Offermann, V. Onuchin, S. Panacek, F. Rademakers, P. Russo, and M. Tadel. ROOT a c++ framework for petabyte data storage, statistical analysis and visualization. *Computer Physics Communications*, 180(12):2499–2512, dec 2009.

[93] A. Hoecker, P. Speckmayer, J. Stelzer, J. Therhaag, E. von Toerne, H. Voss, M. Backes, T. Carli, O. Cohen, A. Christov, D. Dannheim, K. Danielowski, S. Henrot-Versille, M. Jachowski, K. Kraszewski, A. Krasznahorkay Jr. au2, M. Kruk, Y. Mahalalel, R. Ospanov, X. Prudent, A. Robert, D. Schouten, F. Tegenfeldt, A. Voigt, K. Voss, M. Wolter, and A. Zemla. Tmva - toolkit for multivariate data analysis, 2009.

[94] E. Gouveia, S. P. Amor dos Santos, M. C. N. Fiolhais, R. Frederix, R. Gonçalo, R. Martins, A. Onofre, C. M. Pease, H. Peixoto, A. Reigoto, R. Santos, and J. Silva. Probing the cp nature of the higgs coupling in $t\bar{t}h$ events at the lhc, 2018.

[95] Emanuel Gouveia, Ricardo Gonçalo, António Onofre, and Duarte Azevedo. Measuring the cp structure of the top yukawa coupling in $t\bar{t}h$ events at the lhc, 2019.

[96] Duarte Azevedo, Rodrigo Capucha, António Onofre, and Rui Santos. Scalar mass dependence of angular variables in $tt\phi$ production. *Journal of High Energy Physics*, 2020(6), jun 2020.

[97] A L Read. Presentation of search results: the cls technique. *Journal of Physics G: Nuclear and Particle Physics*, 28(10):2693, sep 2002.

Part V
Appendices

Appendix A
Correlation Plots

In this appendix, additional correlation plots relevant to other DM mediator masses and reconstruction methods are presented. Appendix A.1 is dedicated to the reconstruction with truth-match, while Appendix A.2 shows results for the reconstruction without truth-match.

A.1 Reconstruction with Truth-Match

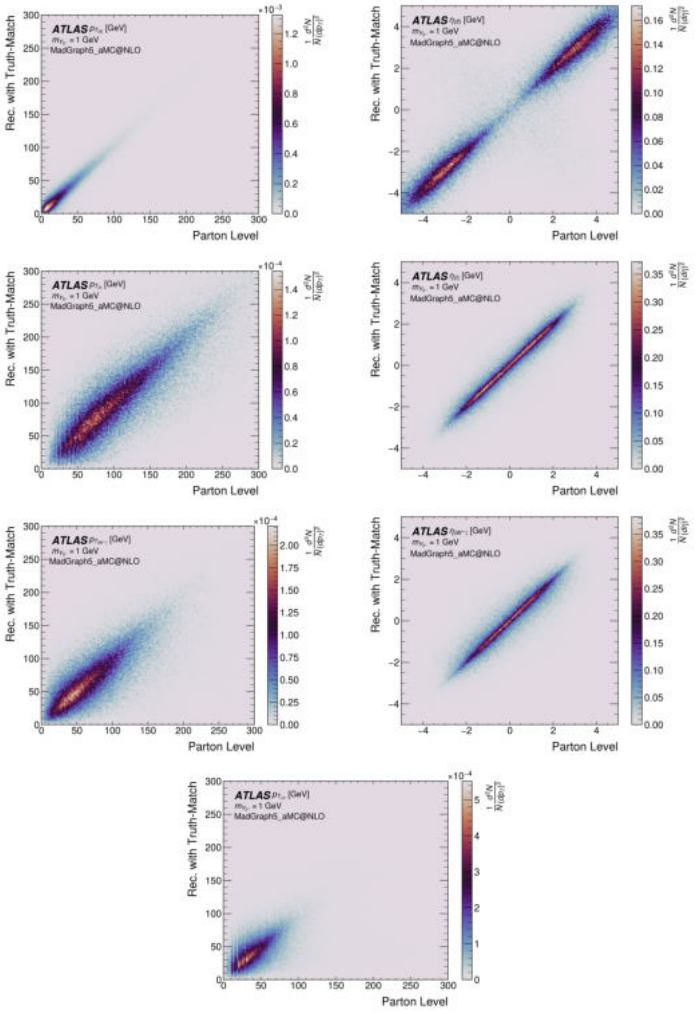

Figure 32: Two-dimensional kinematic distributions for $t\bar{t}Y_0$ events with $m_{Y_0} = 1$ GeV ($J^{CP} = 0^+$).

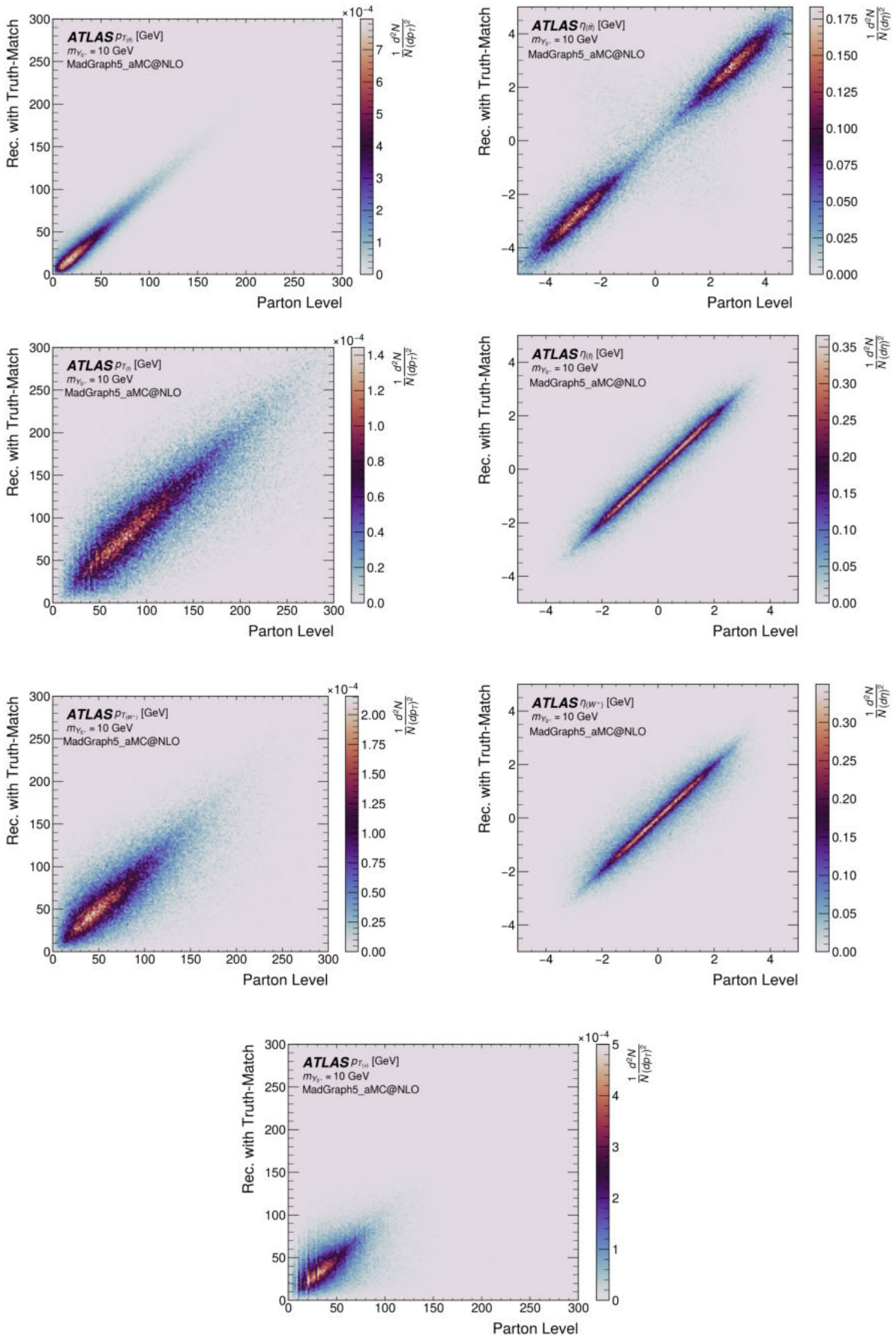

Figure 33: Two-dimensional kinematic distributions for $t\bar{t}Y_0$ events with $m_{Y_0} = 10$ GeV ($J^{CP} = 0^+$).

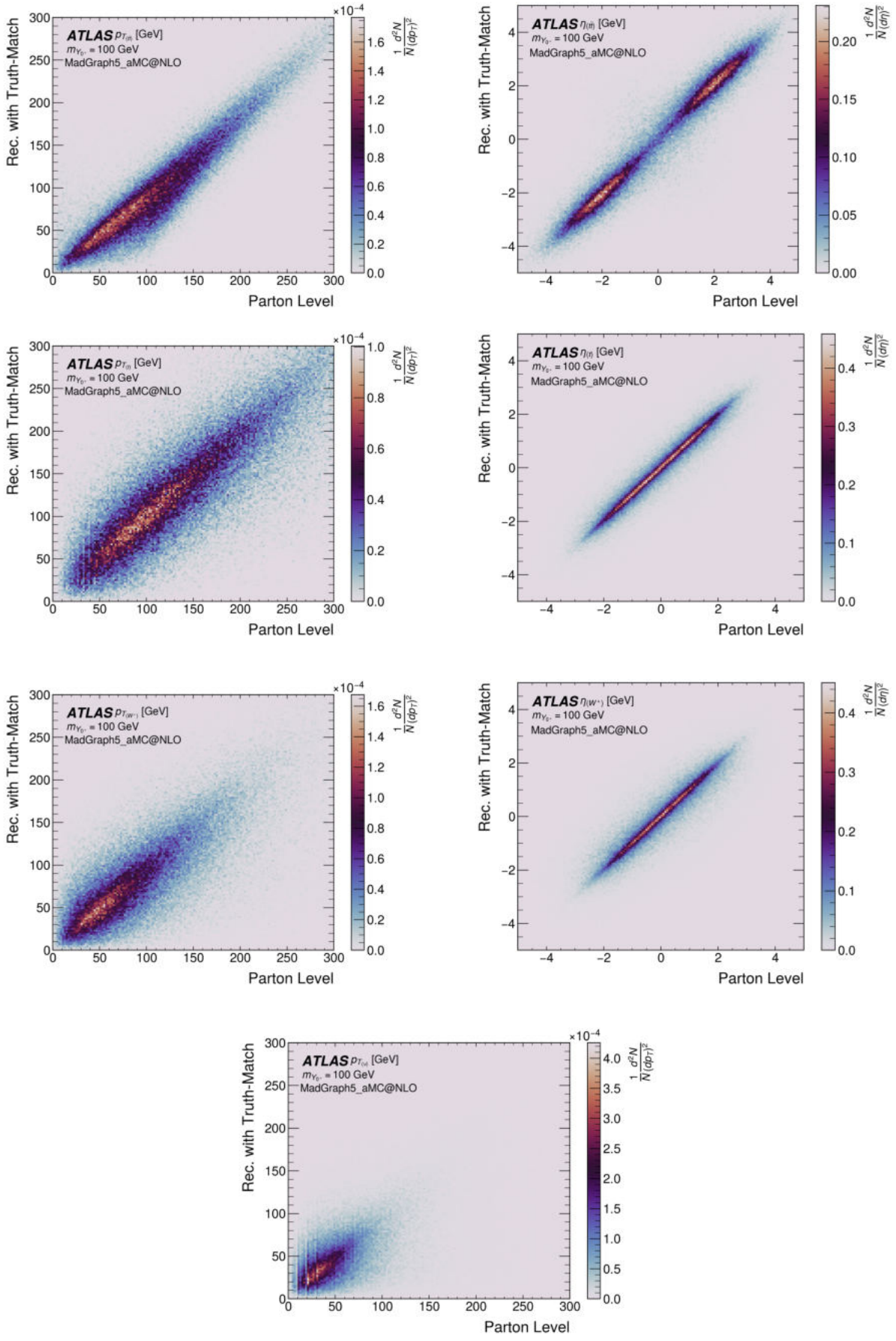

Figure 34: Two-dimensional kinematic distributions for $t\bar{t}Y_0$ events with $m_{Y_0} = 100$ GeV ($J^{CP} = 0^+$).

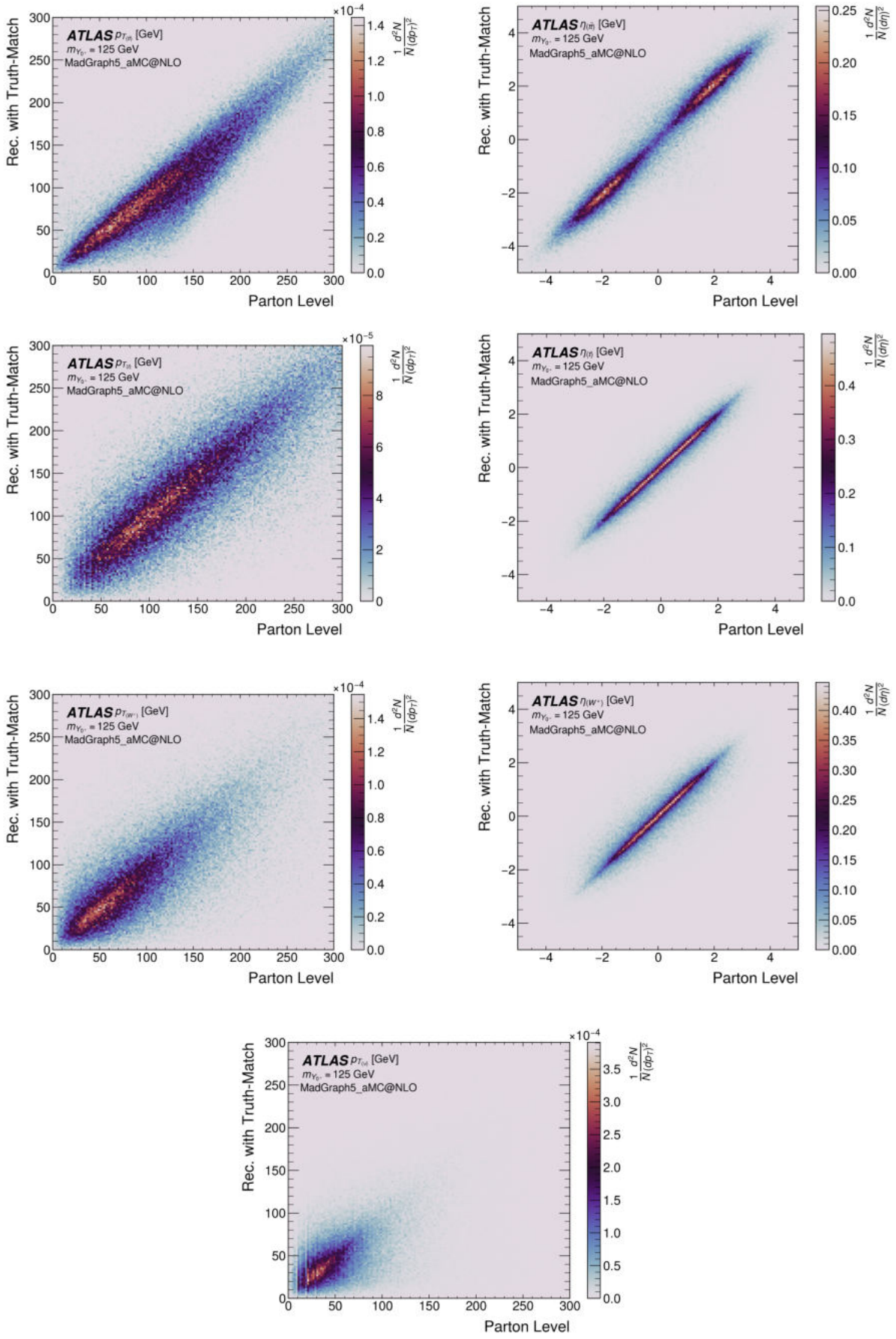

Figure 35: Two-dimensional kinematic distributions for $t\bar{t}Y_0$ events with $m_{Y_0} = 125$ GeV ($J^{CP} = 0^+$).

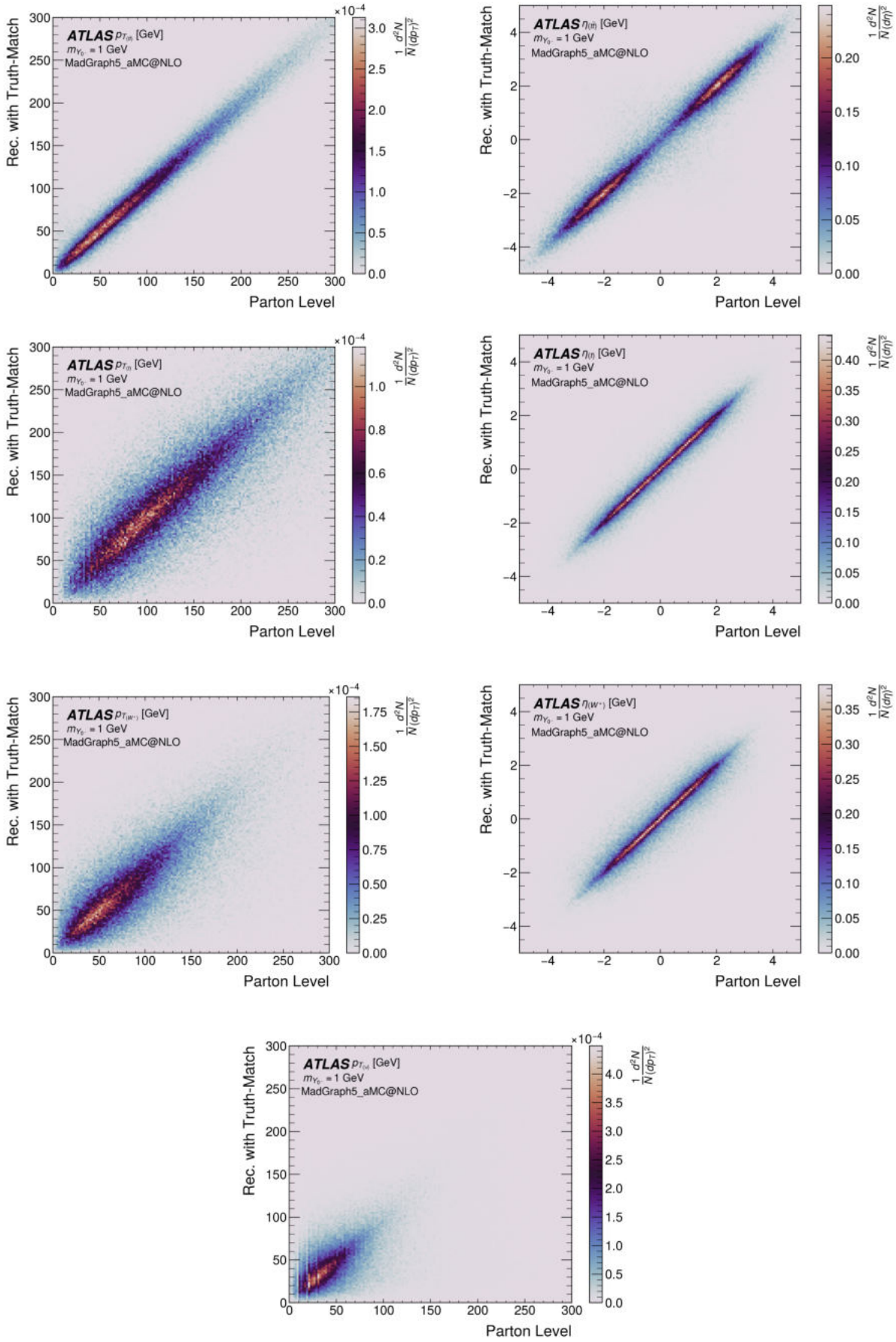

Figure 36: Two-dimensional kinematic distributions for $t\bar{t}Y_0$ events with $m_{Y_0} = 1$ GeV ($J^{CP} = 0^-$).

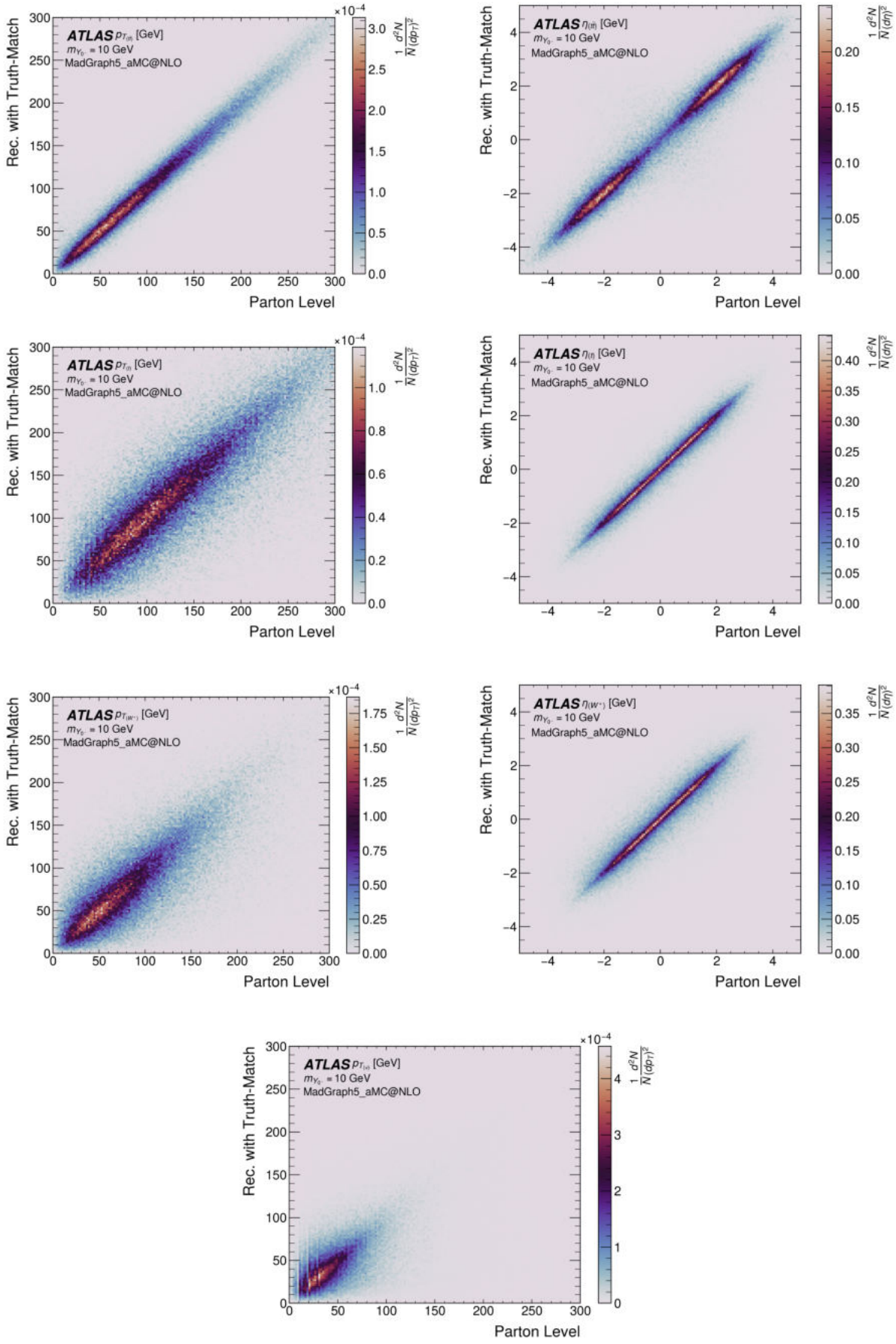

Figure 37: Two-dimensional kinematic distributions for $t\bar{t}Y_0$ events with $m_{Y_0} = 10$ GeV ($J^{CP} = 0^-$).

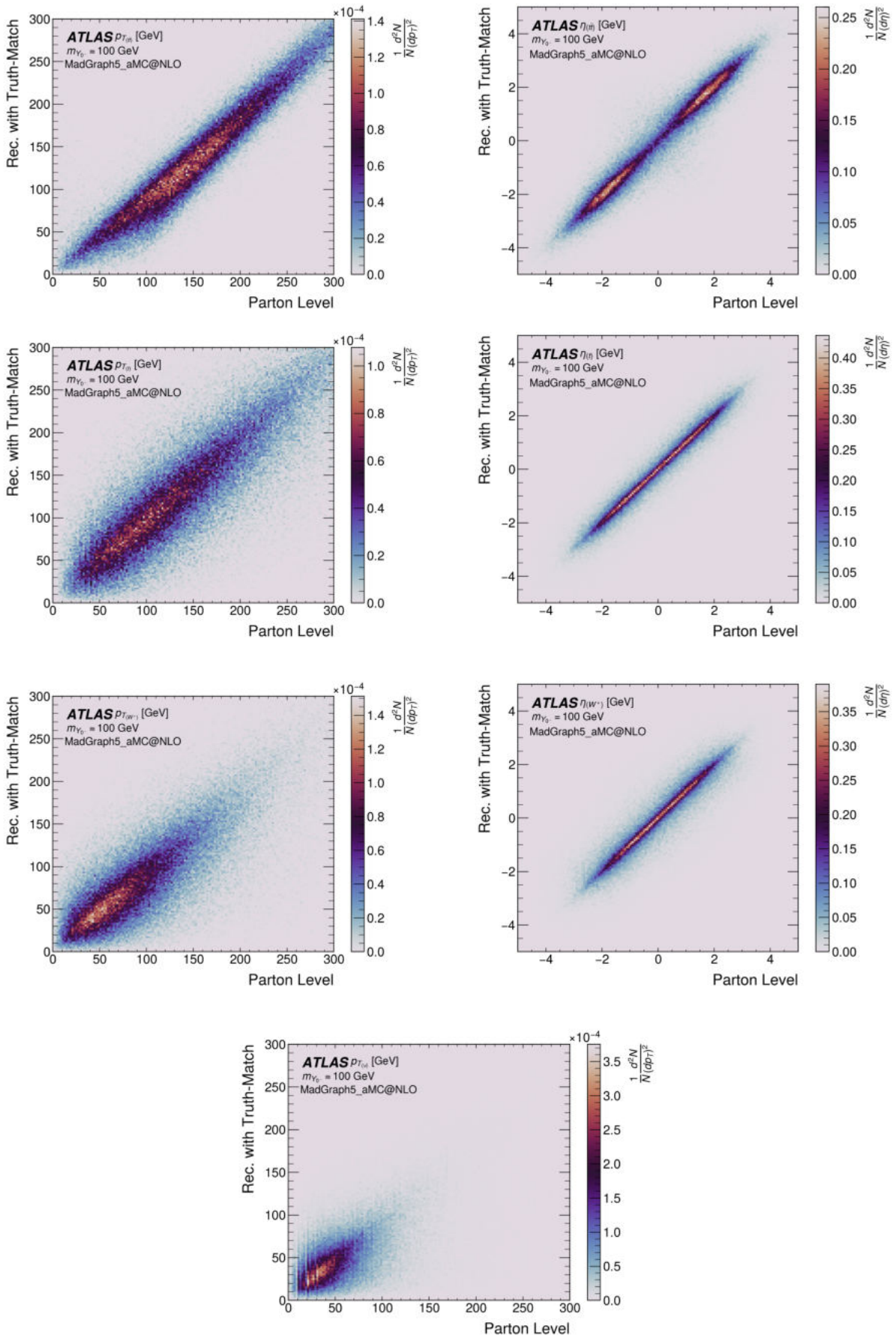

Figure 38: Two-dimensional kinematic distributions for $t\bar{t}Y_0$ events with $m_{Y_0} = 100$ GeV ($J^{CP} = 0^-$).

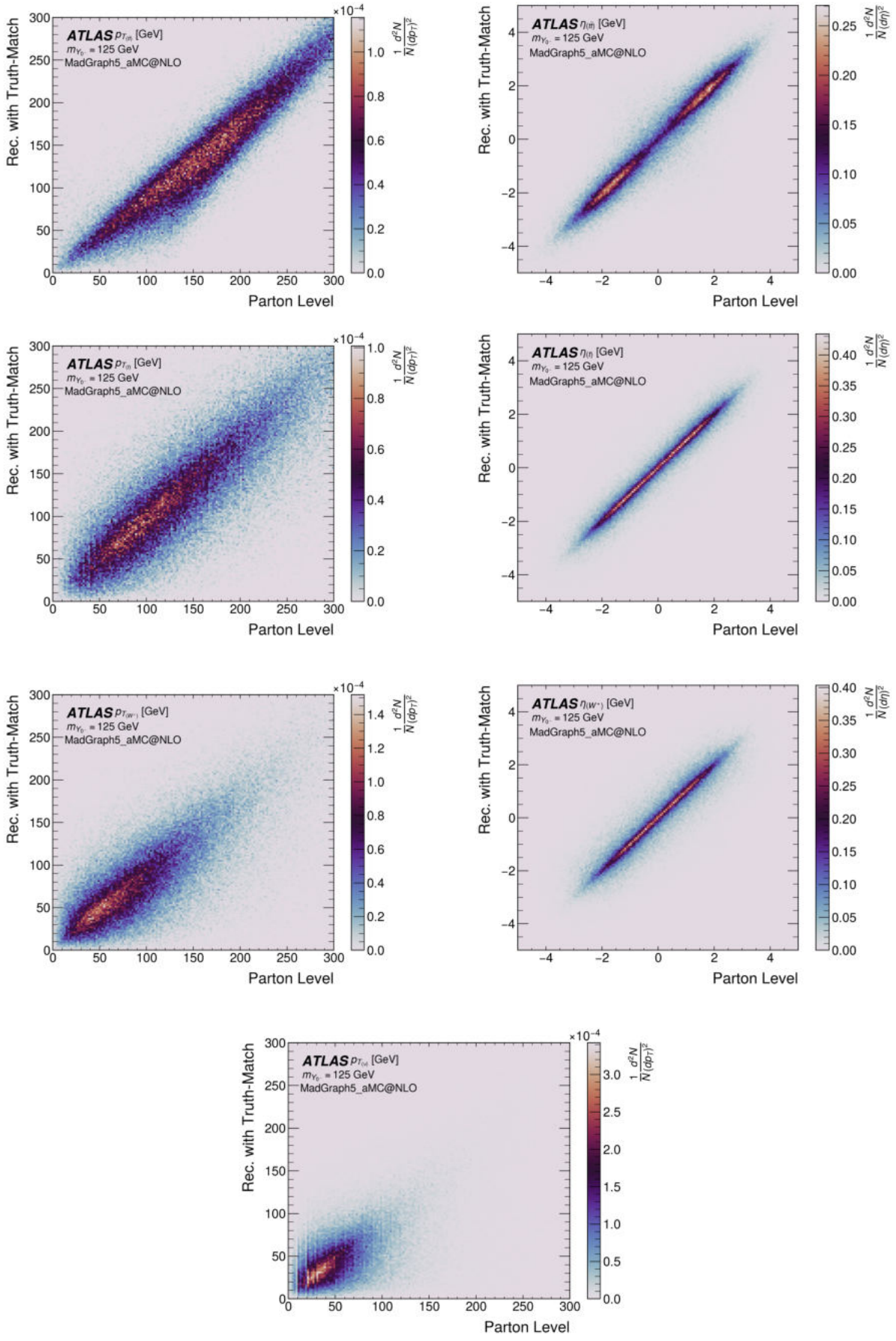

Figure 39: Two-dimensional kinematic distributions for $t\bar{t}Y_0$ events with $m_{Y_0} = 125$ GeV ($J^{CP} = 0^-$).

A.2 Reconstruction without Truth-Match

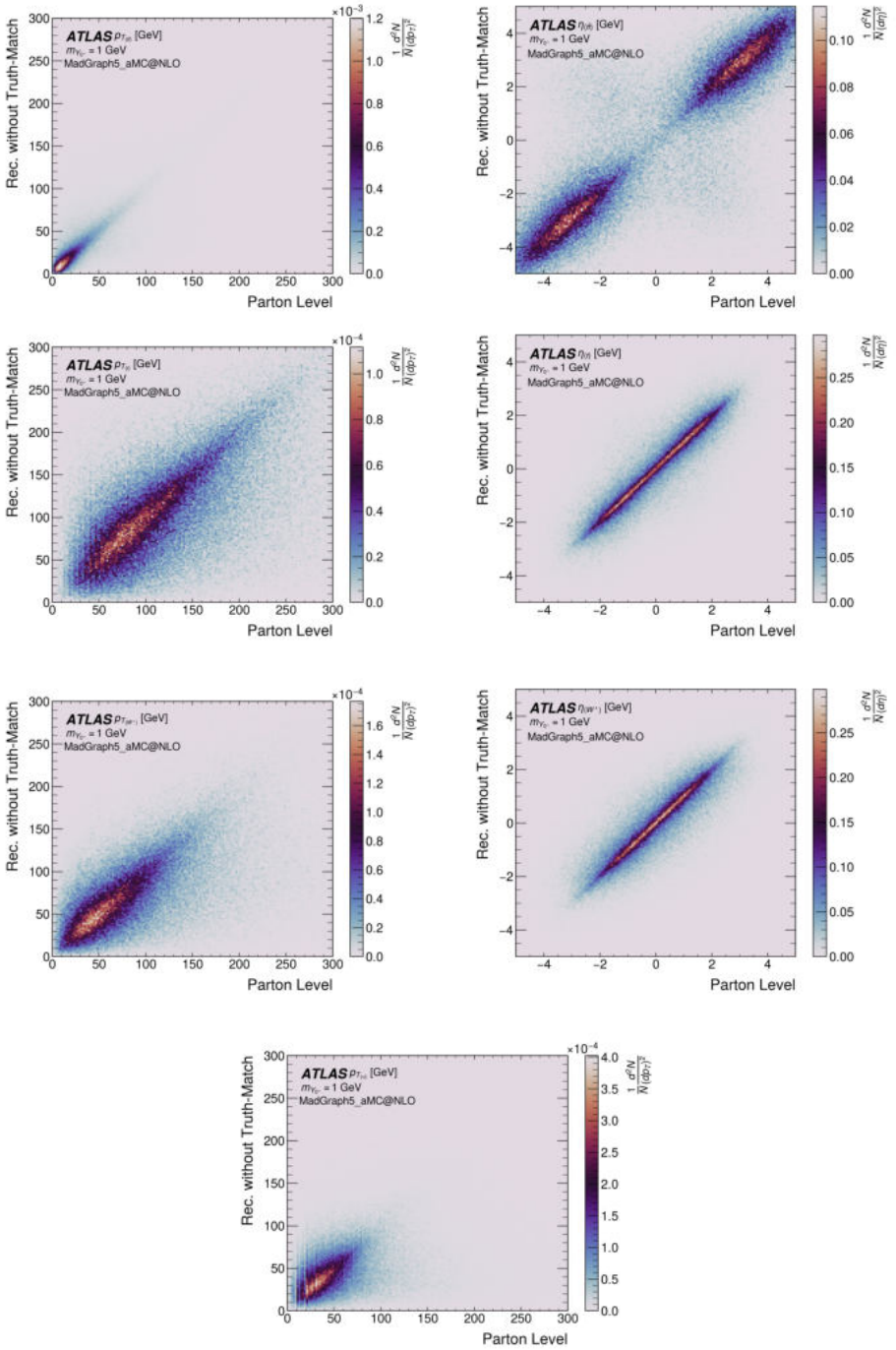

Figure 40: Two-dimensional kinematic distributions for $t\bar{t}Y_0$ events with $m_{Y_0} = 1$ GeV ($J^{CP} = 0^+$).

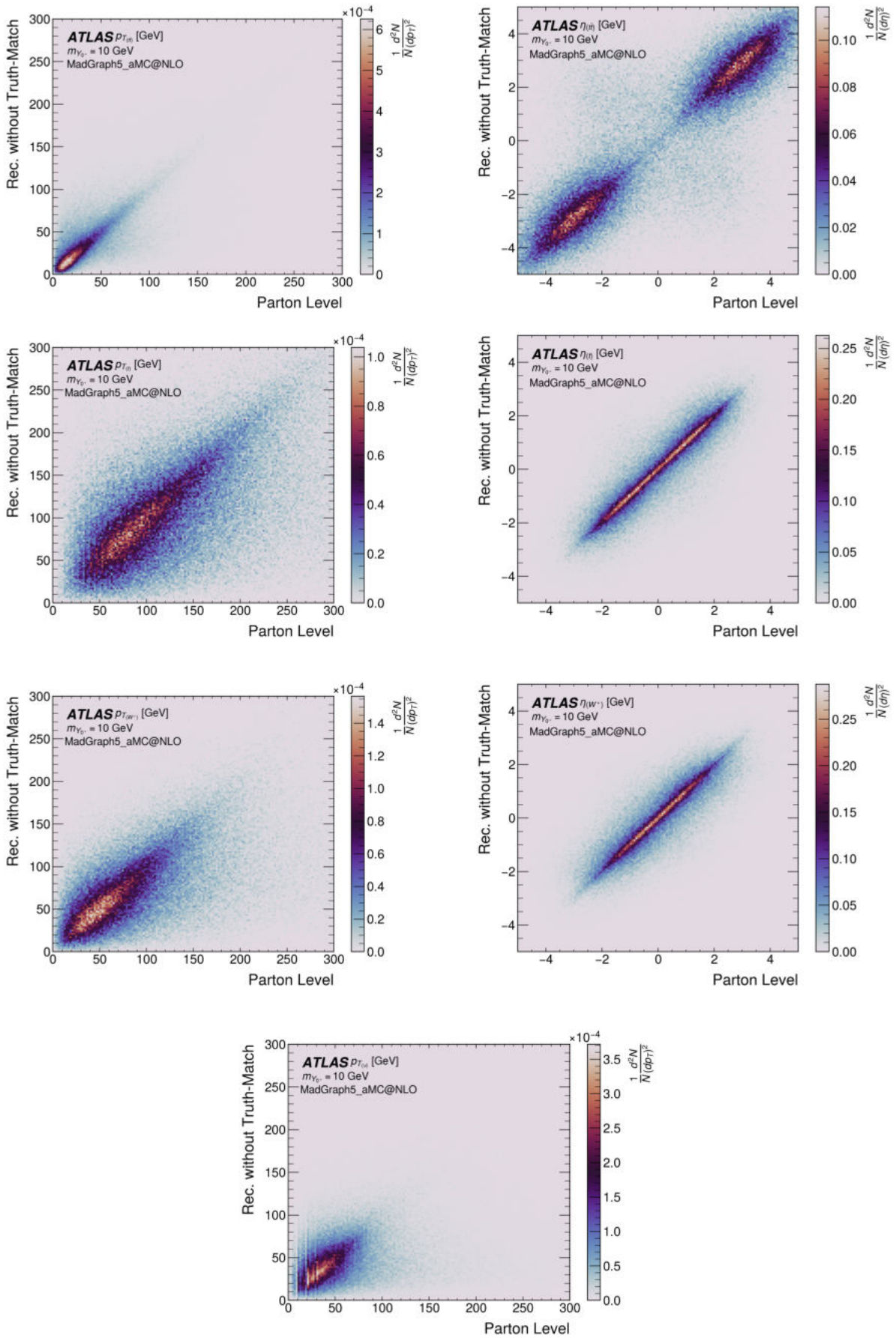

Figure 41: Two-dimensional kinematic distributions for $t\bar{t}Y_0$ events with $m_{Y_0} = 10$ GeV ($J^{CP} = 0^+$).

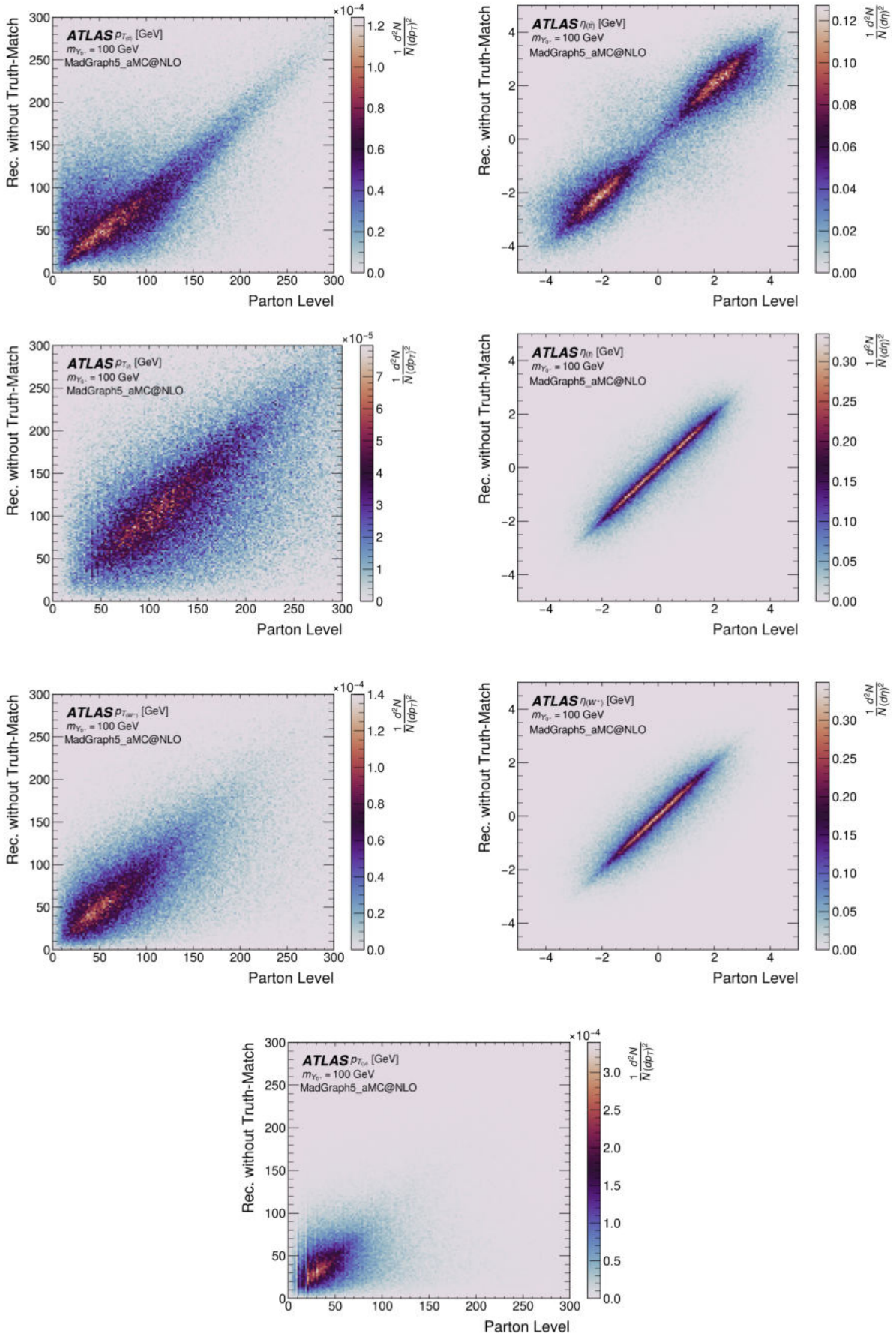

Figure 42: Two-dimensional kinematic distributions for $t\bar{t}Y_0$ events with $m_{Y_0} = 100$ GeV ($J^{CP} = 0^+$).

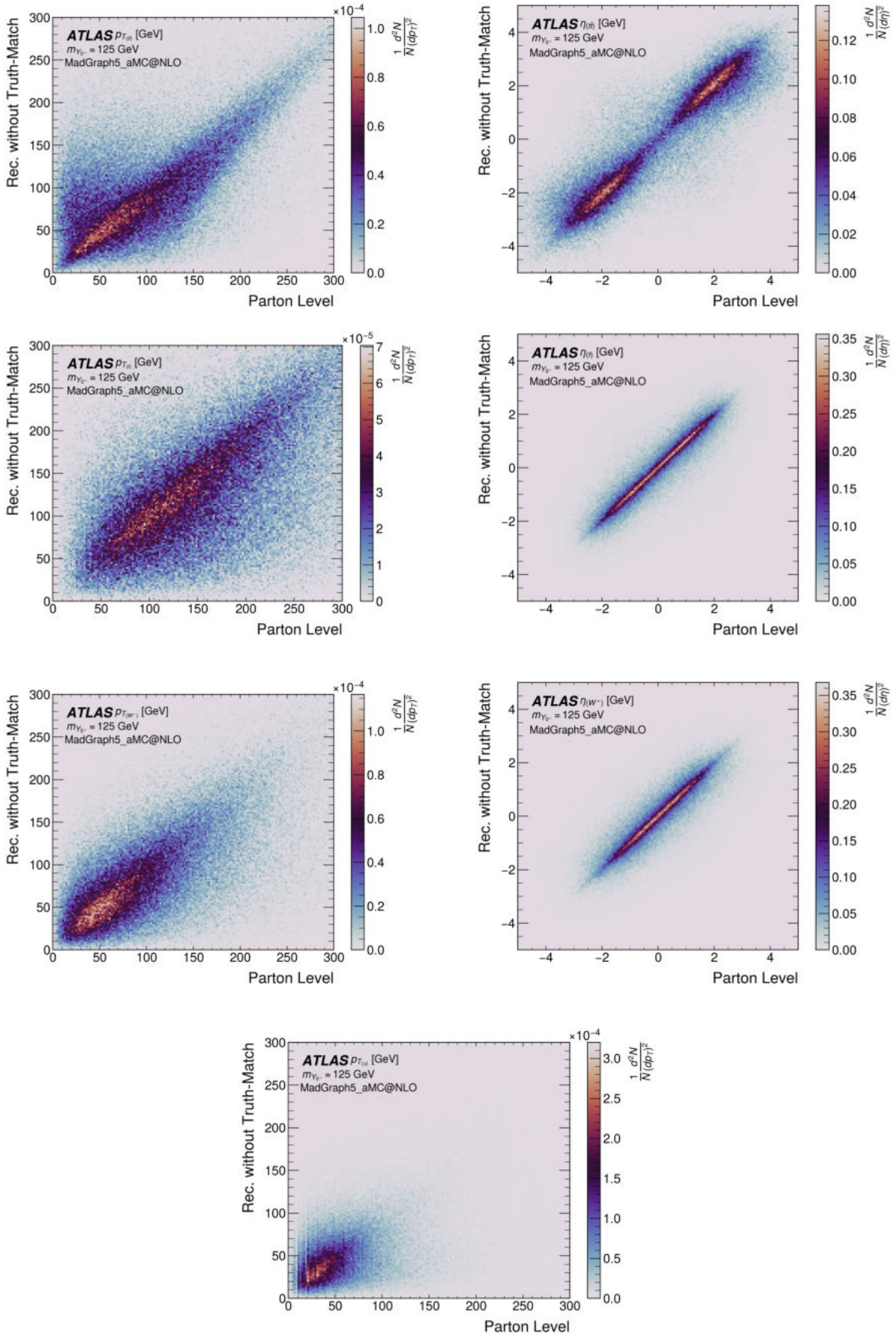

Figure 43: Two-dimensional kinematic distributions for $t\bar{t}Y_0$ events with $m_{Y_0} = 125$ GeV ($J^{CP} = 0^+$).

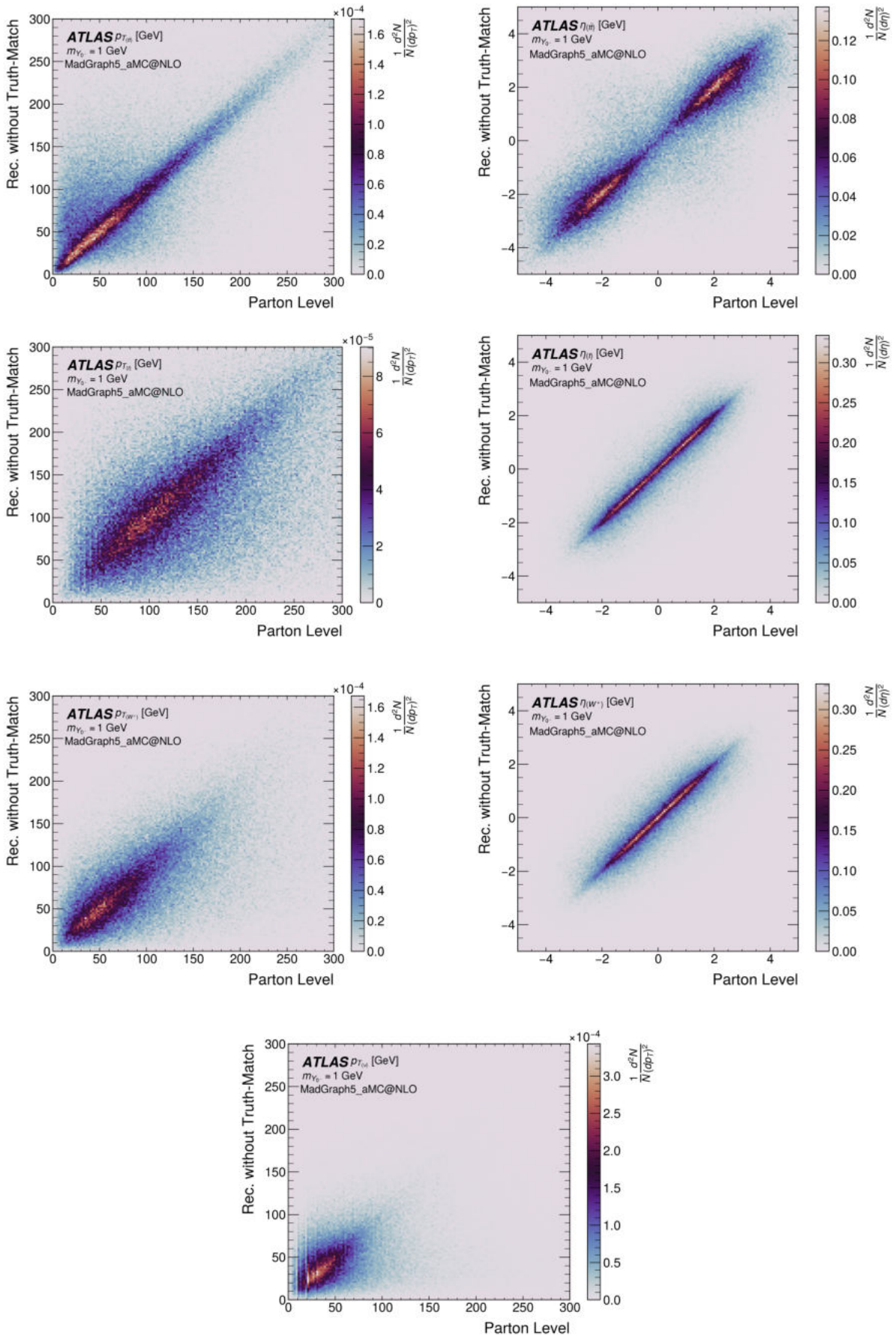

Figure 44: Two-dimensional kinematic distributions for $t\bar{t}Y_0$ events with $m_{Y_0} = 1$ GeV ($J^{CP} = 0^-$).

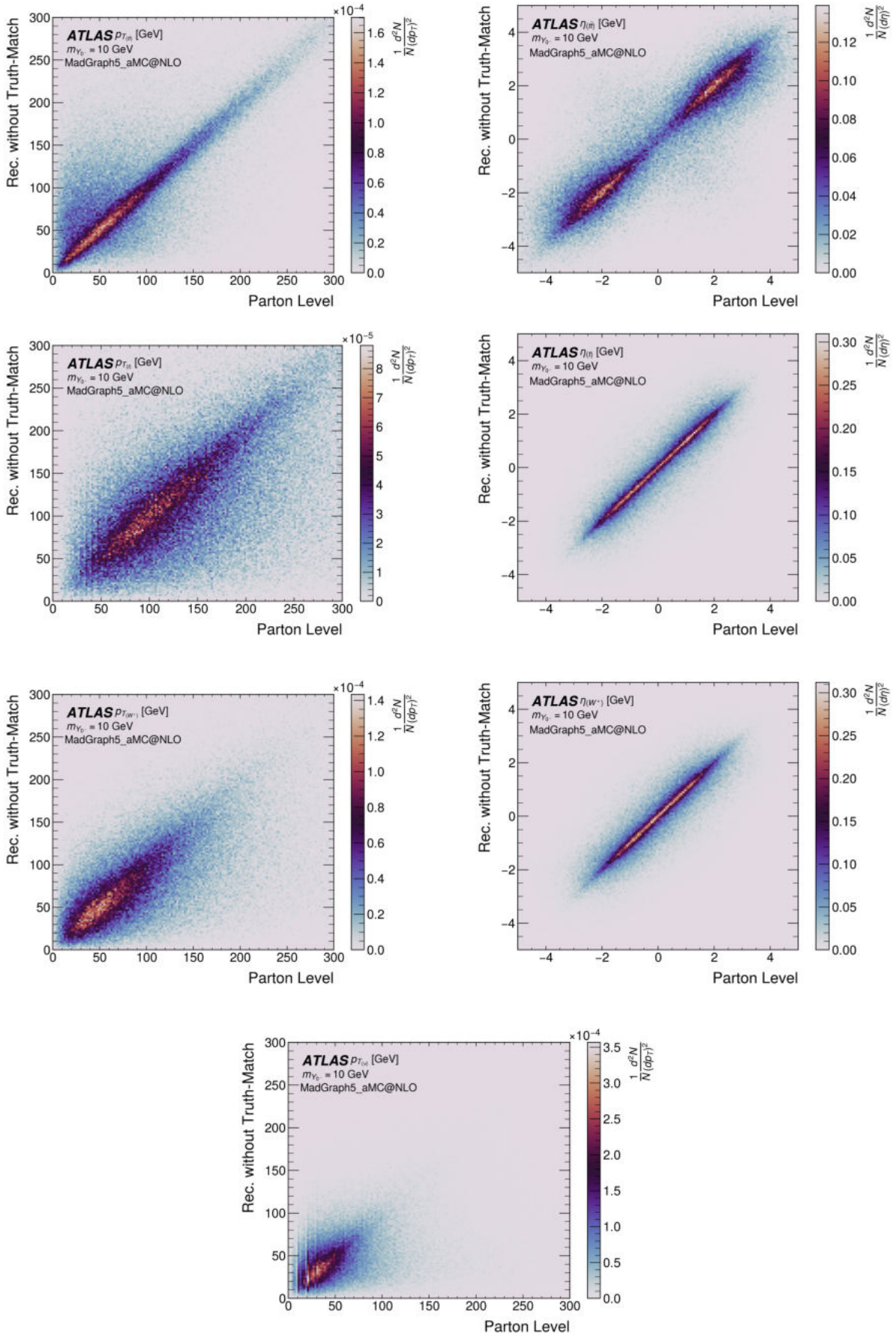

Figure 45: Two-dimensional kinematic distributions for $t\bar{t}Y_0$ events with $m_{Y_0} = 10$ GeV ($J^{CP} = 0^-$).

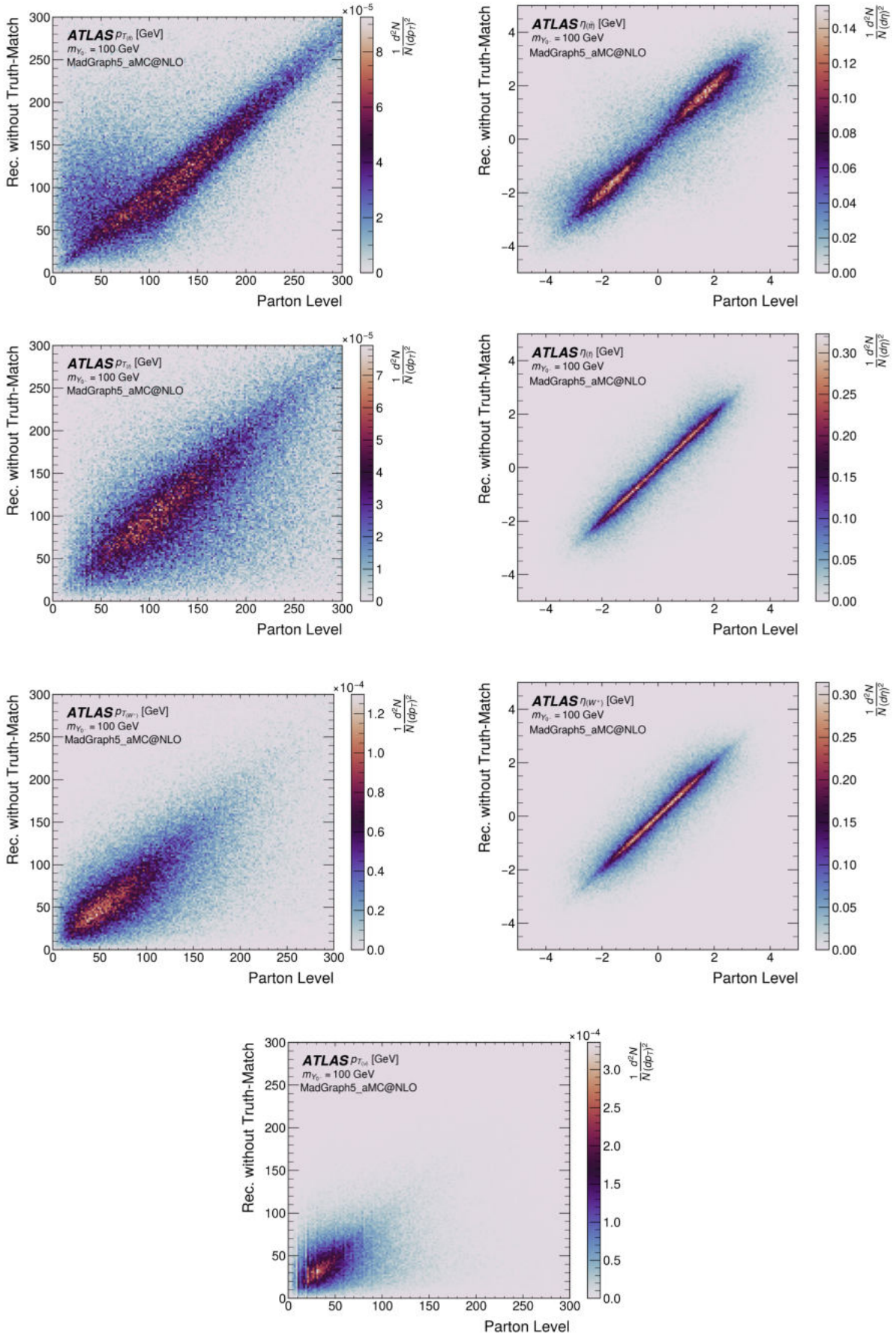

Figure 46: Two-dimensional kinematic distributions for $t\bar{t}Y_0$ events with $m_{Y_0} = 100$ GeV ($J^{CP} = 0^-$).

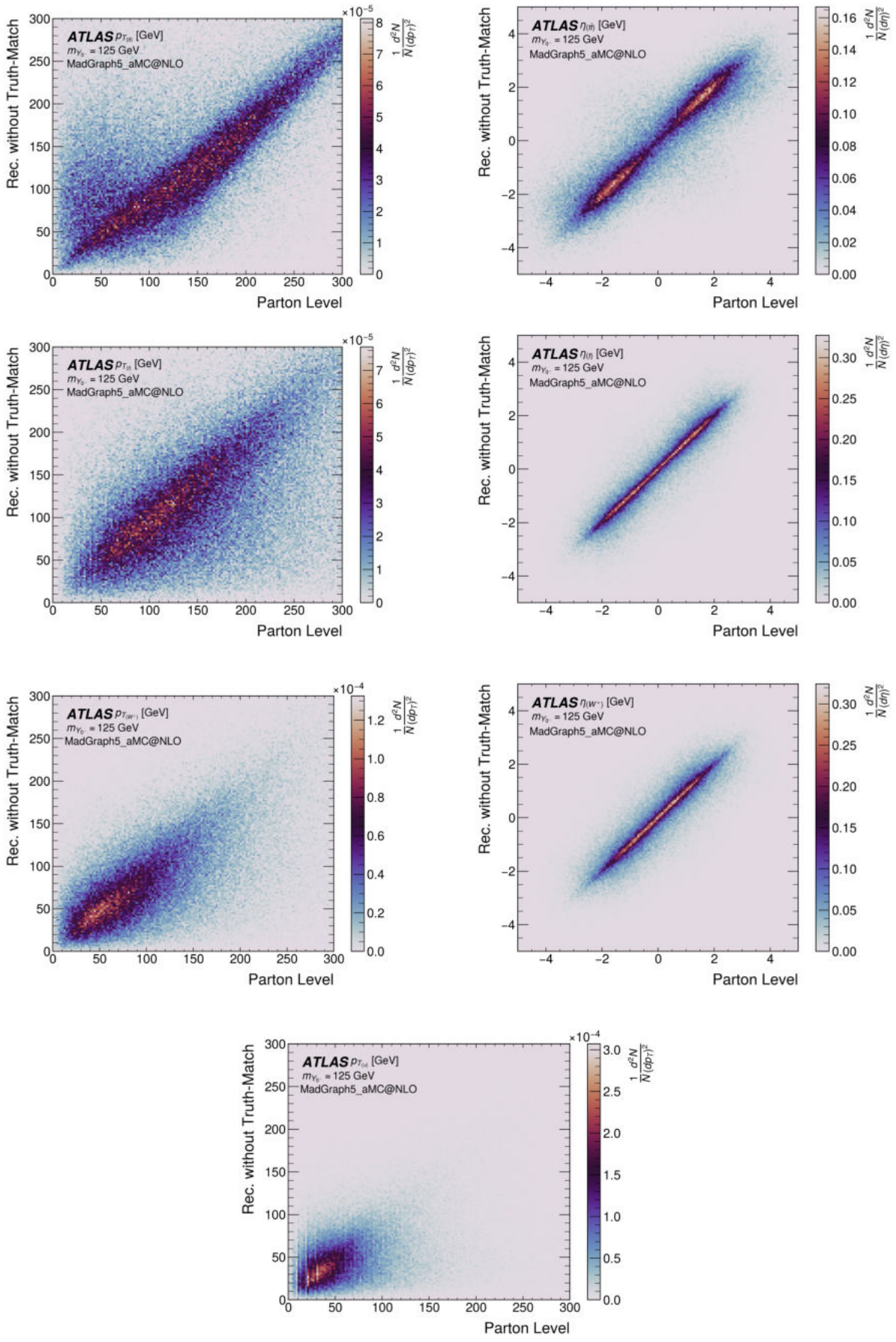

Figure 47: Two-dimensional kinematic distributions for $t\bar{t}Y_0$ events with $m_{Y_0} = 125$ GeV ($J^{CP} = 0^-$).

Appendix B
Exclusion Limits Plots

In this appendix, additional exclusion limit plots are presented for various mass scenarios. Appendix B.1 pertains to the *Scenario 1* exclusion hypothesis, while Appendix B.2 pertains to the *Scenario 2* exclusion hypothesis.

B.1 Scenario 1

The figures below correspond to the exclusion limit plots for various mediator masses:

- Figure 48 pertains to a mediator mass of 1 GeV;
- Figure 49 pertains to a mediator mass of 10 GeV;
- Figure 50 pertains to a mediator mass of 100 GeV;
- Figure 51 pertains to a mediator mass of 125 GeV.

B.2 Scenario 2

The figures below correspond to the exclusion limit plots for various mediator masses:

- Figure 52 pertains to a mediator mass of 1 GeV;
- Figure 53 pertains to a mediator mass of 10 GeV;
- Figure 54 pertains to a mediator mass of 100 GeV;
- Figure 55 pertains to a mediator mass of 125 GeV.

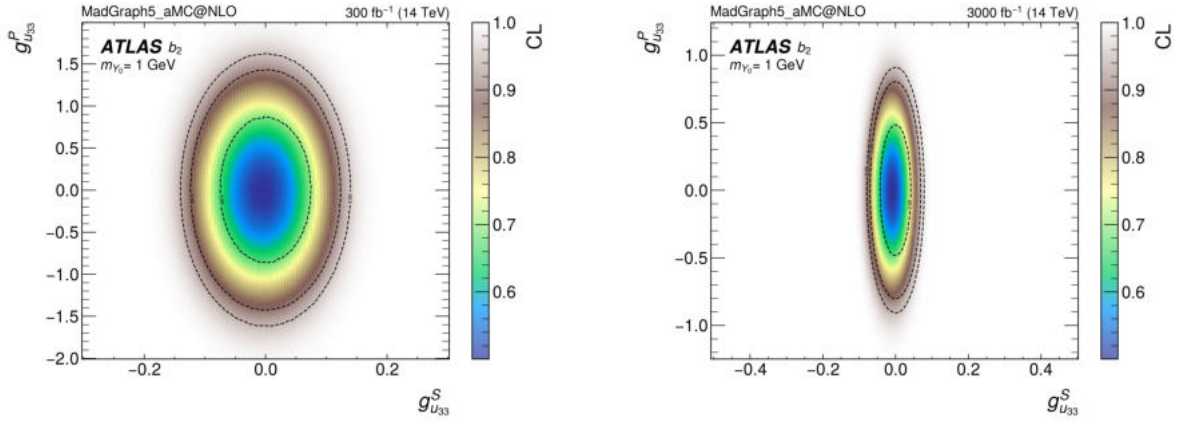

(a) b_2 ($m_{Y_0} = 1$ GeV)

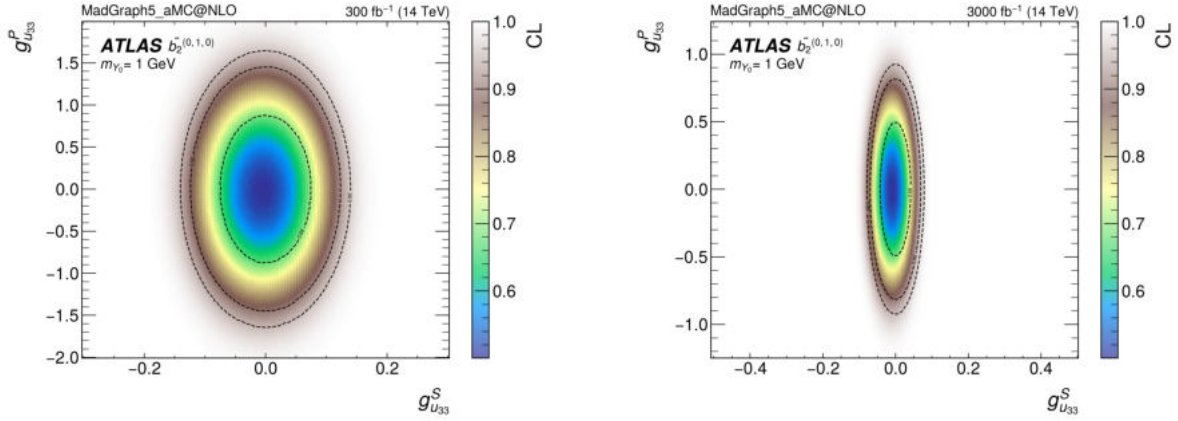

(b) $\tilde{b}_2^{(0,1,0)}$ ($m_{Y_0} = 1$ GeV)

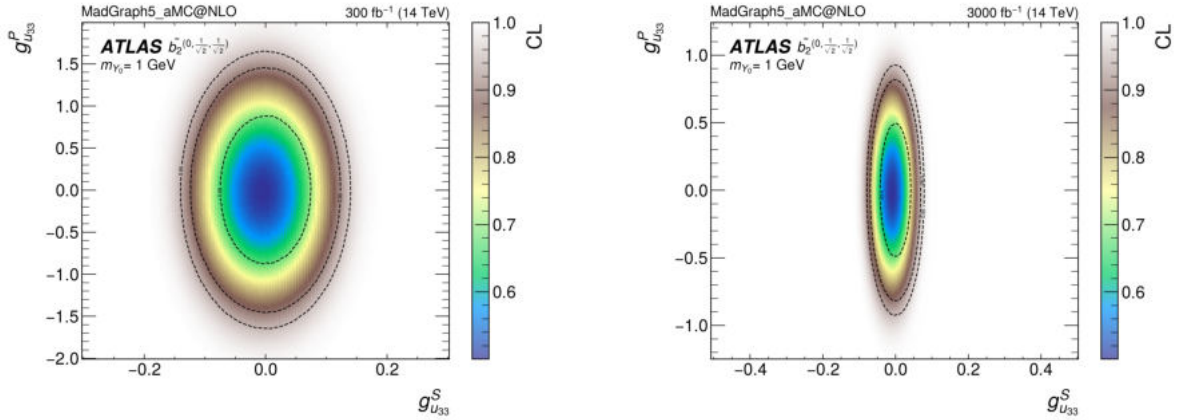

(c) $\tilde{b}_2^{(0,1/\sqrt{2},1/\sqrt{2})}$ ($m_{Y_0} = 1$ GeV)

Figure 48: CL limits for excluding the SM with a DM mediator, Y_0, characterized by mixed scalar and pseudo-scalar couplings with the top quarks, considering the SM as the null hypothesis.

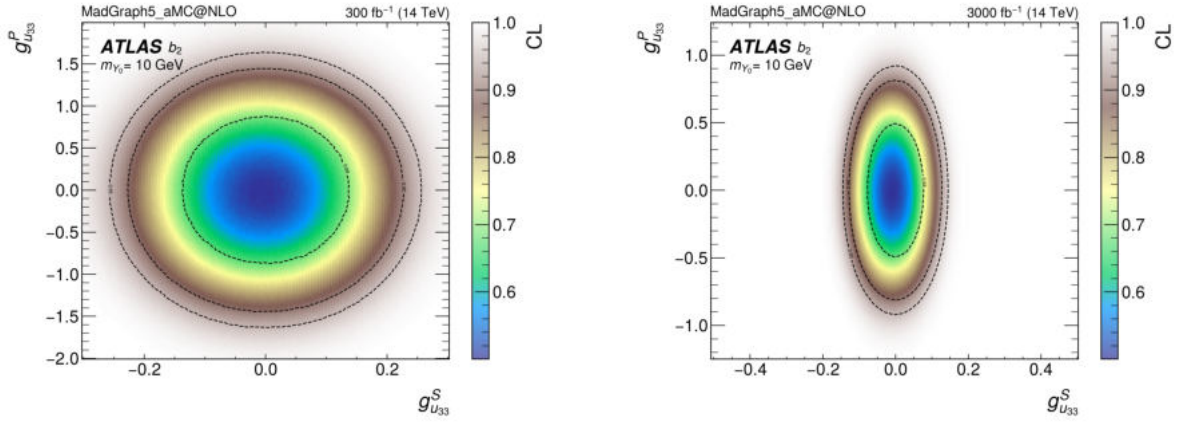

(a) b_2 ($m_{Y_0} = 10$ GeV)

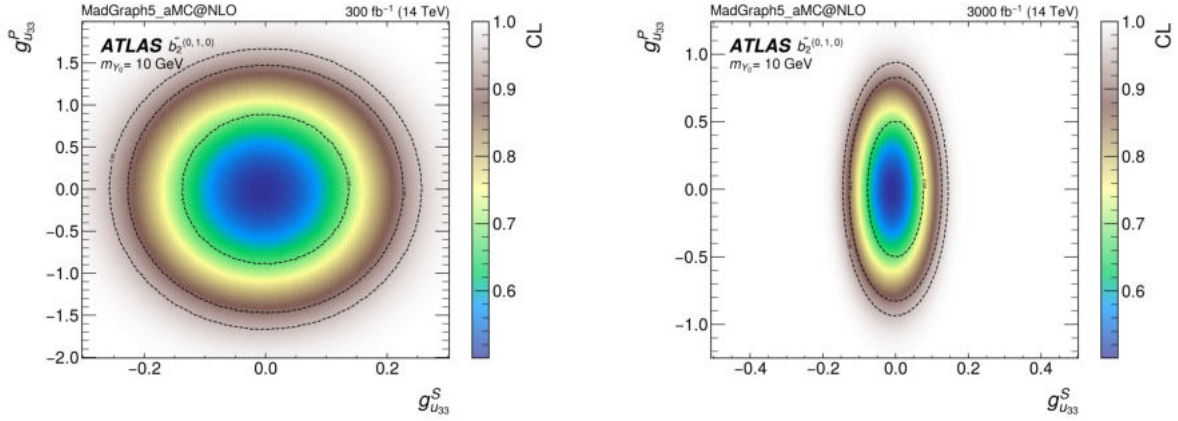

(b) $\tilde{b}_2^{(0,1,0)}$ ($m_{Y_0} = 10$ GeV)

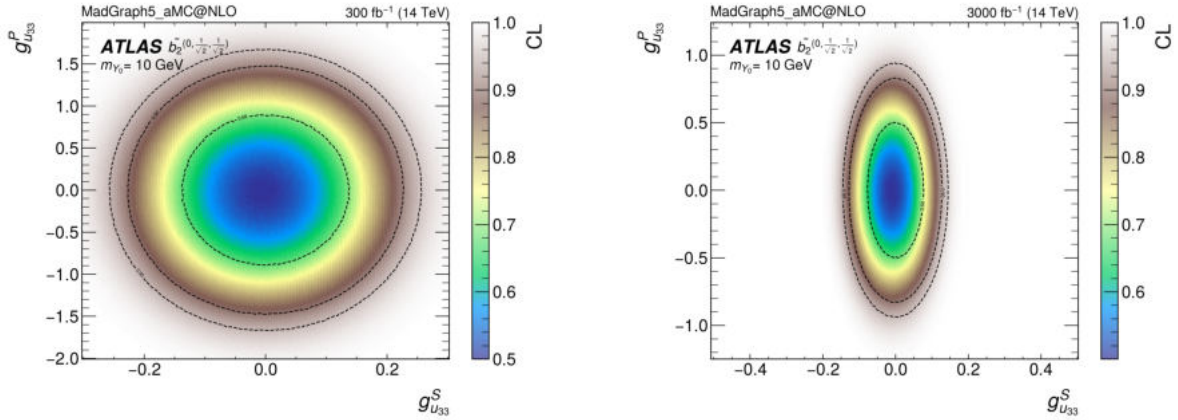

(c) $\tilde{b}_2^{(0,1/\sqrt{2},1/\sqrt{2})}$ ($m_{Y_0} = 10$ GeV)

Figure 49: CL limits for excluding the SM with a DM mediator, Y_0, characterized by mixed scalar and pseudo-scalar couplings with the top quarks, considering the SM as the null hypothesis.

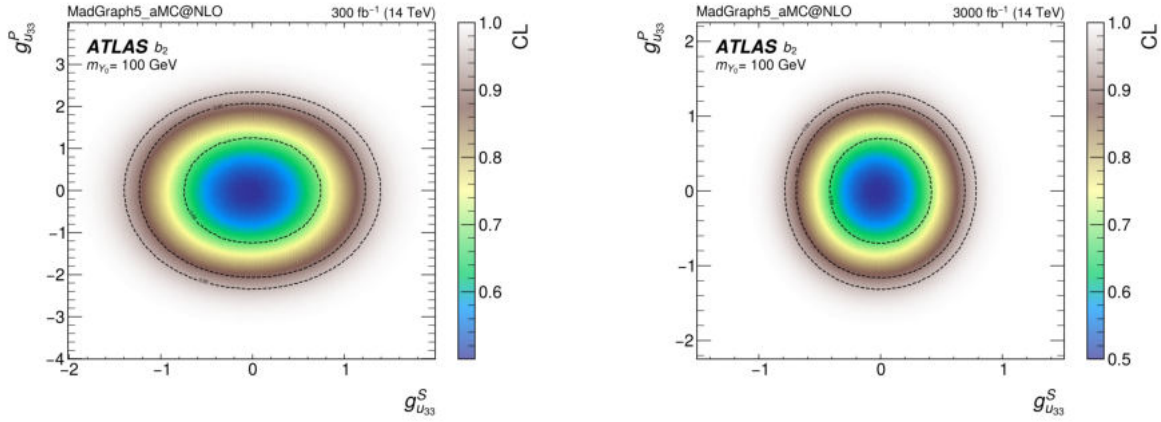

(a) b_2 ($m_{Y_0} = 100$ GeV)

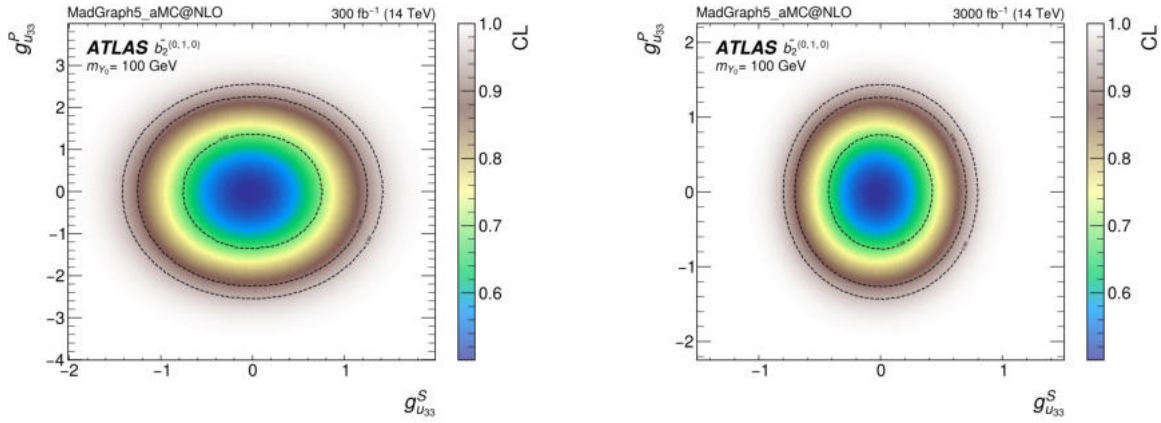

(b) $\tilde{b}_2^{(0,1,0)}$ ($m_{Y_0} = 100$ GeV)

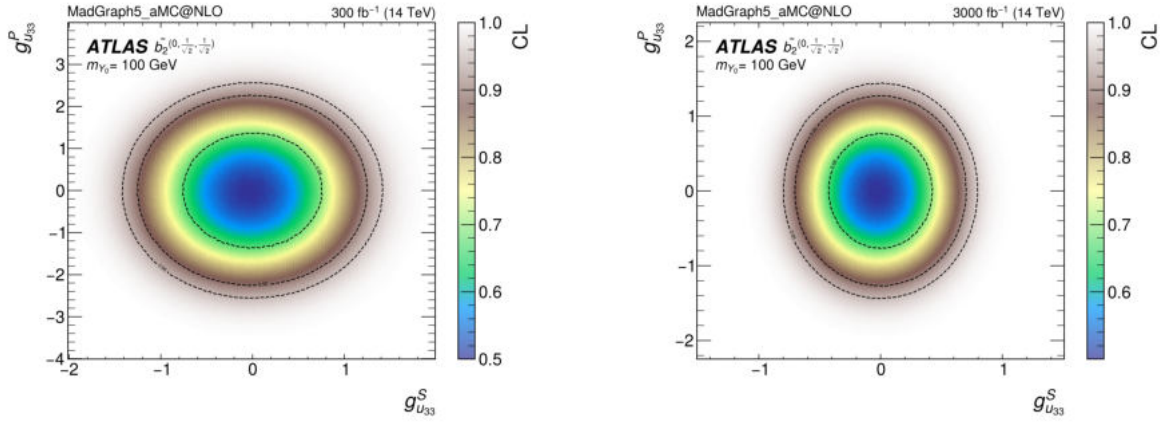

(c) $\tilde{b}_2^{(0,1/\sqrt{2},1/\sqrt{2})}$ ($m_{Y_0} = 100$ GeV)

Figure 50: CL limits for excluding the SM with a DM mediator, Y_0, characterized by mixed scalar and pseudo-scalar couplings with the top quarks, considering the SM as the null hypothesis.

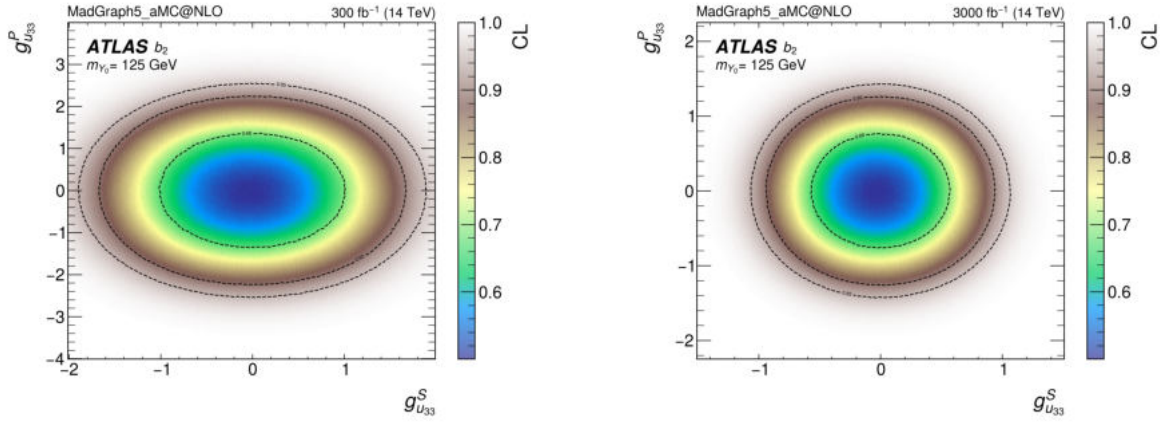

(a) b_2 ($m_{Y_0} = 125$ GeV)

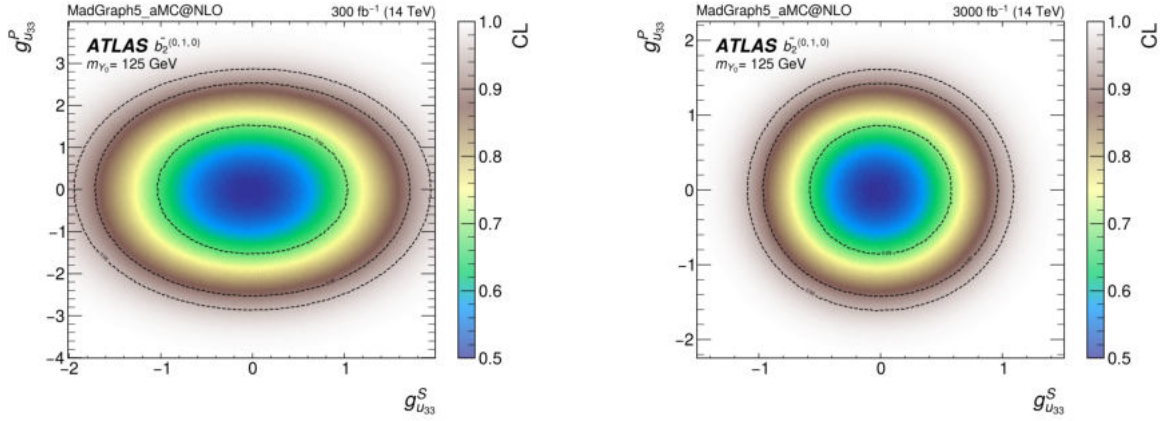

(b) $\tilde{b}_2^{(0,1,0)}$ ($m_{Y_0} = 125$ GeV)

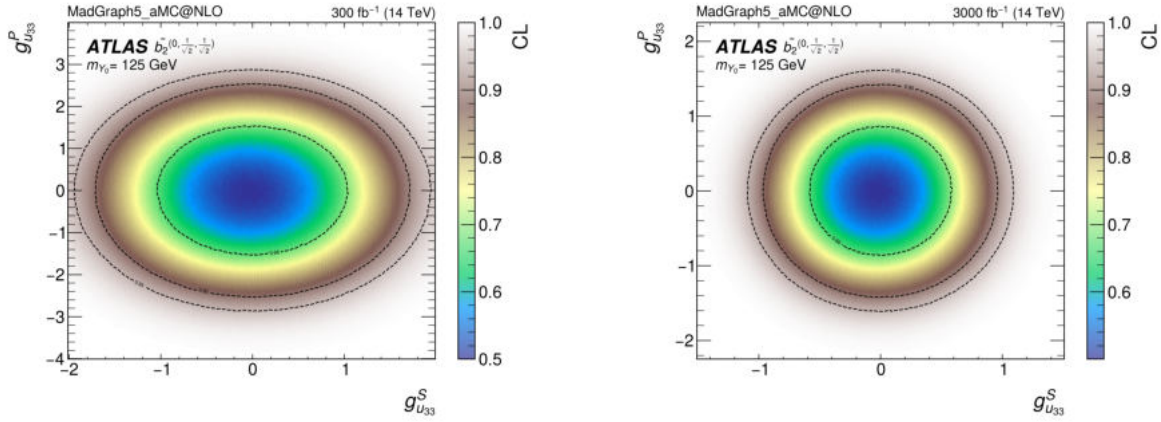

(c) $\tilde{b}_2^{(0,1/\sqrt{2},1/\sqrt{2})}$ ($m_{Y_0} = 125$ GeV)

Figure 51: CL limits for excluding the SM with a DM mediator, Y_0, characterized by mixed scalar and pseudo-scalar couplings with the top quarks, considering the SM as the null hypothesis.

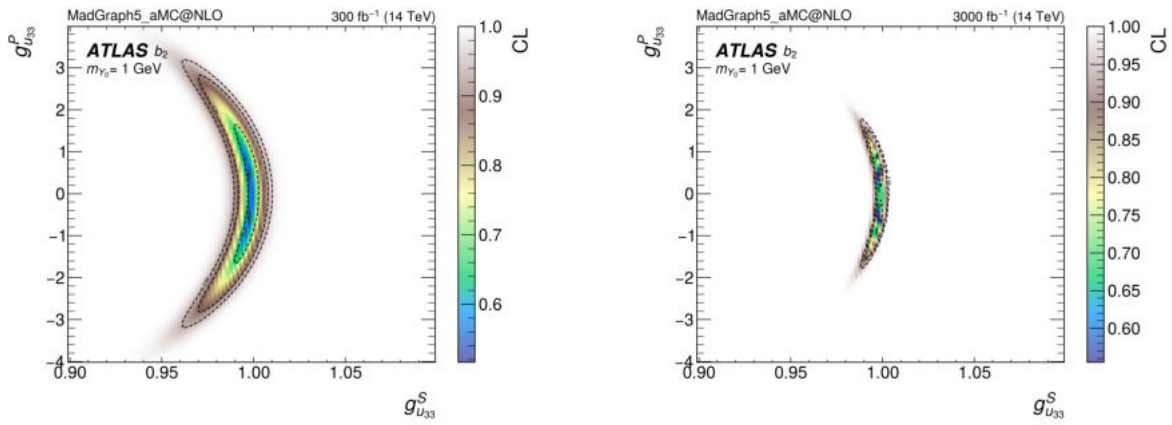

(a) b_2 ($m_{Y_0} = 1$ GeV)

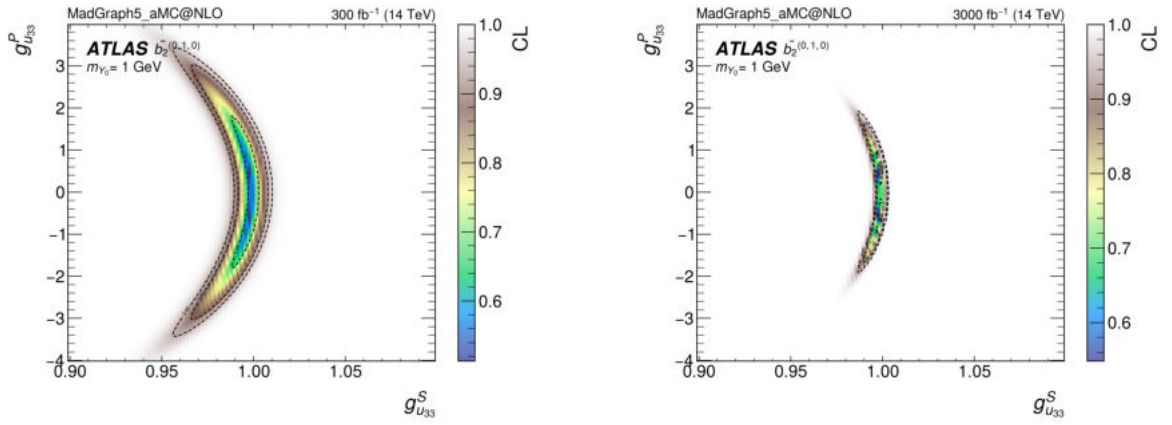

(b) $\tilde{b}_2^{(0,1,0)}$ ($m_{Y_0} = 1$ GeV)

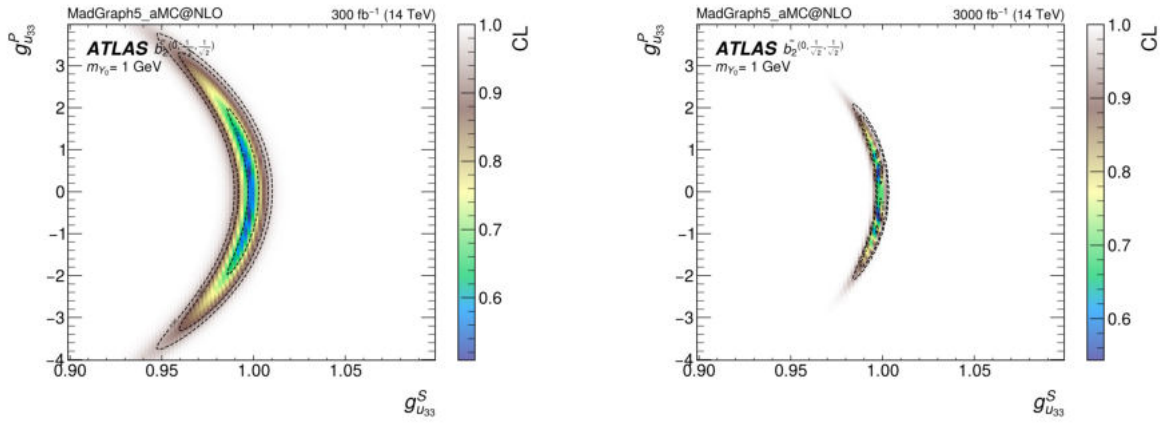

(c) $\tilde{b}_2^{(0,1/\sqrt{2},1/\sqrt{2})}$ ($m_{Y_0} = 1$ GeV)

Figure 52: CL limits for excluding the SM with a DM mediator, Y_0, characterized by mixed scalar and pseudo-scalar couplings with the top quarks, considering the SM plus a pure scalar DM mediator as the null hypothesis.

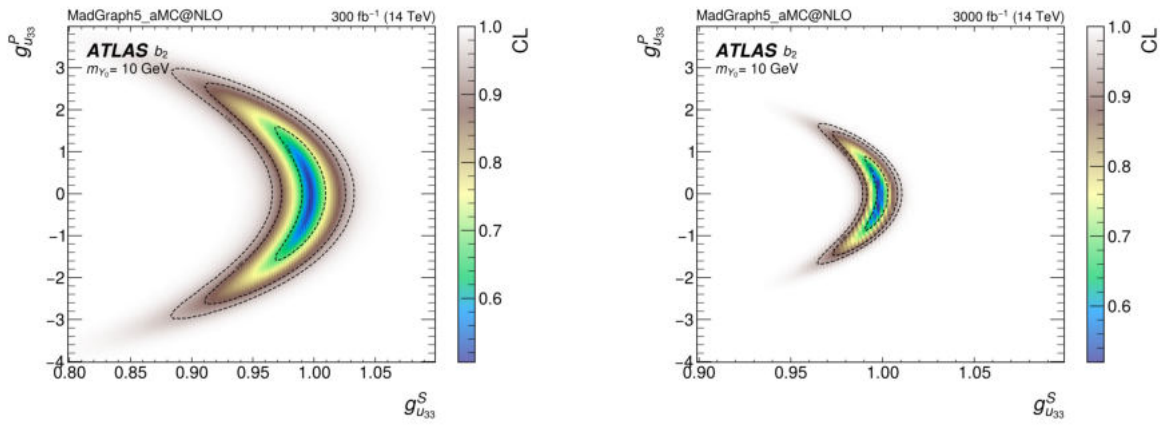

(a) b_2 ($m_{Y_0} = 10$ GeV)

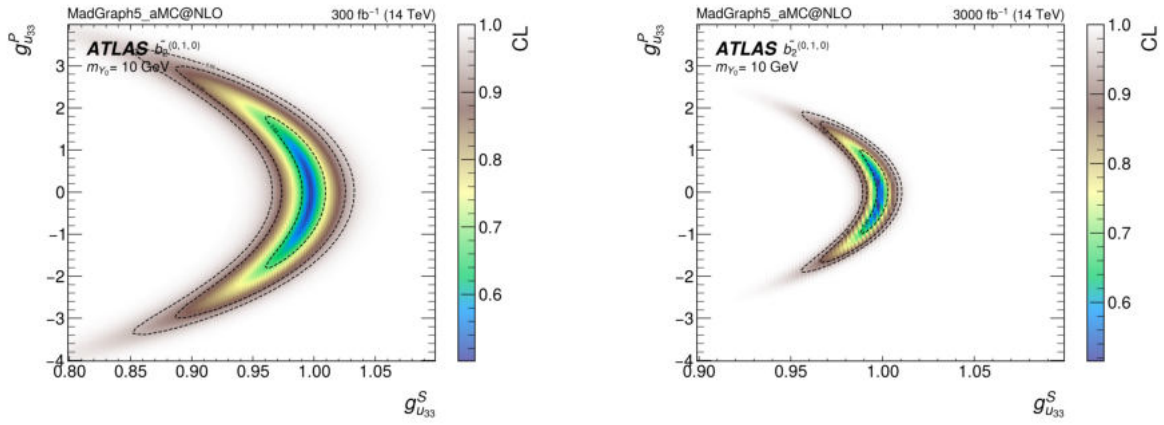

(b) $\tilde{b}_2^{(0,1,0)}$ ($m_{Y_0} = 10$ GeV)

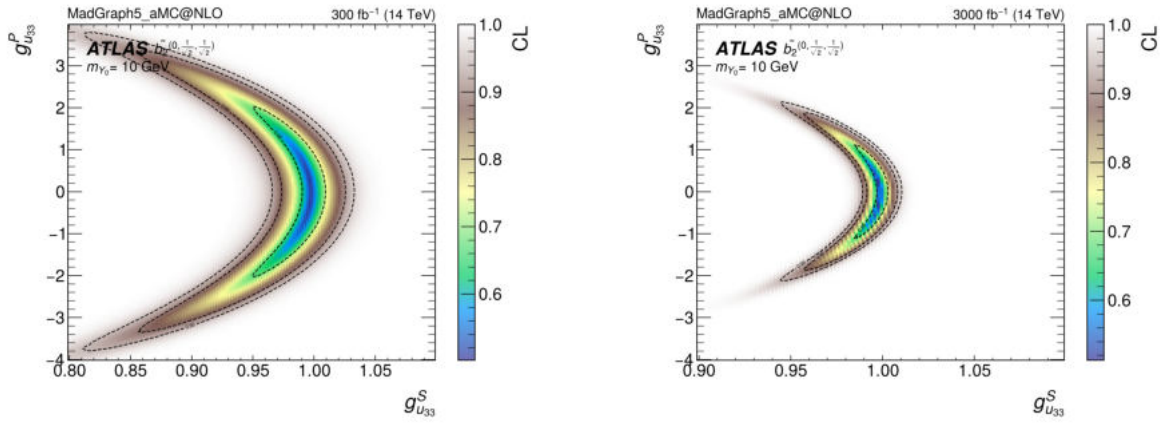

(c) $\tilde{b}_2^{(0,1/\sqrt{2},1/\sqrt{2})}$ ($m_{Y_0} = 10$ GeV)

Figure 53: CL limits for excluding the SM with a DM mediator, Y_0, characterized by mixed scalar and pseudo-scalar couplings with the top quarks, considering the SM plus a pure scalar DM mediator as the null hypothesis.

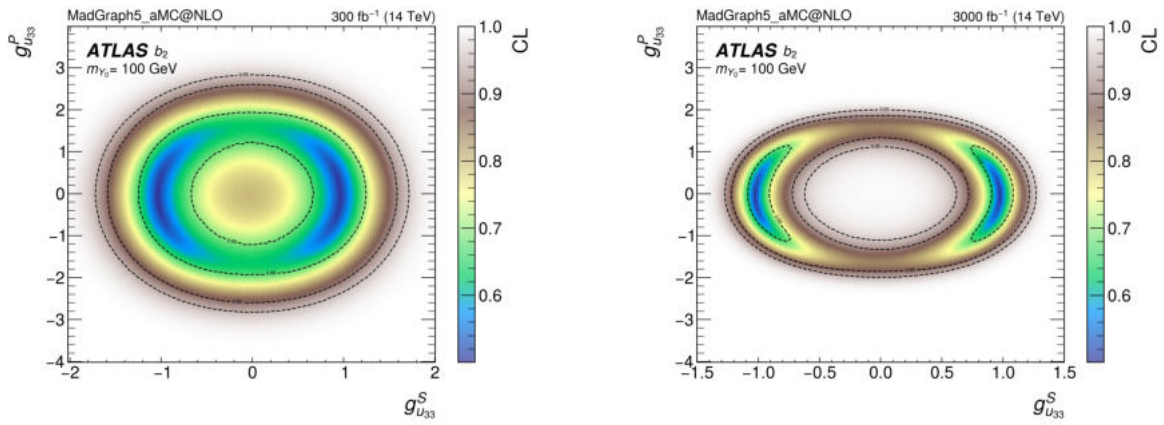

(a) b_2 ($m_{Y_0} = 100$ GeV)

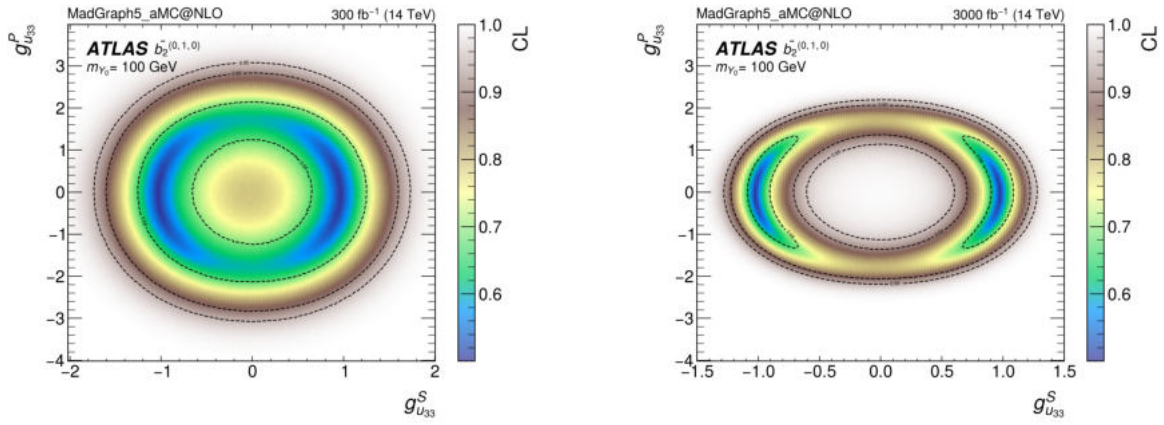

(b) $\tilde{b}_2^{(0,1,0)}$ ($m_{Y_0} = 100$ GeV)

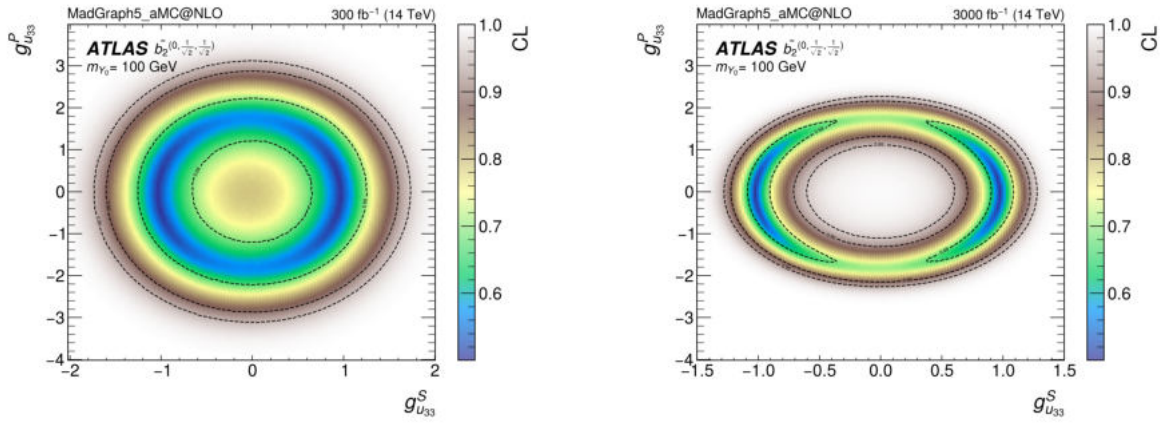

(c) $\tilde{b}_2^{(0,1/\sqrt{2},1/\sqrt{2})}$ ($m_{Y_0} = 100$ GeV)

Figure 54: CL limits for excluding the SM with a DM mediator, Y_0, characterized by mixed scalar and pseudo-scalar couplings with the top quarks, considering the SM plus a pure scalar DM mediator as the null hypothesis.

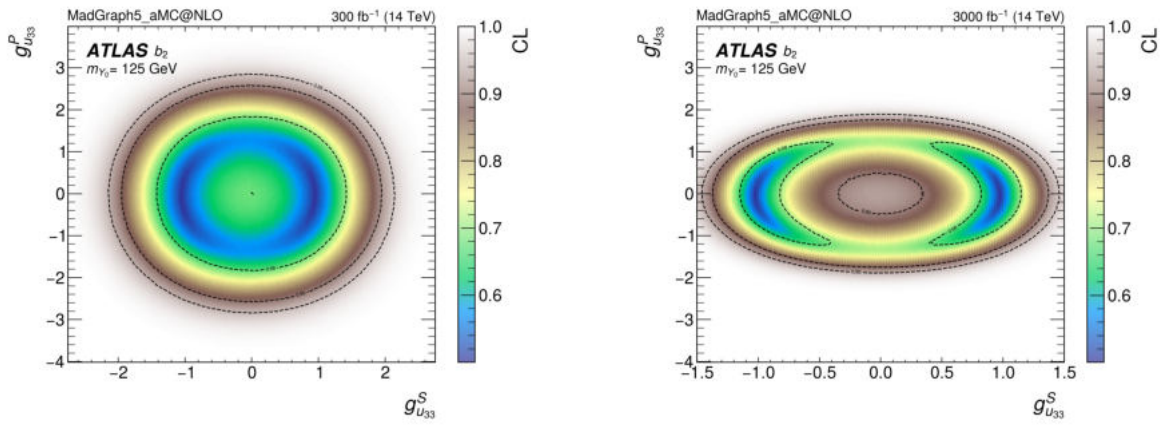

(a) b_2 ($m_{Y_0} = 125$ GeV)

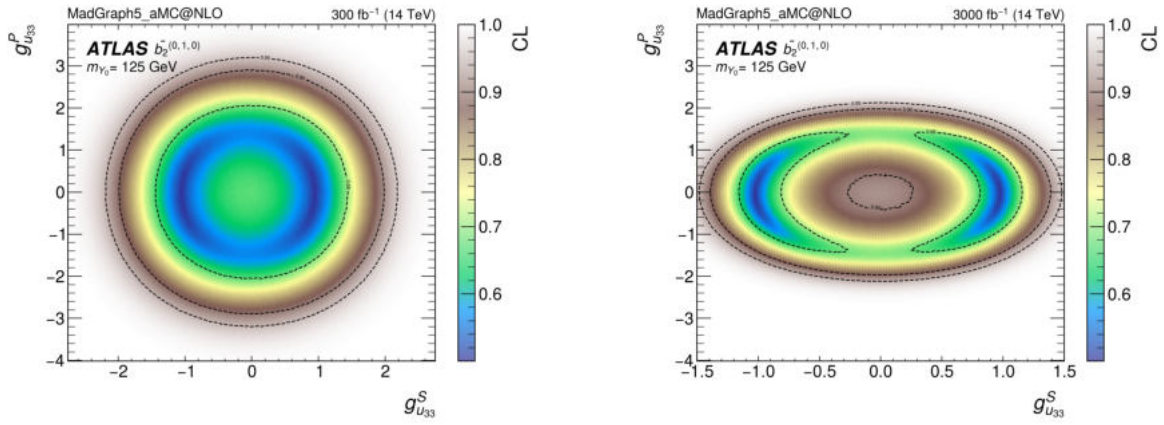

(b) $\tilde{b}_2^{(0,1,0)}$ ($m_{Y_0} = 125$ GeV)

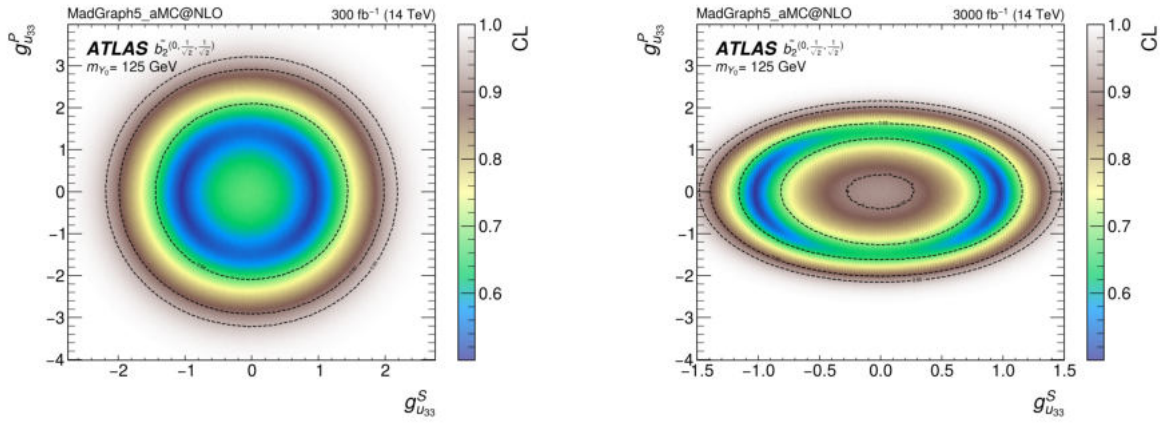

(c) $\tilde{b}_2^{(0,1/\sqrt{2},1/\sqrt{2})}$ ($m_{Y_0} = 125$ GeV)

Figure 55: CL limits for excluding the SM with a DM mediator, Y_0, characterized by mixed scalar and pseudo-scalar couplings with the top quarks, considering the SM plus a pure scalar DM mediator as the null hypothesis.